A MATHEMATICAL MODEL OF THE MAXIMUM POWER DENSITY ATTAINABLE IN AN ALKALINE HYDROGEN/OXYGEN FUEL CELL

Final Report

June 1991

Submitted to

Mr. Norman Hagedorn
Mail Stop 301–3
National Aeronautics and Space Administration
Lewis Research Center
21000 Brookpark Road
Cleveland, Ohio 44135

by

Michael C. Kimble and Ralph E. White
Department of Chemical Engineering
Texas A&M University
College Station, TX 77843–3122

ABSTRACT

A mathematical model of a hydrogen/oxygen alkaline fuel cell is presented that can be used to predict the polarization behavior under various power loads. The major limitations to achieving high power densities are indicated and methods to increase the maximum attainable power density are suggested. These performance indications can help future research and the design of alkaline fuel cells.

The alkaline fuel cell model describes the phenomena occurring in the solid, liquid, and gaseous phases of the anode, separator, and cathode regions based on porous electrode theory applied to three phases. Fundamental equations of chemical engineering that describe conservation of mass and charge, species transport, and kinetic phenomena are used to develop the model by treating all phases as a homogeneous continuum. Gas phase diffusional resistances are considered by calculating the spatial variation of the partial pressures of oxygen, hydrogen, and water vapor in the gas phase. The liquid phase diffusional resistances are accounted for by considering the concentration distributions of dissolved oxygen and hydrogen in KOH. The variation of the KOH electrolyte concentration is also accounted for by including the ionic resistance effects. Electronic resistances are considered by calculating the solid electrode potential drops in the porous gas diffusion electrodes. By developing a complete model of the alkaline fuel cell, the interaction of these various resistances can be investigated under conditions that simulate actual fuel cells.

A sensitivity analysis of the various transport and electrokinetic parameters indicates which parameters have the most influence on the predicted current density and over which range of potentials these parameters affect the fuel cell performance the most. This information can be used to decide which parameters should be optimized or determined more accurately through further modeling or experimental studies. The effect of various design parameters on the limiting current density are also investigated to determine if optimal values exist for the parameters. These parameter sensitivi-

ties and optimal design parameters can help in the development of better three-phase electrodes and separators for the alkaline fuel cell.

TABLE OF CONTENTS

LIST OF TABLES

LIST OF FIGURES

Figure Page

CHAPTER I

INTRODUCTION

The alkaline fuel cell (AFC) is capable of providing a clean, efficient, and high powered source of electrical energy. The relative ease of operation, low weight and volume, and reliable performance has made the alkaline fuel cell an attractive power source especially for the American space program as well as for electric vehicles, defense, stationary power sources, portable generators, and small submersibles to name a few (1–3). However, for applications that require even higher power densities, the performance of the alkaline fuel cell needs to be improved. A mathematical model of the alkaline fuel cell can assist in understanding better the phenomena occurring in the system as well as help in the design of fuel cells.

A. Fuel Cells

A fuel cell is a reactor where a fuel and an oxidizer react electrochemically producing products and releasing energy. Typically, during a combustion process, the energy of the fuel is released as heat which is then converted to electrical energy through a generator. However, one of the main advantages of the fuel cell is that the chemical energy of the fuel is directly converted into electrical energy which can be used to produce work. By avoiding the chemical to mechanical conversions, efficiencies of 50 to 60% can be achieved in fuel cells in contrast to the Carnot limited efficiencies of 15 to 25% in combustion engines (2).

Recent research in fuel cells has led to the development of various types of fuel cells such as the phosphoric acid, molten carbonate, solid oxide, and solid polymer electrolyte fuel cells as discussed by (1,4–7). However, these systems still cannot compete with the alkaline fuel cell's high power density. Continued research in

---

This document follows the style of the *Journal of the Electrochemical Society*

electrocatalysts, porous gas diffusion electrodes, and materials has increased the power density for the AFC dramatically since the 1960's (8). By developing a mathematical model of the alkaline fuel cell, the major factors that limit the performance of the system can be investigated. These performance indications can be used to guide future research in alkaline fuel cells.

B. Objectives

The maximum power density obtained from alkaline fuel cells has undergone many advances in recent years due to improved catalysts and electrode materials and also due to optimized operating conditions and fuel cell design. It has been known that in order to increase the power density in AFCs, the activation, concentration, and ohmic polarization should be minimized (4). For example, improved electrocatalysts for the oxygen reduction reaction in alkaline electrolytes has helped reduce the activation polarization (9); increased solid and solution conductivity has helped reduce the ohmic polarization (10); dual porosity electrodes have helped reduce concentration polarization (10–12). However, in order to investigate these phenomena, numerous and expensive experimental tests need to be performed. Furthermore, the interaction among the three types of polarization may cause difficulties in isolating the characteristics of a particular type of polarization. Mathematical modeling can help determine how changes in parameters and operating conditions will influence the various types of polarization which subsequently affect the performance of the fuel cell. The AFC model can help identify parameters and concepts that limit the performance of the fuel cell based on today's state-of-the-art technology. Additionally, the model can be used to investigate the effects of hypothetical advances in technology on the predicted performance.

The objectives of this work are to develop a realistic mathematical model of a hydrogen/oxygen alkaline fuel cell and to use the model to predict the maximum attainable power density. Fundamental equations of chemical and electrochemical

engineering are used to describe conservation of mass and charge, species transport, and kinetic phenomena in the fuel cell. Gas and liquid phase diffusional resistances as well as ionic and electronic resistances in the solution and solid phases, respectively, are accounted for in the model. The production and removal of water are also considered so that all electrochemically produced water will leave the system with the excess gas streams. The effects of the various transport, thermodynamic, and kinetic parameters on the fuel cell's performance are investigated to identify the more influential parameters. The mathematical model is then used to optimize the thicknesses and porosities of the fuel cell's various regions by maximizing the power density.

C. Structure of Report

This report contains the development and analysis of an alkaline fuel cell model. The motivation for developing this model is presented in Chapter I. A review of the relevant literature on porous gas diffusion electrodes and alkaline fuel cells is discussed in Chapter II. The development of the alkaline fuel cell model is shown in Chapter III along with some results of the dependent variables and model predictions. The sensitivity of the model predictions and the optimization of certain features of the fuel cell are presented in Chapter IV. The results of the alkaline fuel cell model are then summarized and recommendations for future studies are given in Chapter V.

CHAPTER II

LITERATURE SURVEY

A. Three Phase Electrodes

The need to increase current densities in electrochemical systems has led to the development of three phase electrodes (porous gas-diffusion electrodes) containing large interfacial surface areas between the solid electrocatalysts, electrolyte, and gaseous pores. However, since these electrodes contain a tortuous and non-uniform distribution of catalysts, gaseous-filled pores, and liquid-filled pores, it is difficult to accurately describe the phenomena occurring in the electrodes. Numerous experimental and modeling studies have been conducted over the years to describe and enhance the performance of these porous electrodes as discussed by (13–17). The major difficulty in modeling three-phase porous electrodes is in describing the electrode structure. Most gas-diffusion electrodes incorporate a hydrophobic agent such as Teflon or polytetrafluoroethylene (PTFE) mixed with the electrochemically active hydrophilic catalysts. This creates a stable three-phase boundary but also creates a very complex wetting phenomena making it difficult to characterize the structure of the electrode.

One of the earliest models for a three phase electrode was developed by Will (18,19) who conceptualized the three phase electrode as consisting of a thin liquid film in the form of a meniscus covering the electrocatalyst. Will concluded that most of the current is generated in a small diffusion region near the thin film/meniscus boundary. A slight variation to this approach was shown by Rockett and Brown (20) who allowed the thin film to have a variable thickness. These models only included solution phase diffusional and ohmic resistances, neglecting any gaseous and electronic resistances. The interaction of the KOH and dissolved O_2 kinetic parameters were shown to be responsible for the limiting current density in Rockett's model, rather than just a single parameter as concluded in prior models. A more complete thin film/meniscus model

was developed by Bennion and Tobias (21) where they considered the diffusion and migration of the relevant species and the solubility of O_2 in the electrolyte. Their model results showed that the current density is controlled by the charge transfer overpotential and the ohmic resistance drop in the thin film. They also concluded that the transport of dissolved O_2 is not rate limiting in the thin film meniscus region but is limiting in the bulk electrolyte regions.

Iliev et al. (22) developed a simple model of a gas-diffusion electrode that considered the Knudsen diffusivity of gaseous O_2, gas dissolution, and ohmic drop only. They considered the diffusion of gaseous O_2 as occurring by Knudsen diffusion rather than molecular diffusion since the pore radii were on the order of 30 nm for their work. They concluded that the porous structure of the electrode and the mode of mass transfer through the gaseous pores are responsible for the electrochemical activity in the electrode. Unfortunately, their model did not include ionic or electronic resistances which can drastically influence the system.

The models by Will, Rockett, and Bennion are usually termed microscopic models since they try to describe the physical phenomena occurring at the three-phase boundaries. Another approach to describing three-phase electrodes is to treat them macroscopically where the unknown structural geometries of the porous electrodes are assumed to be homogeneously mixed. One such approach is the agglomerate model (23–25) where the catalyst particles and the gaseous and liquid filled pores co-exist in a homogeneous continuum. One of the earlier agglomerate models was developed by Giner(23) who accounted for the diffusion of a dissolved gaseous species in parallel with an electrochemical reaction in a cylindrical agglomerate. Giner also accounted for the solution phase potential variation. The model results showed the performance of the electrode as a function of agglomerate radius and catalyst utilization.

Cutlip (26) developed an analytical model of the mass transfer process occurring in gas diffusion electrodes. This model was primarily designed to study the mass transfer

effects due to low concentrations taking into account gaseous diffusion, gas dissolution, and the transport of dissolved gas. Catalyst effectiveness factors (27) were used to modify the electrocatalyst based on different shape factors. Cutlip concluded that the limiting current density is not influenced by the liquid phase diffusional resistances. Another important conclusion from Cutlip's model was that the coupling of the gas-phase diffusional resistance and electrode thickness were strongly influential on the limiting current density. The limiting current density was found to be proportional to electrode thickness when the gas-phase diffusional resistance was non-existent. Conversely, the limiting current density was found to be independent of electrode thickness when gas phase diffusional resistances were present.

An improvement to Giner's flooded agglomerate model and to Cutlip's earlier model was presented by Iczkowski and Cutlip (28) who developed a fairly complete model of a three-phase electrode. This model accounted for the gaseous diffusion resistances, solution phase diffusional resistances, and solid and liquid potential variations. They fitted their model to experimental polarization curves by adjusting the radius of the agglomerates, electrolyte film thickness, and the porosity-tortuosity factor of the gaseous and liquid filled pores. They applied their model to a phosphoric acid electrode up to current densities of 370 mA/cm^2 and concluded that ohmic resistance was the major cause of polarization losses in the electrode followed by Knudsen and molecular diffusion effects. However, they concluded that the solution phase resistance of dissolved oxygen diffusion contributed the least to the polarization losses.

An agglomerate model for a double-layered oxygen electrode was also given by (29) where it was assumed that the electrochemical reaction was analogous to the diffusion and reaction of a gaseous reactant in a porous catalyst pellet surrounded by a gaseous film. Unfortunately, too many simplifying assumptions (*e.g.*, constant overvoltage, constant electrolyte concentration, simple Tafel kinetics, etc.) limit the applicability of this approach to more complex phenomena occurring in the electrode.

A different macroscopic model applied to two-phase porous electrodes was developed by Newman and Tobias (30) which is commonly referred to as porous electrode theory. This approach treats the different phases in the electrode as a homogeneous continuum that can be characterized by measurable quantities such as the porosity and specific surface area as described by (17). This macroscopic approach to describing the porous electrode assumes that the variables of interest are continuous in time and space allowing them to be averaged over a small volume element in the electrode. A macroscopic treatment of the chemical, electrochemical, and physical processes occurring in a three-phase electrode was developed by Darby (31) and extended by White *et al.* (32) based on porous electrode theory. It is, perhaps, rather unfortunate that the continuum approach has been criticized as being too abstract in comparison to the agglomerate approach (23). A close examination of the two macroscopic methods show that both methods are essentially describing the same type of conceptualization; the major differences being the way electrode surface areas and film thicknesses are handled.

B. Alkaline Fuel Cell Models

As shown in the previous section, there have been many investigations into three phase electrodes, in particular, the oxygen electrode since it is responsible for most of the polarization losses in AFCs. Unfortunately, no complete model of the alkaline fuel cell exists in the open literature that contains both electrodes and the separator. It is difficult to generate any firm conclusions on an entire fuel cell assembly when only a single electrode model is used since the interactions between the anode, cathode, and separator are not considered.

All of the single electrode models presented above simplified or neglected various forms of resistance (*i.e.*, gas phase diffusion, liquid phase diffusion, electronic, or ionic resistances). Some of these simplifications such as constant electrolyte concentration or constant solid potential are, as will be shown later, justified when a low overvoltage

is applied as was done in these models. However, at higher overvoltages, the assumptions of constant potentials and concentrations fail since large polarization effects are occurring. Hence, the previous models are not sufficient when trying to predict high power density performance. By considering all pertinent regions in the alkaline fuel cell, performance predictions can be made at high power densities.

CHAPTER III

A ONE-DIMENSIONAL MODEL OF AN ALKALINE FUEL CELL

A. Introduction

A schematic of an overall alkaline fuel cell system with its associated gas channels is shown in Fig. 1 which is used as a basis for the model development. The modeling region itself is presented in Fig. 2 showing a conceptualization of the three-phase electrodes. The AFC operates by flowing either dry or humidified hydrogen and oxygen gases through the anode and cathode gas flow channels, respectively. As these gases flow through the channels, humidified hydrogen gas diffuses into the gas diffusion region of the anode while humidified oxygen gas diffuses into the gas diffusion layer of the cathode. Next, the gases diffuse into the reaction layers of the electrodes, where the gases further diffuse in the gaseous phase as well as dissolve into the KOH electrolyte. In the middle of the fuel cell is a non-conducting microporous separator matrix which is assumed to prevent any gases from diffusing across the system. In some alkaline fuel cells, the electrolyte is circulated out of the system which helps maintain a constant electrolyte concentration and assists in heat and water removal. A design constraint for this work is that the KOH electrolyte does not circulate outside the system. This will cause large electrolyte concentration variations across the electrodes and separator. In practical fuel cells, the liquid water produced in the system dilutes the KOH electrolyte to a certain extent. It is assumed that all electrochemically produced liquid water evaporates into the gas streams. This assumption is reasonable since in actual alkaline fuel cells the average electrolyte concentration reaches a constant value at steady state.

The design of the porous gas-diffusion electrodes is critical in order to achieve high performance in the alkaline fuel cell. It is important that the three-phase boundaries in these electrodes provide a high utilization of the catalyst clusters which will give large

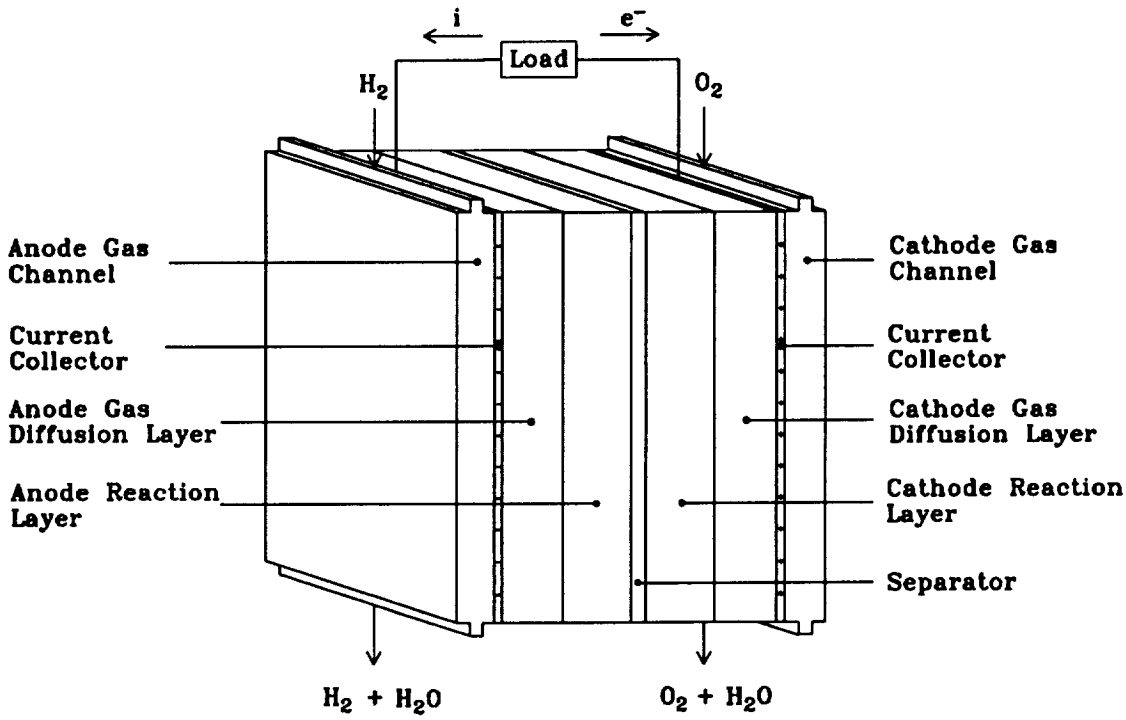

Figure 1. Overall schematic of a hydrogen/oxygen alkaline fuel cell.

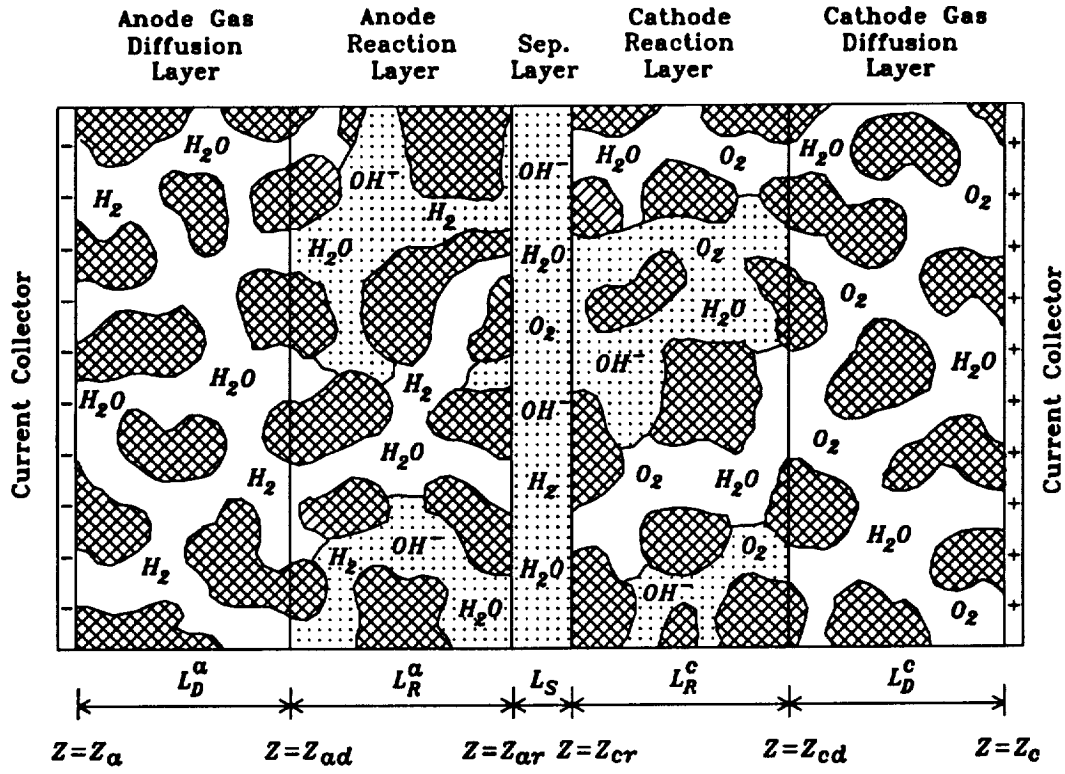

Figure 2. Detailed schematic of the three-phase regions in a hydrogen/oxygen alkaline fuel cell.

surface areas for the electrochemical reactions. It is also important that the electrodes have good electrical conductivity and are corrosion resistant. The preparation and design of some high performance gas-diffusion electrode are given by (10,33–38) where it has generally been concluded that the reaction layer should be optimized to contain a large number of catalytic clusters in the electrolyte and a large number of gas dissolving sites. Typically, multilayer electrodes are used as shown in Fig. 2 where each electrode contains a gas diffusion region consisting of hydrophobic gaseous pores only, and a reaction region consisting of hydrophobic gas–filled pores as well as liquid–filled pores. The hydrophobicity in the electrodes is obtained by impregnating the porous electrodes with a wet-proofing agent such as teflon, polytetrafluoroethylene (PTFE), or wax which also serve as a binding material for the electrodes (10). The quantity and distribution of these wet–proofing agents have a strong effect on the fuel cell performance as shown by (11,39).

As the dissolved gases diffuse through the electrolyte, they electrochemically react according to the following reactions:

$$\text{Cathode}: \qquad O_2 + 2H_2O_{(l)} + 4e^- \rightarrow 4OH^- \qquad [1]$$

and

$$\text{Anode}: \qquad H_2 + 2OH^- \rightarrow 2H_2O_{(l)} + 2e^- \qquad [2]$$

Hence, the overall reaction is the production of water

$$\text{Total}: \qquad H_2 + \frac{1}{2}O_2 \rightarrow H_2O_{(l)} \qquad [3]$$

with the simultaneous liberation of electrical energy. There have been numerous investigations into the mechanism of the oxygen reduction reaction in alkaline solutions. The two more common mechanisms for oxygen reduction involve the production of peroxide as either an intermediate species (40–43) or as a reaction product (44,45). However, the kinetic parameters vary depending on the type of electrode substrate and

electrocatalyst (9,46–49) as well as on operating conditions such as concentration, pH, temperature, and oxygen partial pressure (50,51). Therefore, since too many factors influence the oxygen reduction mechanism, it will be assumed that the direct four electron transfer process, as given by Eq. [1], occurs in the oxygen electrode.

B. Phenomenological Equations

In order to investigate the performance of an alkaline fuel cell, the phenomena occurring in the separator and in the three-phases of the electrodes need to be described. Including all regions of the cell allows the anode and cathode to interact through the continuous distribution of the solution phase potential and the electrolyte concentration across the system. This interaction is impossible to investigate with a single electrode model. To account for the complexities of the microporous structures, porous electrode theory (17), is used as a basis to describe the electrodes. This theory allows the superimposition of two or more phases into a single, homogeneous continuum. Thus, the gas diffusion layers are described by a homogeneous continuum of gaseous-filled pores and solid electrode material. Similarly, the reaction layers can be described by superimposing the gaseous-filled and liquid-filled pores with the solid electrode particles.

To develop a complete model of the alkaline fuel cell, the various forms of resistance need to be considered. In the gas phase, the reactant gases (H_2 and O_2) diffuse via molecular diffusion through water vapor in their respective electrodes contributing to the gas phase diffusional resistances. Thus, the partial pressures of hydrogen (P_{H_2}), oxygen (P_{O_2}), and water vapor in the anode ($P^a_{H_2O}$) and cathode ($P^c_{H_2O}$), need to be determined. Electronic resistances occur through a potential drop in the anode (E_a) and cathode (E_c) while an ohmic resistance arises due to a varying solution phase potential (ϕ). To account for the liquid phase diffusional resistances, the concentrations of dissolved hydrogen (C_{H_2}) and dissolved oxygen (C_{O_2}) need to be determined. The electrolyte concentration (C_e) varies in the solution phase

contributing to the ionic resistance. Additionally, the volume average velocity ($\vec{v}$) needs to be determined in order to consider convective effects in the solution phase. The fundamental equations needed to solve these eleven dependent variables will now be described in their general form. After these generalized equations have been applied in each region of the fuel cell, the necessary boundary conditions will be developed.

A one dimensional mathematical model of the alkaline fuel cell can be developed by considering conservation of mass and charge, transport of species, and reaction kinetics in each of the regions of the fuel cell as shown in Fig. 2. The equation of continuity for species i can be written in the general form for a porous medium

$$\frac{\partial \epsilon C_i}{\partial t} = -\nabla \cdot \mathbf{N}_i + R_i^p + R_i^e \qquad (i = \mathrm{O_2}, \mathrm{H_2}, \mathrm{H_2O}, +, -, \mathrm{o}) \qquad [4]$$

where R_i^p and R_i^e represent rates of production for material that is "brought in" from across a phase boundary and for material that is produced from an electrochemical reaction, respectively. Since porous electrode theory is being used, the reaction rate terms are included throughout the electrode, as indicated in Eq. [4], instead of being treated as a boundary condition as done in agglomerate models. Note that the $+, -,$ and o (water) species in Eq. [4] correspond to the K^+ ions, OH^- ions, and solvent, respectively. Furthermore, the ∇ operator in Eq. [4] and in subsequent equations is represented by $\frac{\partial}{\partial z}$ where z is in the horizontal direction in reference to Fig. 2. The flux expression for species i, $\mathbf{N}_i$, depends on whether species i is in the gas or solution phase. In the gas phase, the Stefan-Maxwell equation can be simplified for a binary gas mixture of species i and j (52):

$$\nabla y_i = \sum_{j=1}^{2} \frac{RT}{P\mathcal{D}_{i,j}^g}(y_i \mathbf{N}_j - y_j \mathbf{N}_i) \quad (i, j = \mathrm{O_2 \text{ or } H_2}, \mathrm{H_2O}) \qquad [5]$$

where the effects of diffusion and convection are accounted for. The ionic flux expression (53)

$$\mathbf{N}_i = -\mathcal{D}_i^l \nabla C_i - z_i u_i F C_i \nabla \phi + C_i \vec{v} \qquad (i = \mathrm{O_2}, \mathrm{H_2}, +, -, \mathrm{o}) \qquad [6]$$

can be used to represent the transport of species i in the liquid-filled pores of the porous electrodes. This expression accounts for the diffusive, migration, and convective effects in the solution phase through the first, second, and third terms, respectively. Note that Eqs. [5] and [6] contain effective diffusivities, $\mathcal{D}_i$, which are related to the free stream diffusivities by a porosity and tortuosity factor:

$$\mathcal{D}_i = \frac{\epsilon D_i}{\tau} \qquad [7]$$

and the Nernst-Einstein relation is assumed to relate the mobility, u_i, to the diffusivity of species i,

$$u_i = \frac{\mathcal{D}_i^l}{RT} \qquad [8]$$

The electrochemical reaction rate per unit of electrode volume, $R_{i,e}$, is expressed for species i in the form:

$$R_i^e = -\frac{s_i a^l i}{nF} \qquad [9]$$

where the stoichiometric coefficients, s_i, are given by expressing the electrochemical reactions in the form

$$\sum_i s_i M^{z_i} \rightarrow ne^- \qquad [10]$$

The local current density, i, is expressed by the Butler-Volmer electrochemical rate expression

$$i = i^\circ \left[\prod_i \left(\frac{C_i}{C_i^r} \right)^{p_i} \exp\left(\frac{\alpha_a nF}{RT} \eta \right) - \prod_i \left(\frac{C_i}{C_i^r} \right)^{q_i} \exp\left(\frac{-\alpha_c nF}{RT} \eta \right) \right] \qquad [11]$$

where the overpotential, η, is given by

$$\eta = E - \phi - U_{ref} \qquad [12]$$

Note that Eq. [11] is used for the hydrogen oxidation and oxygen reduction reactions rather than Tafel expressions in order to account for the effects of the reactant and product concentrations over the entire range of potentials investigated.

The rate of production of hydrogen and oxygen gas into the electrolyte across a phase boundary, R_i^p, is approximated by

$$R_i^p = -a^g \mathcal{D}_i^l \left(\frac{H_i P_i - C_i}{\delta} \right) \qquad [13]$$

where H_i is Henry's law constant in mol/(cm^{3}atm) for species i, δ is the diffusion layer thickness, and a^g is the specific surface area of the gaseous pores. Note that the term, $a^g \mathcal{D}_i^l / \delta$, could be replaced by a mass transfer coefficient, but this may lessen the appeal of the functionality of the dissolution rate expression. This rate expression assumes that equilibrium will be established at the gas-liquid interface following a Henry's law expression.

These equations describe the physical phenomena believed to be occurring in the alkaline fuel cell and will now be applied to the specific regions of the fuel cell.

Gas Diffusion Regions

Each electrode contains a gas diffusion layer to prevent the electrolyte from weeping into the gas stream and to provide structural support to the electrode. It may be assumed that the hydrophobicity of the electrode will prevent any liquid from entering this region. Therefore, only hydrogen gas and water vapor will exist in the anode gas diffusion layer and only oxygen gas and water vapor will exist in the cathode gas diffusion layer. Additionally, the solid electrode material in the gas diffusion regions will experience an ohmic drop that follows Ohm's law. Hence, each gas diffusion region has three unknown variables: P_{H_2}, $P^a_{H_2O}$, and E_a for the anode layer and P_{O_2}, $P^c_{H_2O}$, and E_c for the cathode gas diffusion layer. In the gas diffusion regions, the reactant gases (H_2 or O_2) diffuse through water vapor from the gas channel/gas diffusion interface to the gas diffusion/reaction interface. The water

vapor in these regions comes from two sources: water vapor that enters the system with the reactant gases and the water vapor that evaporates from the electrolyte in the gas reaction regions. Thus, the water vapor itself can diffuse in or out of the gas diffusion regions depending on the inlet and reaction conditions. To properly account for the relative fluxes of reactant gas to water vapor needed in the Stefan-Maxwell expression, Eq. [5], a water balance is needed about the system. From the stoichiometry of the overall reaction, Eq. [3], the flux of hydrogen gas is related to the total flux of water leaving the system

$$N^g_{H_2} = -N^T_{H_2O} \qquad [14]$$

and similarly for oxygen gas:

$$N^g_{O_2} = -\frac{1}{2}N^T_{H_2O} \qquad [15]$$

Since the total flux of water vapor is simply the sum of the water fluxes that leave with the anode and cathode gas streams,

$$N^T_{H_2O} = N^a_{H_2O} + N^c_{H_2O} \qquad [16]$$

then a water fraction, f_a, can be defined that relates the amount of water that leaves through the anode to the total amount of water generated (54):

$$f_a = \frac{N^a_{H_2O}}{N^a_{H_2O} + N^c_{H_2O}} \qquad [17]$$

Similarly, a cathode fraction ($f_c = 1 - f_a$) can be defined which gives:

$$f_a = 1 - \frac{N^c_{H_2O}}{N^a_{H_2O} + N^c_{H_2O}} \qquad [18]$$

Equations [14], [16], and [17] can be combined to relate the flux of hydrogen gas to the flux of water vapor in the anode:

$$N^a_{H_2O} = -f_a N^g_{H_2} \qquad [19]$$

Similarly, Eqs. [15], [16], and [18] can be combined to give the relationship between the oxygen and water vapor flux in the cathode:

$$N^c_{H_2O} = -2(1 - f_a)N^g_{O_2} \qquad [20]$$

These flux ratios can be inserted into the convective term of the Stefan-Maxwell flux expression, Eq. [5], and combined with the equation of continuity, Eq. [4] (where R^p_i and R^e_i are zero since there are no reactions in this region), to give:

$$\frac{\partial \epsilon^g P_{\mathrm{H_2}}}{\partial t} = \nabla \cdot \left[\frac{\mathcal{D}^g_{\mathrm{H_2}} P^a_T}{P^a_{\mathrm{H_2O}} + f_a P_{\mathrm{H_2}}} \nabla P_{\mathrm{H_2}} \right] \qquad [21]$$

in the anode and

$$\frac{\partial \epsilon^g P_{\mathrm{O_2}}}{\partial t} = \nabla \cdot \left[\frac{\mathcal{D}^g_{\mathrm{O_2}} P^c_T}{P^c_{\mathrm{H_2O}} + 2(1 - f_a)P_{\mathrm{O_2}}} \nabla P_{\mathrm{O_2}} \right] \qquad [22]$$

in the cathode. Since no production or consumption of any kind occurs in the gas diffusion layers, the total pressure will be constant in each region

$$P^a_T = P_{\mathrm{H_2}} + P^a_{\mathrm{H_2O}} \qquad [23]$$

in the anode and

$$P^c_T = P_{\mathrm{O_2}} + P^c_{\mathrm{H_2O}} \qquad [24]$$

in the cathode.

The last dependent variables that need to be determined in the gas diffusion regions are the anode and cathode solid potentials, E_a and E_c, respectively. The ohmic drop in these regions can be described by Ohm's law:

$$\nabla E = -\frac{I}{\sigma} \qquad [25]$$

where σ is the conductivity of the electrode and I is the total cell current density. Since there are no electrochemical reactions in the gas diffusion region, then the

current density is constant so that the gradient of the current density is zero. Hence, the ohmic drop in the anode gas diffusion layer is given by

$$\nabla^2 E_a = 0 \qquad [26]$$

and similarly in the cathode gas diffusion region:

$$\nabla^2 E_c = 0 \qquad [27]$$

The steady-state forms of the governing equations for the anode gas diffusion region are summarized in Table I where the spatial dimension was made dimensionless by setting:

$$\xi = \frac{z}{L} \qquad [28]$$

Similarly, the steady-state forms of the cathode gas diffusion region's governing equations are shown in Table II.

Gas Reaction Regions

In addition to containing a gas diffusion layer, each electrode has a gas reaction layer where the electrochemical and dissolution reactions occur. The reactant gases (O_2 or H_2) diffuse through water vapor in the gas pores of the electrode while some of the gases dissolve into the liquid–filled pores. The dissolved gases further diffuse in the solution until they reach a reaction site where they react electrochemically. The electrochemical reactions are influenced by the electrolyte concentration, solution potential, solid electrode potentials, volume average velocity, and dissolved reactant gas concentrations. Thus, in the anode gas reaction region there are seven variables to solve for: C_e, ϕ, E_a, C_{H_2}, v, P_{H_2}, and $P^a_{H_2O}$. Similarly, there are seven unknown variables in the cathode gas reaction region: C_e, ϕ, E_c, C_{O_2}, v, P_{O_2}, and $P^c_{H_2O}$. The reactant gases in these layers will have the same flux expressions as developed in the gas diffusion regions. Since the gases dissolve into the electrolyte, the gas dissolution

Table I. Summary of governing equations for the anode gas diffusion region ($z_a < z < z_{ad}$).

$$\frac{\partial}{\partial \xi}\left(\frac{P_T^a}{P_{H_2O}^a + f_a P_{H_2}} \frac{\partial P_{H_2}}{\partial \xi}\right) = 0$$	[29]
$$P_T^a = P_{H_2} + P_{H_2O}^a$$	[30]
$$\frac{\partial^2 E_a}{\partial \xi^2} = 0$$	[31]

Table II. Summary of governing equations for the cathode gas diffusion region ($z_{cd} < z < z_c$).

$$\frac{\partial}{\partial \xi}\left(\frac{P_T^c}{P_{H_2O}^c + 2(1-f_a)P_{O_2}}\frac{\partial P_{O_2}}{\partial \xi}\right) = 0 \qquad [32]$$

$$P_T^c = P_{O_2} + P_{H_2O}^c \qquad [33]$$

$$\frac{\partial^2 E_c}{\partial \xi^2} = 0 \qquad [34]$$

rates are included in the equation of continuity. Combining Eqs. [4], [5], and [13] gives an expression for the hydrogen gas pressure

$$\frac{\partial \epsilon^g P_{H_2}}{\partial t} = \nabla \cdot \left(\frac{\mathcal{D}^g_{H_2}(P^a_{H_2O} + P_{H_2})}{P^a_{H_2O} + f_a P_{H_2}} \nabla P_{H_2} \right) - a^g_a \mathcal{D}^l_{H_2} RT \left(\frac{H_{H_2} P_{H_2} - C_{H_2}}{\delta_a} \right) \quad [35]$$

in the anode and an expression for the oxygen gas pressure

$$\frac{\partial \epsilon P_{O_2}}{\partial t} = \nabla \cdot \left(\frac{\mathcal{D}^g_{O_2}(P^c_{H_2O} + P_{O_2})}{P^c_{H_2O} + 2(1 - f_a) P_{O_2}} \nabla P_{O_2} \right) - a^g_c \mathcal{D}^l_{O_2} RT \left(\frac{H_{O_2} P_{O_2} - C_{O_2}}{\delta_c} \right) \quad [36]$$

in the cathode.

In order to account for the evaporation of water into the gaseous pores, linear correlations were developed to give the partial pressure of water as a function of KOH concentration and temperature (Appendix A):

$$P_{H_2O} = a_{H_2O} + b_{H_2O} \cdot C_e \quad [37]$$

where a_{H_2O} and b_{H_2O} are regression coefficients at a constant temperature. Since the electrolyte concentration varies in the liquid pores of the gas reaction regions, the water vapor pressure will also vary as given by Eq. [37] and which will influence the gas phase transport as given by Eqs. [35] and [36]. Note that these correlations assume that equilibrium will be established between the gas and liquid phases in the gas reaction regions.

The dissolved reactant gas concentrations are given by combining Eqs. [4], [6], [9], and [13] to give

$$\frac{\partial \epsilon^l C_{H_2}}{\partial t} = \mathcal{D}^l_{H_2} \nabla^2 C_{H_2} - \nabla \cdot \left(\vec{v} C_{H_2} \right) - \frac{i_a a^l_a}{2F} + a^g_a \mathcal{D}^l_{H_2} \left[\frac{H_{H_2} P_{H_2} - C_{H_2}}{\delta_a} \right] \quad [38]$$

for the dissolved hydrogen concentration in the anode gas reaction region and

$$\frac{\partial \epsilon^l C_{O_2}}{\partial t} = \mathcal{D}^l_{O_2} \nabla^2 C_{O_2} - \nabla \cdot \left(\vec{v} C_{O_2} \right) + \frac{i_c a^l_c}{4F} + a^g_c \mathcal{D}^l_{O_2} \left[\frac{H_{O_2} P_{O_2} - C_{O_2}}{\delta_c} \right] \quad [39]$$

for the dissolved oxygen concentration in the cathode gas reaction region. The local current densities in Eqs. [38] and [39] are expressed using the Butler-Volmer kinetic

expression, Eq. [11]:

$$i_a = i_a^{\circ}\left[\left(\frac{C_{\mathrm{H}_2}}{C_{\mathrm{H}_2}^r}\right)^{p_{\mathrm{H}_2}}\left(\frac{C_{\mathrm{e}}}{C_{\mathrm{e}}^r}\right)^{p_{\mathrm{e}}}\exp\left(\frac{\alpha_a^a n_a F}{RT}(E_a-\phi-U_a)\right)\right] - i_a^{\circ}\left[\exp\left(-\frac{\alpha_c^a n_a F}{RT}(E_a-\phi-U_a)\right)\right] \quad [40]$$

for the anodic current density and

$$i_c = i_c^{\circ}\left[\left(\frac{C_{\mathrm{e}}}{C_{\mathrm{e}}^r}\right)^{p_{\mathrm{e}}}\exp\left(\frac{\alpha_a^c n_c F}{RT}(E_c-\phi-U_c)\right)\right] - i_c^{\circ}\left[\left(\frac{C_{\mathrm{O}_2}}{C_{\mathrm{O}_2}^r}\right)^{q_{\mathrm{O}_2}}\exp\left(-\frac{\alpha_c^c n_c F}{RT}(E_c-\phi-U_c)\right)\right] \quad [41]$$

for the cathodic current density. The superscribed *r* variables pertain to the reference concentrations associated with either the cathodic, i_c°, or anodic, i_a°, exchange current densities. The reference potentials, U, for each electrochemical reaction are given as a function of temperature, electrolyte concentration, and the partial pressure of the reactant gas relative to a standard reversible hydrogen electrode as defined by (55)

$$U = U^{\theta} - \frac{RT}{nF}\sum_i s_i \ln\left(\frac{C_i}{\rho}\right) - U_{RE}^{\theta} + \frac{RT}{n_{RE}F}\sum_i s_{i,RE}\ln\left(\frac{C_{i,RE}}{\rho}\right) \quad [42]$$

where U^{θ} is the standard potential at temperature T and U_{RE}^{θ} is the reference potential, both relative to the standard hydrogen electrode which is defined to be zero for convenience. Hence, these reference potentials are

$$U_c = U_c^{\theta} - \frac{8.314\,T}{4F}\ln\left(\frac{C_{\mathrm{e}}^4}{P_{\mathrm{O}_2}}\right)\ (\mathrm{V}) \quad [43]$$

for the cathode and

$$U_a = U_a^{\theta} - \frac{8.314\,T}{2F}\ln\left(P_{\mathrm{H}_2}C_{\mathrm{e}}^2\right)\ (\mathrm{V}) \quad [44]$$

for the anode. The standard electrode potentials at temperature T are given by (56)

$$U_c^{\theta} = 0.4011 - (T-298.15)\,1.682\times10^{-3}\ (\mathrm{V}) \quad [45]$$

and

$$U_a^\theta = -0.828 - (T - 298.15)\, 8.360 \times 10^{-4}\ (\mathrm{V}) \qquad [46]$$

The concentrations of the ionic species, K^+ and OH^-, are expressed by combining the material balance, Eq. [4], the ionic flux, Eq. [6], and the electrochemical rate, Eq. [9]. Combining these equations for each ionic species gives

$$\frac{\partial \epsilon^l C_+}{\partial t} = \mathcal{D}_+ \nabla^2 C_+ + u_+ F \nabla \cdot (C_+ \nabla \phi) - \nabla \cdot \left(v^{\blacksquare} C_+\right) \qquad [47]$$

for the K^+ ions and

$$\frac{\partial \epsilon^l C_-}{\partial t} = \mathcal{D}_- \nabla^2 C_- - \frac{i\, a^l}{F} - u_- F \nabla \cdot (C_- \nabla \phi) - \nabla \cdot \left(v^{\blacksquare} C_-\right) \qquad [48]$$

for the OH^- ions in both the anode and cathode gas reaction regions. In Eq. [48], the $i\, a^l$ term is given by $i_a a_a^l$ for the anodic gas reaction region and by $i_c a_c^l$ for the cathodic gas reaction region. The electroneutrality condition

$$\sum_i z_i C_i = 0 \qquad [49]$$

can be used to relate the potassium and hydroxide ion concentrations in the solution phase, giving

$$C_{\mathrm{e}} = C_- = C_+ \qquad [50]$$

Equation [50] can be combined with Eqs. [47] and [48] to eliminate the K^+ and OH^- ion concentrations, giving:

$$\frac{\partial \epsilon^l C_{\mathrm{e}}}{\partial t} = \mathcal{D}_+ \nabla^2 C_{\mathrm{e}} + u_+ F \nabla \cdot (C_{\mathrm{e}} \nabla \phi) - \nabla \cdot \left(v^{\blacksquare} C_{\mathrm{e}}\right) \qquad [51]$$

and

$$\frac{\partial \epsilon^l C_{\mathrm{e}}}{\partial t} = \mathcal{D}_- \nabla^2 C_{\mathrm{e}} - \frac{i\, a^l}{F} - u_- F \nabla \cdot (C_{\mathrm{e}} \nabla \phi) - \nabla \cdot \left(v^{\blacksquare} C_{\mathrm{e}}\right) \qquad [52]$$

for the anode and cathode gas reaction regions.

An expression for the volume average velocity can be formulated by first multiplying the equation of continuity, Eq. [4], for each species i present in the solution by the partial molar volume (assumed constant) of each species

$$\bar{V}_i \frac{\partial \epsilon^l C_i}{\partial t} = \left[-\nabla \cdot \mathbf{N}_i + R_i^e + R_i^p \right] \bar{V}_i \quad (i = +, -, \circ, O_2, H_2) \tag{53}$$

and summed over all species resulting in

$$\begin{aligned} &\frac{\partial \left[\epsilon^l \left(\bar{V}_- C_- + \bar{V}_+ C_+ + \bar{V}_\circ C_\circ + \bar{V}_{H_2} C_{H_2} + \bar{V}_{O_2} C_{O_2} \right) \right]}{\partial t} = \\ &-\nabla \cdot \left(\mathbf{N}_- \bar{V}_- + \mathbf{N}_+ \bar{V}_+ + \mathbf{N}_\circ \bar{V}_\circ + \mathbf{N}_{O_2} \bar{V}_{O_2} + \mathbf{N}_{H_2} \bar{V}_{H_2} \right) \\ &+ R_-^e \bar{V}_- + R_+^e \bar{V}_+ + R_\circ^e \bar{V}_\circ + R_{O_2}^p \bar{V}_{O_2} + R_{H_2}^p \bar{V}_{H_2} \end{aligned} \tag{54}$$

Recognizing that

$$1 = \bar{V}_- C_- + \bar{V}_+ C_+ + \bar{V}_\circ C_\circ + \bar{V}_{H_2} C_{H_2} + \bar{V}_{O_2} C_{O_2} \tag{55}$$

and assuming that the partial molar volumes for oxygen and hydrogen are much smaller than for the electrolyte species, then Eq. [54] can be simplified to:

$$\begin{aligned} \frac{\partial \epsilon^l}{\partial t} &= -\nabla \cdot \left(\mathbf{N}_- \bar{V}_- + \mathbf{N}_+ \bar{V}_+ + \mathbf{N}_\circ \bar{V}_\circ \right) \\ &+ R_-^e \bar{V}_- + R_+^e \bar{V}_+ + R_\circ^e \bar{V}_\circ \end{aligned} \tag{56}$$

The volume average velocity, $\overset{\blacksquare}{v}$, defined by (52) is given as:

$$\overset{\blacksquare}{v} = \sum_i C_i v_i \bar{V}_i = \sum_i N_i \bar{V}_i \tag{57}$$

which can be inserted into Eq. [56] and combined with Eq. [9] to give

$$\frac{\partial \epsilon^l}{\partial t} = -\nabla \cdot \overset{\blacksquare}{v} - \left(s_- \bar{V}_- + s_+ \bar{V}_+ + s_\circ \bar{V}_\circ \right) \frac{i\, a^l}{nF} \tag{58}$$

Newman (57) makes the following assumption for a binary electrolyte

$$\nu_+ t_+^\circ \bar{V}_+ = \nu_- t_-^\circ \bar{V}_- \tag{59}$$

which can be combined with

$$1 = t_-^\circ + t_+^\circ \qquad [60]$$

and the partial molar volume of the electrolyte

$$\bar{V}_e = \nu_+ \bar{V}_+ + \nu_- \bar{V}_- \qquad [61]$$

to give

$$t_+^\circ \bar{V}_e = \nu_- \bar{V}_- \qquad [62]$$

and

$$t_-^\circ \bar{V}_e = \nu_- \bar{V}_+ \qquad [63]$$

Combining Eqs. [60], [62], and [63] with the number of electrons transferred

$$-n = s_+ z_+ + s_- z_- \qquad [64]$$

gives an expression relating the partial molar volume of the electrolyte to its dissociated ions

$$s_- \bar{V}_- + s_+ \bar{V}_+ = \frac{s_- \bar{V}_e}{\nu_-} + \frac{t_-^\circ \bar{V}_e n}{\nu_- z_-} \qquad [65]$$

Since the liquid phase porosity does not change with time for the type of electrochemical reactions occurring in the alkaline fuel cell, the time rate of change of the liquid phase porosity is zero. Thus, combining Eqs. [58] and [65] gives an expression for the volume average velocity.

$$\nabla \cdot \vec{v} = -\left(\frac{s_- \bar{V}_e}{\nu_-} + \frac{t_-^\circ \bar{V}_e n}{\nu_- z_-} + s_\circ \bar{V}_\circ \right) \frac{i\, a^l}{nF} \qquad [66]$$

Since the total current density obtained from the fuel cell is equal to the integral of the local current densities as generated by the reaction, then

$$I = -\int_0^{L_R} i\, a^l dz \qquad [67]$$

so that the potential drop is given by

$$\nabla^2 E_a = \frac{i_a a_a^l}{\sigma_a} \qquad [68]$$

for the anodic gas reaction layer and by

$$\nabla^2 E_c = \frac{i_c a_c^l}{\sigma_c} \qquad [69]$$

for the cathodic gas reaction layer where the anodic and cathodic current density expressions are given by Eqs. [40] and [41], respectively.

Using Eq. [28], these governing equations for the anode gas reaction region are shown in their steady-state form in Table III. Similarly, the steady-state governing equations for the cathode gas reaction region are shown in Table IV.

Separator

In the middle of the alkaline fuel cell there is a porous separator matrix that is assumed to contain only solid non-conducting material and liquid–filled pores. The separator allows the ionic and dissolved reactant species to diffuse between the anode and cathode regions. The five unknown variables in this region are C_e, ϕ, $\vec{v}$, C_{O_2}, and C_{H_2}. The same development previously presented for the ionic species in the gas reaction regions can be applied here. No electrochemical reactions occur in the separator so that Eqs. [51] and [52] simplify to

$$\frac{\partial \epsilon^l C_e}{\partial t} = \mathcal{D}_+ \nabla^2 C_e + u_+ F \nabla \cdot (C_e \nabla \phi) - \nabla \cdot \left(\vec{v} C_e\right) \qquad [86]$$

and

$$\frac{\partial \epsilon^l C_e}{\partial t} = \mathcal{D}_- \nabla^2 C_e - u_- F \nabla \cdot (C_e \nabla \phi) - \nabla \cdot \left(\vec{v} C_e\right) = 0 \qquad [87]$$

Unreacted dissolved gases from the gas reaction regions may diffuse into the separator. Combining Eqs. [4] and [6] and simplifying gives

$$\frac{\partial \epsilon^l C_{H_2}}{\partial t} = \mathcal{D}^l_{H_2} \nabla^2 C_{H_2} - \nabla \cdot \left(\vec{v} C_{H_2}\right) \qquad [88]$$

Table III. Summary of governing equations for the anode gas reaction region ($z_{ad} < z < z_{ar}$).

$$\frac{\mathcal{D}^g_{H_2}}{RTL^2}\frac{\partial}{\partial\xi}\left(\frac{P^a_{H_2O}+P_{H_2}}{P^a_{H_2O}+f_aP_{H_2}}\frac{\partial P_{H_2}}{\partial\xi}\right)-a^g_a\mathcal{D}^l_{H_2}\left[\frac{H_{H_2}P_{H_2}-C_{H_2}}{\delta_a}\right]=0 \qquad [70]$$

$$P^a_{H_2O}=a_{H_2O}+b_{H_2O}\,C_e \qquad [71]$$

$$\frac{\mathcal{D}^l_{H_2}}{L^2}\frac{\partial^2 C_{H_2}}{\partial\xi^2}-\frac{1}{L}\frac{\partial}{\partial\xi}\left(\overset{\blacksquare}{v}C_{H_2}\right)-\frac{i_aa^l_a}{2F}+a^g_a\mathcal{D}^l_{H_2}\left[\frac{H_{H_2}P_{H_2}-C_{H_2}}{\delta_a}\right]=0 \qquad [72]$$

$$\frac{\mathcal{D}_+}{L^2}\frac{\partial^2 C_e}{\partial\xi^2}+\frac{u_+F}{L^2}\left[C_e\frac{\partial^2\phi}{\partial\xi^2}+\frac{\partial C_e}{\partial\xi}\frac{\partial\phi}{\partial\xi}\right]-\frac{C_e}{L}\frac{\partial\overset{\blacksquare}{v}}{\partial\xi}-\frac{\overset{\blacksquare}{v}}{L}\frac{\partial C_e}{\partial\xi}=0 \qquad [73]$$

$$\frac{\mathcal{D}_-}{L^2}\frac{\partial^2 C_e}{\partial\xi^2}-\frac{i_aa^l_a}{F}-\frac{u_-F}{L^2}\left[C_e\frac{\partial^2\phi}{\partial\xi^2}+\frac{\partial C_e}{\partial\xi}\frac{\partial\phi}{\partial\xi}\right]-\frac{C_e}{L}\frac{\partial\overset{\blacksquare}{v}}{\partial\xi}-\frac{\overset{\blacksquare}{v}}{L}\frac{\partial C_e}{\partial\xi}=0 \qquad [74]$$

$$\frac{1}{L}\frac{\partial\overset{\blacksquare}{v}}{\partial\xi}=-\left(\frac{s_-\bar{V}_e}{\nu_-}+\frac{t^\circ_-\bar{V}_en_a}{\nu_-z_-}+s_o\bar{V}_o\right)\frac{a^l_ai_a}{n_aF} \qquad [75]$$

$$\frac{1}{L^2}\frac{\partial^2 E_a}{\partial\xi^2}=\frac{i_aa^l_a}{\sigma_a} \qquad [76]$$

where

$$i_a=i^\circ_a\left[\left(\frac{C_{H_2}}{C^r_{H_2}}\right)^{p_{H_2}}\left(\frac{C_e}{C^r_e}\right)^{p_e}\exp\left(\frac{\alpha^a_an_aF}{RT}(E_a-\phi-U_a)\right)\right] -i^\circ_a\left[\exp\left(-\frac{\alpha^a_cn_aF}{RT}(E_a-\phi-U_a)\right)\right] \qquad [77]$$

Table IV. Summary of governing equations for the cathode gas reaction region ($z_{cr} < z < z_{cd}$).

$$\frac{\mathcal{D}^g_{O_2}}{RTL^2}\frac{\partial}{\partial\xi}\left(\frac{P^c_{H_2O}+P_{O_2}}{P^c_{H_2O}+2(1-f_a)P_{O_2}}\frac{\partial P_{O_2}}{\partial\xi}\right)-a^g_c\mathcal{D}^l_{O_2}\left[\frac{H_{O_2}P_{O_2}-C_{O_2}}{\delta_c}\right]=0 \qquad [78]$$

$$P^c_{H_2O}=a_{H_2O}+b_{H_2O}\,C_e \qquad [79]$$

$$\frac{\mathcal{D}^l_{O_2}}{L^2}\frac{\partial^2 C_{O_2}}{\partial\xi^2}+\frac{i_c a^l_c}{4F}+a^g_c\mathcal{D}^l_{O_2}\left[\frac{H_{O_2}P_{O_2}-C_{O_2}}{\delta_c}\right]-\frac{C_{O_2}}{L}\frac{\partial\bar{v}}{\partial\xi}-\frac{\bar{v}}{L}\frac{\partial C_{O_2}}{\partial\xi}=0 \qquad [80]$$

$$\frac{\mathcal{D}_+}{L^2}\frac{\partial^2 C_e}{\partial\xi^2}+\frac{u_+F}{L^2}\left[C_e\frac{\partial^2\phi}{\partial\xi^2}+\frac{\partial C_e}{\partial\xi}\frac{\partial\phi}{\partial\xi}\right]-\frac{C_e}{L}\frac{\partial\bar{v}}{\partial\xi}-\frac{\bar{v}}{L}\frac{\partial C_e}{\partial\xi}=0 \qquad [81]$$

$$\frac{\mathcal{D}_-}{L^2}\frac{\partial^2 C_e}{\partial\xi^2}-\frac{i_c a^l_c}{F}-\frac{u_-F}{L^2}\left[C_e\frac{\partial^2\phi}{\partial\xi^2}+\frac{\partial C_e}{\partial\xi}\frac{\partial\phi}{\partial\xi}\right]-\frac{C_e}{L}\frac{\partial\bar{v}}{\partial\xi}-\frac{\bar{v}}{L}\frac{\partial C_e}{\partial\xi}=0 \qquad [82]$$

$$\frac{1}{L}\frac{\partial\bar{v}}{\partial\xi}=-\left(\frac{s_-\bar{V}_e}{\nu_-}+\frac{t^\circ_-\bar{V}_e n_c}{\nu_- z_-}+s_o\bar{V}_o\right)\frac{a^l_c i}{n_c F} \qquad [83]$$

$$\frac{1}{L^2}\frac{\partial^2 E_c}{\partial\xi^2}=\frac{i_c a^l_c}{\sigma_c} \qquad [84]$$

where

$$i_c=i^\circ_c\left[\left(\frac{C_e}{C^r_e}\right)^{p_e}\exp\left(\frac{\alpha^c_a n_c F}{RT}(E_c-\phi-U_c)\right)\right] -i^\circ_c\left[\left(\frac{C_{O_2}}{C^r_{O_2}}\right)^{q_{O_2}}\exp\left(-\frac{\alpha^c_c n_c F}{RT}(E_c-\phi-U_c)\right)\right] \qquad [85]$$

for the dissolved hydrogen gas and

$$\frac{\partial \epsilon^l C_{O_2}}{\partial t} = \mathcal{D}^l_{O_2} \nabla^2 C_{O_2} - \nabla \cdot \left(\overset{\blacksquare}{v} C_{O_2} \right) \qquad [89]$$

for the dissolved oxygen gas. The volume average velocity can be simplified from Eqs. [66] by recognizing that the local current density term is zero in the separator giving

$$\nabla \overset{\blacksquare}{v} = 0 \qquad [90]$$

These five governing equations for the separator region are summarized in Table V in their steady-state forms.

C. Boundary Conditions

There are six boundaries in the alkaline fuel cell that need to be incorporated into the model. Referring to Fig. 2, these boundaries occur at the following interfaces: anode gas channel/anode gas diffusion layer (z_a), anode gas diffusion layer/anode gas reaction layer (z_{ad}), anode gas reaction layer/separator (z_{ar}), separator/cathode gas reaction layer (z_{cr}), cathode gas reaction layer/cathode gas diffusion layer (z_{cd}), cathode gas diffusion layer/cathode gas channel (z_c). Dirichlet or Neumann-type boundary conditions can be used to describe the phenomena that occur at these interfaces. These conditions will now be presented at each interface.

Anode Gas Channel/Anode Gas Diffusion Interface

The boundaries at this interface follow the Dirichlet-type conditions where the gaseous hydrogen and water vapor pressures are 'fixed' values. Since the total pressure at this interface remains constant, the partial pressures of hydrogen and water will vary so that the flux of water in the anode, Eq. [19], will be consistent with the fraction, f_a, and the total flux of water predicted by the cell current density:

$$\mathrm{N}^T_{H_2O} = \frac{I}{2F} \qquad [96]$$

Table V. Summary of governing equations for the separator region ($z_{ar} < z < z_{cr}$).

$$\frac{\mathcal{D}_+}{L_S^2}\frac{\partial^2 C_e}{\partial \xi^2} + \frac{u_+ F}{L_S^2}\left[C_e\frac{\partial^2 \phi}{\partial \xi^2} + \frac{\partial C_e}{\partial \xi}\frac{\partial \phi}{\partial \xi}\right] - \frac{C_e}{L_S}\frac{\partial v^{\blacksquare}}{\partial \xi} - \frac{v^{\blacksquare}}{L_S}\frac{\partial C_e}{\partial \xi} = 0 \qquad [91]$$

$$\frac{\mathcal{D}_-}{L_S^2}\frac{\partial^2 C_e}{\partial \xi^2} - \frac{u_- F}{L_S^2}\left[C_e\frac{\partial^2 \phi}{\partial \xi^2} + \frac{\partial C_e}{\partial \xi}\frac{\partial \phi}{\partial \xi}\right] - \frac{C_e}{L_S}\frac{\partial v^{\blacksquare}}{\partial \xi} - \frac{v^{\blacksquare}}{L_S}\frac{\partial C_e}{\partial \xi} = 0 \qquad [92]$$

$$\frac{\partial v^{\blacksquare}}{\partial \xi} = 0 \qquad [93]$$

$$\frac{\mathcal{D}^l_{H_2}}{L_S^2}\frac{\partial^2 C_{H_2}}{\partial \xi^2} - \frac{C_{H_2}}{L_S}\frac{\partial v^{\blacksquare}}{\partial \xi} - \frac{v^{\blacksquare}}{L_S}\frac{\partial C_{H_2}}{\partial \xi} = 0 \qquad [94]$$

$$\frac{\mathcal{D}^l_{O_2}}{L_S^2}\frac{\partial^2 C_{O_2}}{\partial \xi^2} - \frac{C_{O_2}}{L_S}\frac{\partial v^{\blacksquare}}{\partial \xi} - \frac{v^{\blacksquare}}{L_S}\frac{\partial C_{O_2}}{\partial \xi} = 0 \qquad [95]$$

Hence, the water vapor pressure at this interface can be calculated by combining Eqs. [5], [14], [19], and [96] and solving for the water vapor pressure at the interface. Since the fraction of water leaving through the anode, f_a, and the predicted cell current density, I, influence how much water is produced, the water vapor pressure at this interface is given as a function of f_a and I. For the total pressure to remain constant, the hydrogen pressure is then given by

$$P_{H_2} = P_T^a - P_{H_2O}^a \qquad [97]$$

Since the model predicts the current for a given potential load, the anode potential at this interface can be arbitrarily set to any value. Hence, the anode potential, E_a, was set to zero at this interface. These boundary conditions are summarized in Table VI.

Anode Gas Diffusion/Anode Gas Reaction Interface

At this interface, boundary conditions are needed for seven unknown variables: P_{H_2}, $P_{H_2O}^a$, E_a, C_{H_2}, C_e, ϕ, and $\vec{v}$. The flux for the hydrogen gas as given by Eqs. [5] and [14] is continuous at this interface giving

$$\mathcal{D}_{H_2}^g \nabla P_{H_2} \Big|_D = \mathcal{D}_{H_2}^g \nabla P_{H_2} \Big|_R \qquad [101]$$

The partial pressure of water at this interface is given by the correlation developed earlier for the partial pressure of water above a KOH electrolyte, Eq. [37]. The faradaic current density is continuous at this boundary as given by Eq. [25] resulting in

$$\sigma_D \nabla E_a \Big|_D = \sigma_R \nabla E_a \Big|_R \qquad [102]$$

The fluxes for the dissolved hydrogen and the K^+ and OH^- ions are zero since there exists a solution/solid phase interface at this boundary. Setting the ionic flux expression, Eq. [6], to zero for each of these species results in:

$$0 = \nabla C_e \Big|_R \qquad [103]$$

Table VI. Summary of boundary conditions at the anode gas channel/gas diffusion layer interface ($z = z_a$).

$P_{H_2} = P_T^a - P_{H_2O}^a$	[98]
$P_{H_2O}^a = f(f_a, I)$	[99]
$E_a = 0$	[100]

$$0 = \nabla\phi \Big|_R \qquad [104]$$

and

$$0 = \nabla C_{H_2} \Big|_R \qquad [105]$$

The volume average velocity at this interface is given by Eq. [66] where the local current density is zero since no electrochemical reactions take place at this interface. Also, since this boundary is a solid/solution phase interface, the volume average velocity has to be zero. Hence,

$$0 = \nabla \overset{\blacksquare}{v} \Big|_R \quad \text{and} \quad \overset{\blacksquare}{v} = 0 \qquad [106]$$

These boundary conditions are summarized in Table VII.

Table VII. Summary of boundary conditions at the anode gas diffusion/gas reaction interface ($z = z_{ad}$).

$$\left(\frac{\mathcal{D}^g_{H_2}}{L_D}\frac{\partial P_{H_2}}{\partial \xi}\right)\Bigg|_D = \left(\frac{\mathcal{D}^g_{H_2}}{L_R}\frac{\partial P_{H_2}}{\partial \xi}\right)\Bigg|_R \qquad [107]$$

$$P^a_{H_2O} = a_{H_2O} + b_{H_2O}\, C_e \qquad [108]$$

$$\left(\frac{\sigma_D}{L_D}\frac{\partial E_a}{\partial \xi}\right)\Bigg|_D = \left(\frac{\sigma_R}{L_R}\frac{\partial E_a}{\partial \xi}\right)\Bigg|_R \qquad [109]$$

$$0 = \frac{\partial C_{H_2}}{\partial \xi}\Bigg|_R \qquad [110]$$

$$0 = \frac{\partial C_e}{\partial \xi}\Bigg|_R \qquad [111]$$

$$0 = \frac{\partial \phi}{\partial \xi}\Bigg|_R \qquad [112]$$

$$0 = \frac{\partial v^{\blacksquare}}{\partial \xi}\Bigg|_R \quad \text{and} \quad v^{\blacksquare} = 0 \qquad [113]$$

Anode Gas Reaction/Separator Interface

Eight boundary conditions need to be specified at this interface: for P_{H_2}, $P^a_{H_2O}$, E_a, C_{H_2}, C_e, ϕ, $v^{\blacksquare}$, and C_{O_2}. Since hydrogen gas does not enter the separator, the flux of hydrogen gas, Eq. [5], is set to zero, giving

$$\nabla P_{H_2} \Big|_R = 0 \qquad [114]$$

and the partial pressure of water is again given by Eq. [37]. The faradaic current is zero at this boundary condition since the separator is non-conductive which simplifies from Eq. [25] to give

$$\nabla E_a \Big|_R = 0 \qquad [115]$$

The fluxes for the electrolyte species and dissolved hydrogen are continuous at this interface. Equating Eq. [6] as applied in the reaction layer and the separator layer for each species gives

$$\mathcal{D}^l_{H_2} \nabla C_{H_2} \Big|_R = \mathcal{D}^l_{H_2} \nabla C_{H_2} \Big|_S \qquad [116]$$

$$-\mathcal{D}_+ \nabla C_e \Big|_R - u_+ F C_e \nabla \phi \Big|_R = -\mathcal{D}_+ \nabla C_e \Big|_S - u_+ F C_e \nabla \phi \Big|_S \qquad [117]$$

and

$$-\mathcal{D}_- \nabla C_e \Big|_R + u_- F C_e \nabla \phi \Big|_R = -\mathcal{D}_- \nabla C_e \Big|_S + u_- F C_e \nabla \phi \Big|_S \qquad [118]$$

The volume average velocity at this interface is given by equating Eq. [66] as applied in the anode gas reaction layer to that applied in the separator region. Note that the local current density term is zero since no electrochemical reactions occur at this boundary.

$$\nabla v^{\blacksquare} \Big|_R = \nabla v^{\blacksquare} \Big|_S \qquad [119]$$

Unreacted dissolved oxygen in the cathode gas reaction layer can diffuse through the separator towards the anode gas reaction layer. Any dissolved oxygen in the anode gas

reaction layer would be quickly consumed by an electrochemical reaction and would not significantly influence the system at all. Hence, the dissolved oxygen concentration can be set to zero at the anode reaction layer/separator interface. These boundary conditions for the anode reaction/separator interface are summarized in Table VIII.

Separator/Cathode Gas Reaction Interface

Similar conditions are used at this interface as used at the anode gas reaction layer/separator interface. Eight boundary conditions are needed to describe these variables: P_{O_2}, $P^c_{H_2O}$, E_c, C_{O_2}, C_e, ϕ, $v^{\blacksquare}$, and C_{H_2}. Since the phenomenon at this boundary condition are similar to that at the anode reaction/separator interface, only a summary of the boundary conditions will be presented as shown in Table IX.

Cathode Gas Reaction/Cathode Gas Diffusion Interface

The boundary conditions at this interface are analogous to those at the anode gas diffusion/anode gas reaction interface. Thus, only a summary of the seven required boundary conditions (P_{O_2}, $P^c_{H_2O}$, E_c, C_{O_2}, C_e, ϕ, and $v^{\blacksquare}$) are presented in Table X.

Cathode Gas Diffusion/Cathode Gas Channel Interface

The boundary conditions at this interface are similar to those at the anode gas channel/anode gas diffusion interface except that the cathode potential is set to the applied cell potential. The partial pressures of oxygen and water are, again, allowed to vary at this boundary in an analogous manner as shown at the anode channel/gas diffusion interface. The boundary conditions for this interface are summarized in Table XI.

Table VIII. Summary of boundary conditions at the anode gas reaction/separator interface ($z = z_{ar}$).

$$\left.\frac{\partial P_{H_2}}{\partial \xi}\right|_R = 0 \qquad [120]$$

$$P^a_{H_2O} = a_{H_2O} + b_{H_2O}\, C_e \qquad [121]$$

$$\left.\frac{\partial E_a}{\partial \xi}\right|_R = 0 \qquad [122]$$

$$\left.\frac{\mathcal{D}^l_{H_2}}{L_R}\frac{\partial C_{H_2}}{\partial \xi}\right|_R = \left.\frac{\mathcal{D}^l_{H_2}}{L_S}\frac{\partial C_{H_2}}{\partial \xi}\right|_S \qquad [123]$$

$$\left.-\frac{\mathcal{D}_+}{L_R}\frac{\partial C_e}{\partial \xi}\right|_R \left.-\frac{u_+ F C_e}{L_R}\frac{\partial \phi}{\partial \xi}\right|_R = \left.-\frac{\mathcal{D}_+}{L_S}\frac{\partial C_e}{\partial \xi}\right|_S \left.-\frac{u_+ F C_e}{L_S}\frac{\partial \phi}{\partial \xi}\right|_S \qquad [124]$$

$$\left.-\frac{\mathcal{D}_-}{L_R}\frac{\partial C_e}{\partial \xi}\right|_R \left.+\frac{u_- F C_e}{L_R}\frac{\partial \phi}{\partial \xi}\right|_R = \left.-\frac{\mathcal{D}_-}{L_S}\frac{\partial C_e}{\partial \xi}\right|_S \left.+\frac{u_- F C_e}{L_S}\frac{\partial \phi}{\partial \xi}\right|_S \qquad [125]$$

$$\left.\frac{1}{L_R}\frac{\partial \blacksquare v}{\partial \xi}\right|_R = \left.\frac{1}{L_S}\frac{\partial \blacksquare v}{\partial \xi}\right|_S \qquad [126]$$

$$0 = C_{O_2}\Big|_S \qquad [127]$$

Table IX. Summary of boundary conditions at the cathode separator/gas reaction interface ($z = z_{cr}$).

$$0 = \frac{\partial P_{O_2}}{\partial \xi}\bigg|_R \qquad [128]$$

$$P^c_{H_2O} = a_{H_2O} + b_{H_2O}\, C_e \qquad [129]$$

$$0 = \frac{\partial E_c}{\partial \xi}\bigg|_R \qquad [130]$$

$$\frac{\mathcal{D}^l_{O_2}}{L_S}\frac{\partial C_{O_2}}{\partial \xi}\bigg|_S = \frac{\mathcal{D}^l_{O_2}}{L_R}\frac{\partial C_{O_2}}{\partial \xi}\bigg|_R \qquad [131]$$

$$-\frac{\mathcal{D}_+}{L_S}\frac{\partial C_e}{\partial \xi}\bigg|_S - \frac{u_+ F C_e}{L_S}\frac{\partial \phi}{\partial \xi}\bigg|_S = -\frac{\mathcal{D}_+}{L_R}\frac{\partial C_e}{\partial \xi}\bigg|_R - \frac{u_+ F C_e}{L_R}\frac{\partial \phi}{\partial \xi}\bigg|_R \qquad [132]$$

$$-\frac{\mathcal{D}_-}{L_S}\frac{\partial C_e}{\partial \xi}\bigg|_S + \frac{u_- F C_e}{L_S}\frac{\partial \phi}{\partial \xi}\bigg|_S = -\frac{\mathcal{D}_-}{L_R}\frac{\partial C_e}{\partial \xi}\bigg|_R + \frac{u_- F C_e}{L_R}\frac{\partial \phi}{\partial \xi}\bigg|_R \qquad [133]$$

$$\frac{1}{L_S}\frac{\partial v^{\blacksquare}}{\partial \xi}\bigg|_S = \frac{1}{L_R}\frac{\partial v^{\blacksquare}}{\partial \xi}\bigg|_R \qquad [134]$$

$$C_{H_2}\bigg|_S = 0 \qquad [135]$$

Table X. Summary of boundary conditions at the cathode gas reaction/gas diffusion interface ($z = z_{cd}$).

$\left.\frac{\mathcal{D}^g_{O_2}}{L_R}\frac{\partial P_{O_2}}{\partial \xi}\right\|_R = \left.\frac{\mathcal{D}^g_{O_2}}{L_D}\frac{\partial P_{O_2}}{\partial \xi}\right\|_D$	[136]
$P^c_{H_2O} = a_{H_2O} + b_{H_2O}\, C_e$	[137]
$\left.\frac{\sigma_R}{L_R}\frac{\partial E_a}{\partial \xi}\right\|_R = \left.\frac{\sigma_D}{L_D}\frac{\partial E_a}{\partial \xi}\right\|_D$	[138]
$\left.\frac{\partial C_{O_2}}{\partial \xi}\right\|_R = 0$	[139]
$\left.\frac{\partial C_e}{\partial \xi}\right\|_R = 0$	[140]
$\left.\frac{\partial \phi}{\partial \xi}\right\|_R = 0$	[141]
$\left.\frac{\partial v^{\blacksquare}}{\partial \xi}\right\|_R = 0$ and $v^{\blacksquare} = 0$	[142]

Table XI. Summary of boundary conditions at the cathode gas diffusion/gas channel interface ($z = z_c$).

$P_{O_2} = P_T^c - P_{H_2O}^c$	[143]
$P_{H_2O}^c = f(f_a, I)$	[144]
$E_c = E_{cell}$	[145]

D. Model Parameters

The alkaline fuel cell model requires various parameters that are specific to the cell structure, electrochemical reactions, and operating conditions. Table XII shows the electrochemical parameters used for the anode and cathode reactions for the base case conditions. The number of electrons transferred, charge numbers, and the stoichiometric coefficients for the cathode and anode reactions were taken from reactions [1] and [2], respectively, with the reactions following the form of Eq. [10]. Since the electrolyte is KOH, the dissociation constants of the ionic species are 1. The transfer coefficients for the hydrogen oxidation reaction in Table XII were estimated based on reported Tafel slopes of about 0.12 for the hydrogen evolution reaction (58). For the hydrogen evolution reaction, the Tafel slope, b, is

$$b = 2.3\frac{RT}{\alpha_c^a n_a F} \qquad [146]$$

giving $\alpha_c^a n_a$ of about 0.5. Assuming that

$$\alpha_a n + \alpha_c n = n \qquad [147]$$

then the product of the number of electrons transferred and the anodic transfer coefficient would be 1.5 as shown in Table XII. Note that this assumes the mechanism for hydrogen oxidation and hydrogen reduction are the same. For the oxygen reduction reaction, the transfer coefficients are based on experimentally measured Tafel slopes of about 0.045 (59) giving the transfer coefficients shown in Table XII. Since reliable transfer coefficient data are not readily available for various temperatures, concentrations, potentials, and electrocatalysts, these transfer coefficients are assumed constant.

Table XII also shows four adjustable parameters: the anodic and cathodic exchange transfer currents ($i_a^\circ \cdot a_a^l$ and $i_c^\circ \cdot a_c^l$) and the anodic and cathodic diffusional film areas (a_a^g/δ_a and a_c^g/δ_c). These parameters, as will be shown later, have a significant influence on the cell performance. For the base case conditions, these parameters were

Table XII. Electrochemical parameters for the anode and cathode reactions (base case conditions).

Anode		Cathode	
Parameter	Value	Parameter	Value
n_a	2	n_c	4
s_{H_2}	1	s_{O_2}	-1
s_-	2	s_-	4
s_o	-2	s_o	-1
z_-	-1	z_-	-1
z_+	1	z_+	1
ν_-	1	ν_-	1
ν_+	1	ν_+	1
p_{H_2}	2	q_{O_2}	0.5
p_{OH^-}	2.0	p_{OH^-}	2.0
$\alpha_a^a n_a$	1.5	$\alpha_a^c n_c$	2.5
$\alpha_c^a n_a$	0.5	$\alpha_c^c n_c$	1.5
$i_a^\circ \cdot a_a^l$	0.60 A/cm^3	$i_c^\circ \cdot a_c^l$	0.60 A/cm^3
a_a^g/δ_a	5 x 10^8 cm^{-2}	a_c^g/δ_c	5 x 10^8 cm^{-2}

selected to give performance curves similar to those obtained experimentally. As will be shown later, these parameters can be adjusted to fit the model to experimental polarization data.

Table XIII shows the structural and electrode parameters common to both the anode and cathode for the base case conditions. These parameters were selected as being representative of actual alkaline fuel cells. The base case operating conditions are shown in Table XIV where E_{cell} corresponds to the set cell potential.

In order to obtain realistic performance predictions for the alkaline fuel cell, the diffusion rates of the various species were determined as a function of concentration (or pressure) and temperature. This was necessary to accommodate the changing pressure in the electrodes and the varying electrolyte concentration across the system. Appendix A shows the correlations for the diffusivity and solubility parameters. The gas phase diffusivities for oxygen in water and hydrogen in water are determined as functions of temperature and pressure based on corresponding states principles. The diffusivities of dissolved oxygen and dissolved hydrogen in KOH are based on experimental measurements at different temperatures and concentrations. The ionic diffusivities for K^+ and OH^- ions were scaled from their dilute solution values to concentrated solutions for different temperatures. Setschenow salt effect parameters were used to determined the solubilities of hydrogen and oxygen gas in KOH as a function of temperature and concentration in the form of Henry's law constants. Based on these correlations, the reference concentrations necessary in the Butler-Volmer electrochemical reactions were determined using the base case conditions as shown in Table XV. Also shown in Table XV are the partial molar volumes of the electrolyte and the solvent (water). These partial molar volumes, assumed constant for this work, were obtained from (53)

$$\bar{V}_e = \frac{M_e - \frac{\partial \rho}{\partial C_e}}{\rho - C_e \frac{\partial \rho}{\partial C_e}} \qquad [148]$$

Table XIII. Structural and electrode parameters for the anode and cathode base case conditions.

Parameter	Value
Diffusion layer thickness, L_D	0.0250 cm
Reaction layer thickness, L_R	0.0050 cm
Separator thickness, L_S	0.0050 cm
Diffusion layer conductivity, σ_D	5.0 S/cm^2
Reaction layer conductivity, σ_R	5.0 S/cm^2
Diffusion layer gas porosity, ϵ_D^g	0.70
Reaction layer gas porosity, ϵ_R^g	0.10
Reaction layer liquid porosity, ϵ_R^l	0.60
Separator liquid porosity, ϵ_S	0.80
Cathode and anode tortuosity, τ	1.2
Separator tortuosity, τ	1.0

Table XIV. Base case operating conditions.

Parameter	Value
Initial electrolyte concentration, C_e	7 N
Temperature, T	80 °C
Inlet anode gas pressure, P_T^a	4.1 atm
Inlet cathode gas pressure, P_T^c	4.1 atm
Applied anode potential, E_a	0.0 V
Applied cathode potential, E_c	E_{cell}

for the partial molar volume of the electrolyte and

$$\bar{V}_o = \frac{M_o}{\rho - C_e \frac{\partial \rho}{\partial C_e}} \qquad [149]$$

for the partial molar volume of the solvent. The density of the electrolyte, as given by Akerlof and Bender (60), were correlated with temperature and concentration so that the change in density with concentration, $\partial\rho/\partial C_e$, could be determined. Using the base case operating conditions, the partial molar volumes for the electrolyte and the solvent were then calculated using Eqs. [148] and [149], respectively, as shown in Table XV. The transference number for the OH^- ion with respect to the solvent velocity, t°_-, introduced into the volume average velocity expression, Eq. [66], is determined by

$$t^\circ_- = \frac{\lambda_-}{\lambda_- + \lambda_+} \qquad [150]$$

where it is assumed constant over the electrolyte concentration range.

E. Method of Solution

The alkaline fuel cell model consists of 25 governing equations and 36 outer and internal boundary conditions. These equations are highly coupled and non-linear so that a numerical method is necessary to solve the resulting system of equations. The model equations were discretized by using second order accurate finite–difference approximations (61,62) in the governing equation regimes and by first order accurate finite differences expressions at the boundaries. This switch from second order to first order accurate finite difference expressions at boundaries was necessary to keep a stable solution of the system of equations. The resulting finite difference approximations have a banded matrix structure that can be solved by Newman's BAND(J) algorithm (53).

As the alkaline fuel cell approaches the limiting current density, the dissolved oxygen concentration becomes prohibitively too small ($\sim 10^{-9}$ mol/cm^3) which creates numerical difficulties with other terms that are of a much higher order of magnitude.

Table XV. Reference concentrations and partial molar volumes.

Parameter	Value
C_e^r	7.0 x 10^{-3} mol/cm^3
$C_{O_2}^r$	3.196 x 10^{-8} mol/cm^3
$C_{H_2}^r$	4.802 x 10^{-8} mol/cm^3
$\bar{V}_e$	18.591 cm^3/mol
$\bar{V}_o$	17.888 cm^3/mol
t_-°	0.696

The dissolved oxygen concentration had to be logarithmically transformed in order to achieve limiting current densities with the model. A logarithmically transformed variable, $C^*_{O_2}$, can be defined by

$$C^*_{O_2} = \ln\left(\frac{C_{O_2}}{C^r_{O_2}}\right) \qquad [151]$$

so that the derivatives become:

$$\frac{\partial C_{O_2}}{\partial z} = C^r_{O_2} \exp\left(C^*_{O_2}\right)\frac{\partial C^*_{O_2}}{\partial z} \qquad [152]$$

for the first derivative and

$$\frac{\partial^2 C_{O_2}}{\partial z^2} = C^r_{O_2} \exp\left(C^*_{O_2}\right)\left[\frac{\partial^2 C^*_{O_2}}{\partial z^2} + \left(\frac{\partial C^*_{O_2}}{\partial z}\right)^2\right] \qquad [153]$$

for the second derivative. Equations [152] and [153] can thus be substituted into the model equations for the dissolved oxygen concentration.

To prevent forcing the electrolyte out of the separator, the total pressure drop across the separator was forced to zero by adjusting the fraction f_a. Since a potentiostatic approach is used to model the alkaline fuel cell, the cell potential is set and the current density is calculated by the model. Convergency is obtained when the predicted cell current density is equal in all regions of the fuel cell as expressed by Eq. [25] for the electrode potentials in the gas diffusion regions, Eq. [67] for the integral of the local current densities in the gas reaction regions, and by

$$\frac{I}{nF} = -N^g_i \quad (i=O_2,H_2) \qquad [154]$$

for the gas diffusion regions and

$$I = F\sum z_i N_i \quad (i=+,-) \qquad [155]$$

for the separator.

F. Results and Discussion

The base case parameters shown in Tables XII and XV were used with the alkaline fuel cell model to calculate the eleven dependent variables as a function of cell potential and spatial domain. The cell potential was varied over the potential range of 1.1 to 0.7 V representative of the activation to concentration polarization range, respectively. These variables were then used to predict the current density as a function of cell potential.

Dependent Variable Profiles

To avoid forcing electrolyte out of the separator, the pressure drop across the separator region was forced to zero by adjusting the water vapor fraction, f_a, until the pressures at the separator/reaction interfaces are equal as shown in Figs. 3 and 4. These pressure distributions are influenced by the dissolution rate of the reactant gases and the evaporation rate of water. White *et al.* (32) showed that the electrode properties (*e.g.*, $a^g, a^l, \epsilon^g, \epsilon^l$) were dependent on the system pressure for a pore spectrum that follows a Gaussian distribution. Since the variation of the anode and cathode pressures are small, the assumption of constant electrode properties throughout their domains is reasonable. For the base case conditions used in evaluating the model, the system reaches its limiting current density at cell potentials lower than about 0.85 V. At these potentials, the total pressures along the separator/reaction interfaces become constant at an appreciable pressure which indicates that gas-phase molecular diffusion does not become a limiting factor in obtaining the limiting current densities. A similar conclusion was found by (39) who determined, experimentally, that the gas permeability was not as important as the wettability of the catalyst in limiting the current density. The inclusion of Knudsen diffusion in the gas phase may result in significant voltage losses as shown by (28), however, the importance of Knudsen diffusion is still somewhat questionable as shown by (11).

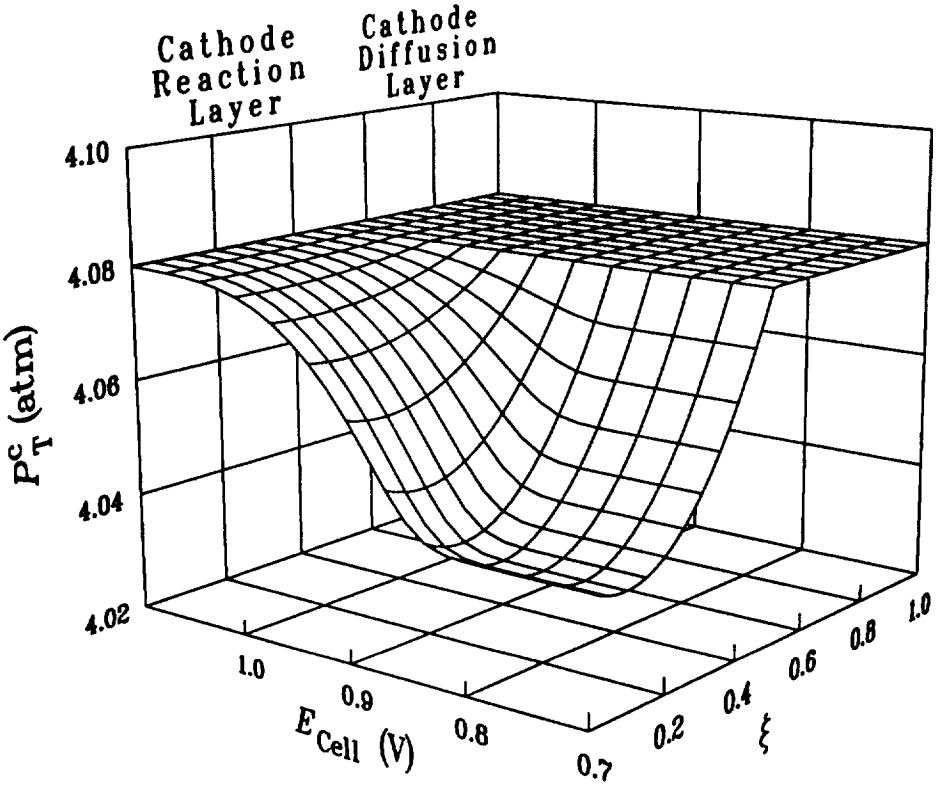

Figure 3. Total pressure distribution in the cathode.

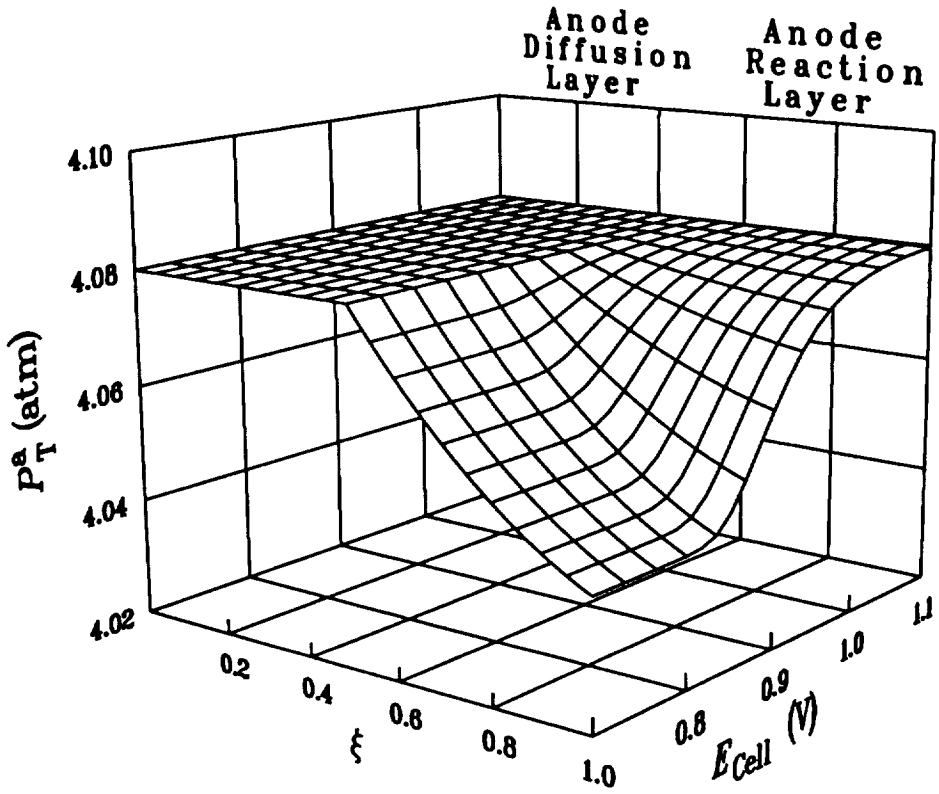

Figure 4. Total pressure distribution in the anode.

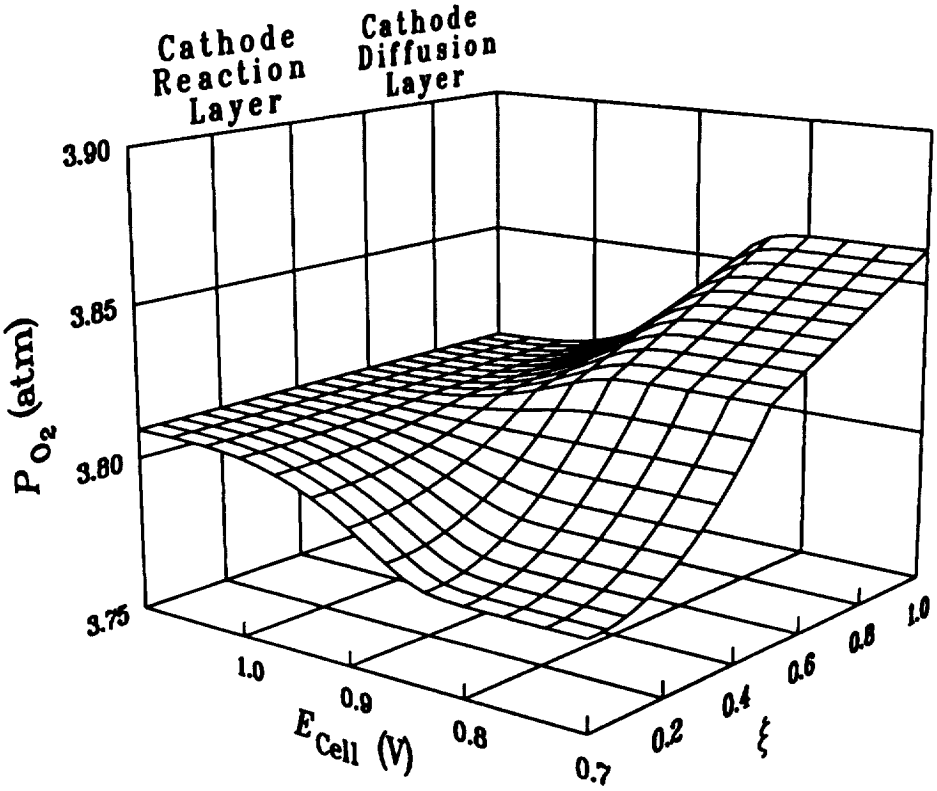

Figure 5. Variation of the oxygen pressure in the cathode.

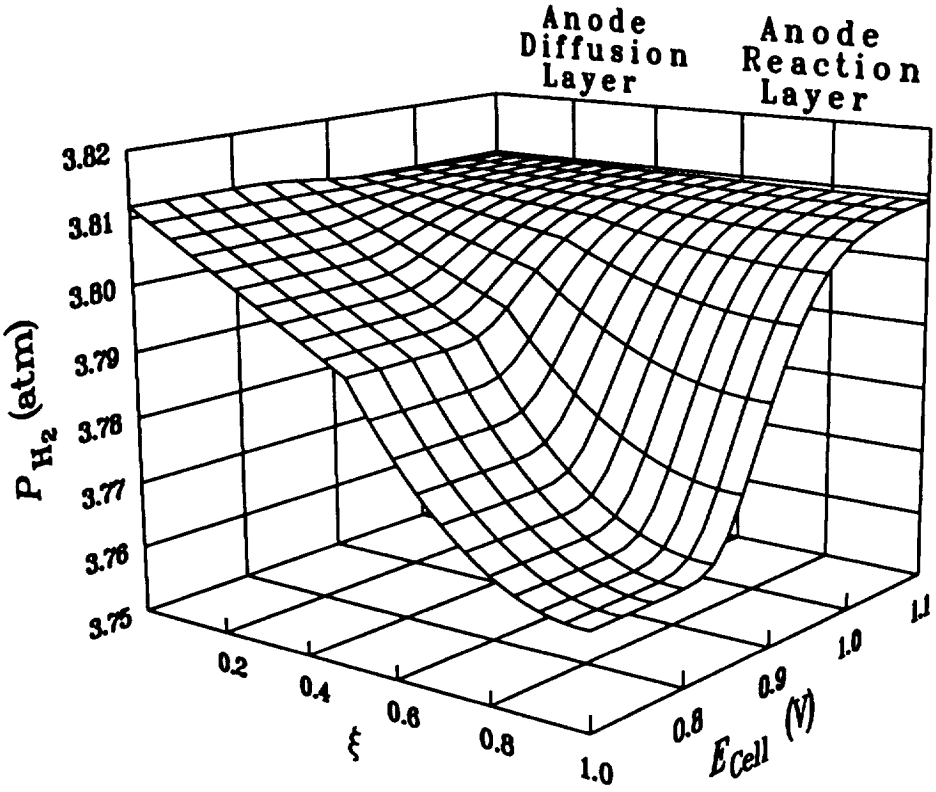

Figure 6. Variation of the hydrogen pressure in the anode.

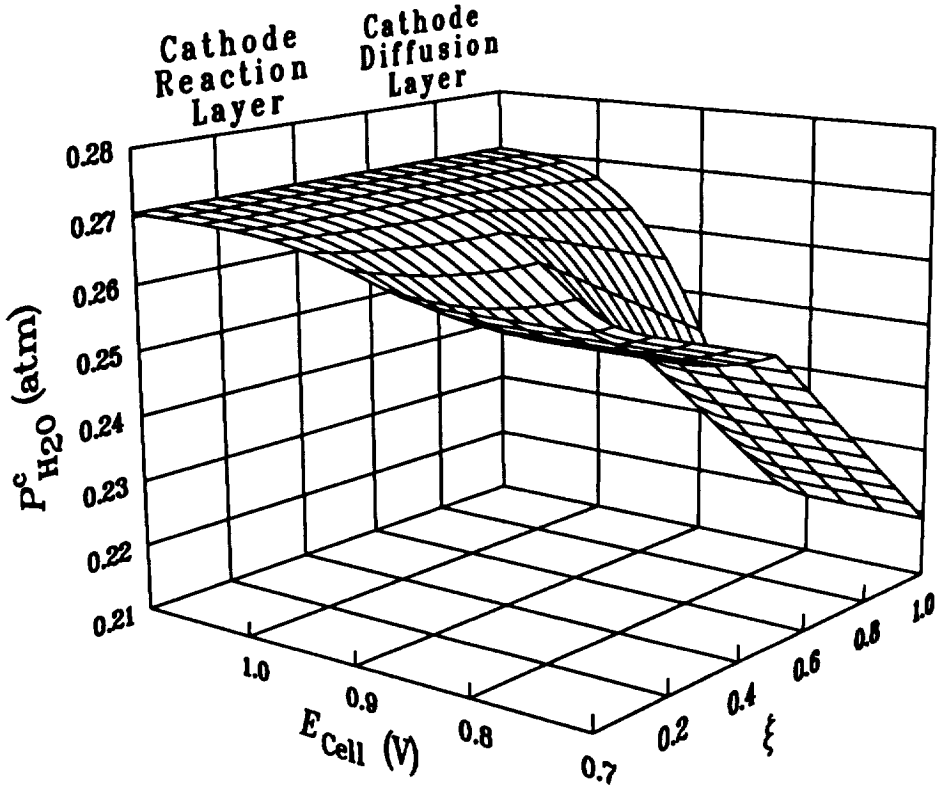

Figure 7. Distribution of the water vapor pressure in the cathode.

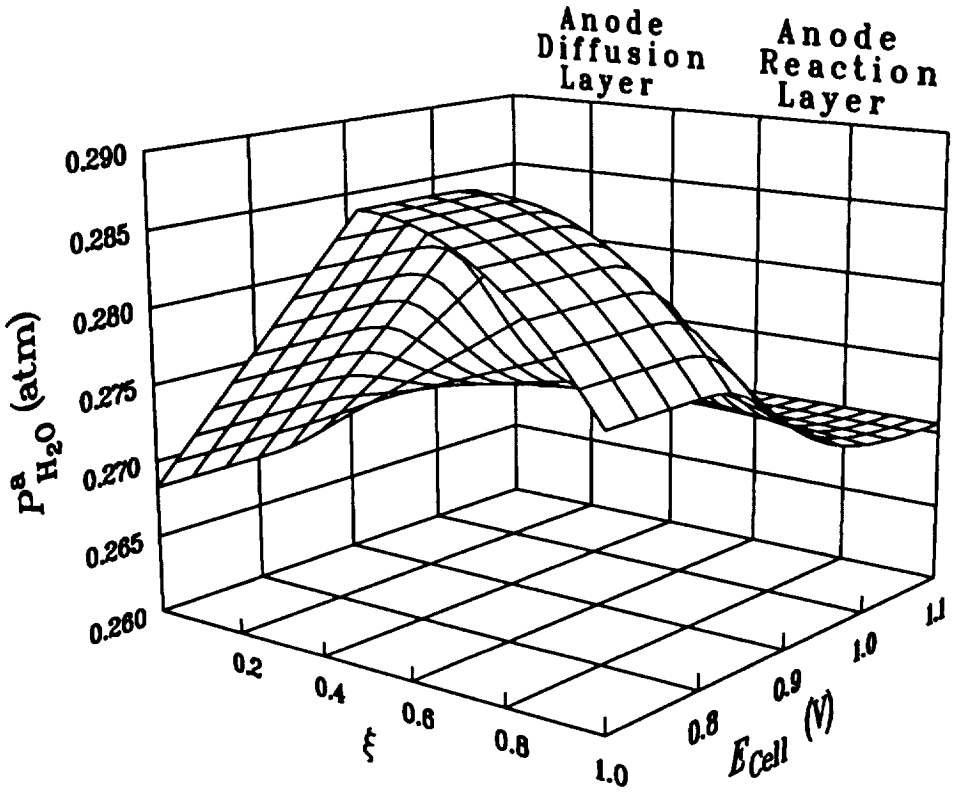

Figure 8. Distribution of the water vapor pressure in the anode.

The total pressure profiles can be separated into their respective partial pressure profiles as shown for oxygen (Fig. 5), hydrogen (Fig. 6), cathode water vapor (Fig. 7), and the anode water vapor (Fig. 8). As expected, the reactant gas pressures decrease very slightly in the diffusion and reactant layers at high cell potentials. However, at lower cell potentials, more of the reactant gases are consumed by the electrochemical reactions as evidenced by the steeper pressure drops. The reactant gas pressure profiles again confirm that at limiting current conditions the oxygen and hydrogen pressures are not a limiting factor since the gas pressures remain constant along the separator/reaction interfaces. The water vapor pressure profiles, Figs. 7 and 8, show that more water evaporates into the anode reaction layer than the cathode reaction layer.

The variation of the electrolyte concentration throughout the reaction layers and the separator is shown in Fig. 9 over the potential range of 0.7 to 1.1 V. Since the electrolyte does not circulate outside the fuel cell, the model assumes that no loss or production of the initial charge of electrolyte will occur. That is, the total number of moles of KOH is assumed to remain constant in the fuel cell. Previous models (23,28) for porous gas diffusion electrodes have typically neglected this electrolyte concentration variation. This simplification is reasonable at low current densities as shown by the relatively constant electrolyte concentration at high cell potentials in Fig. 9. However, at low cell potentials, an approximate 1.2 M change results in the electrolyte concentration from the anode to the cathode. This large variation has a significant impact on the evaporation of water and on the physical properties of the species present. Based on the equilibrium expression for the water vapor, Eq. [37], more water vapor will be present in the anode at low cell potentials than at high potentials. The accumulation of water vapor in the anode could flood the electrode at low cell potentials degrading the performance of the system. In the cathode regions, the larger electrolyte concentration at low cell potentials causes less water vapor to

be present which could dry out the electrode. Figure 9 also shows a fairly constant profile in the 0.7 to 0.8 V potential range indicating that the electrolyte concentration does not become a limiting factor in the limiting current region.

The solubility of oxygen and hydrogen gas in KOH, as given in terms of Henry's law constants, Eq. [171], are noticeably dependent on the electrolyte concentration as shown in Figs. 10 and 11, respectively. The dissolved oxygen concentration steadily decreases in the cathode reaction region as the cell potential is lowered obtaining an exceedingly small value (on the order of 1.0×10^{-7} M) at cell potentials lower than 0.85 V. This decrease in the dissolved oxygen concentration results from an increasing consumption of dissolved oxygen by the electrochemical reaction, Eq. [41], and by a decrease in the solubility with increasing electrolyte concentration. Similar results occur for the dissolved hydrogen concentration as shown in Fig. 11 where the dissolved hydrogen concentration attains a steady value of about 0.36 x 10–3 M at cell potentials lower than 0.85 V. Comparing Figs. 10 and 11 shows that the low concentration of dissolved oxygen at potentials lower than 0.85 V causes mass transfer limitations in the cathode. Therefore, in order to obtain high current densities, more dissolved oxygen is needed in the cathode. The model of a single electrode by (28) predicts that the dissolved oxygen diffusion contributes the least amount to the polarization losses. However, this result was obtained for a low current density of 200 mA/cm^2. At this current density, the AFC model predicts an appreciable amount of dissolved oxygen present in the electrolyte so that diffusional resistances of dissolved oxygen are not as significant as at the limiting current.

The anode and cathode both experience potential drops during operation as shown in Figs. 12 and 13. These profiles show that the potential drops are typically less than 10 mV for electrodes with high conductivities of 5 S/cm. Combining these solid electrode potentials with the solution phase and reference potentials through Eq. [12] gives the overpotential or driving force for each electrode. As shown in Fig. 14, the

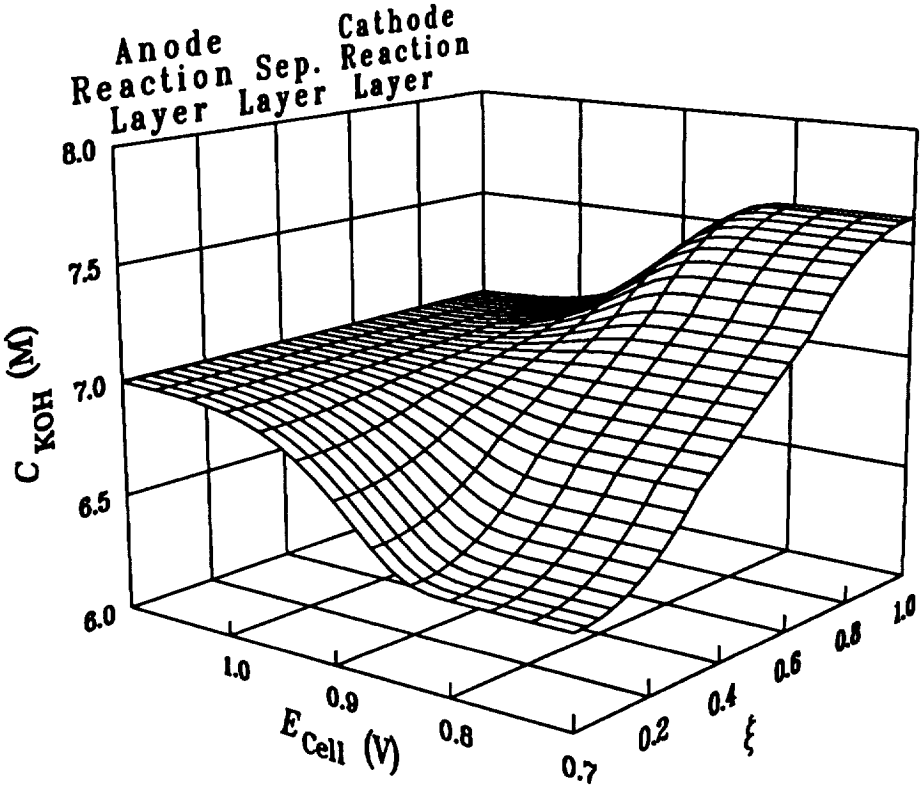

Figure 9. Variation of the electrolyte concentration in the AFC.

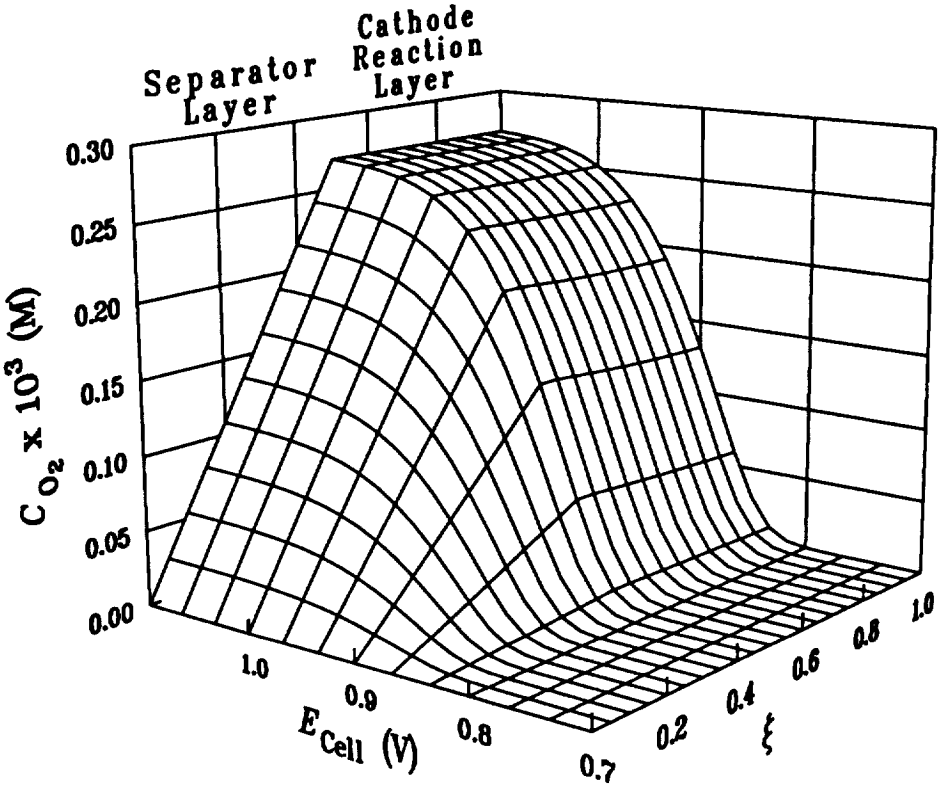

Figure 10. Dissolved oxygen concentration in the separator and cathode.

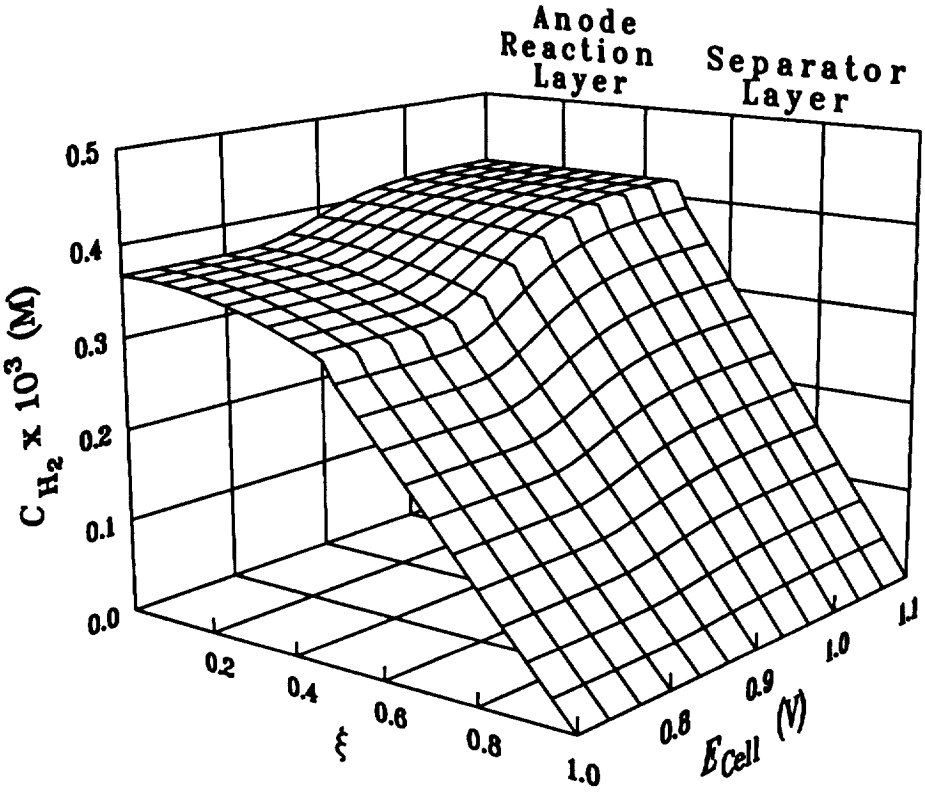

Figure 11. Dissolved hydrogen concentration in the anode and separator.

cathode requires a much larger overpotential than the anode at the same cell potential. The large overpotential in the cathode results from the low concentration of dissolved oxygen in the electrolyte. Attaining even larger overpotentials than shown in Fig. 14 for the cathode would be difficult since the dissolved oxygen concentration is extremely low. The transfer rates associated with these overpotentials are shown in Fig. 15 where the transfer rates increase in magnitude from the gas diffusion/reaction interfaces to the separator. The location and distribution of the reaction zone has been investigated by (29,39) where it is has been concluded that most of the electrochemical reaction occurs within a 0.01 cm distance in the catalyst layer as measured from the gas diffusion layer. However, in addition to obtaining the optimal reaction layer thicknesses, it is equally important to determine the distribution of the current throughout the reaction regions. As shown in Fig. 15, the transfer currents have a significant variation across the 0.005 cm thick reaction layers. Since the transfer currents are large near the separator, more electrocatalysts could be distributed near the diffusion/reaction interfaces to increase the reaction rates at these points. Optimizing the catalyst distribution with respect to the current density, amount of catalyst material, and cost could yield an improved electrode performance.

Parameter Effects on Polarization

For comparison purposes, the models's predicted polarization is shown with some experimental polarization data (63) for two sets of operating conditions in Fig. 16. The parameters shown in Table XII were used for the low temperature and pressure polarization in Fig. 16. Close agreement is obtained between the predicted and experimental polarization results. Since the complete operating conditions and fuel cell specifications are not given by (63) for the experimental results, an accurate comparison between the model and experimental results cannot be made. Parameter estimation could be used to fit the model to the experimental data if more experimental information were known. This would allow the model to accurately predict the fuel cell

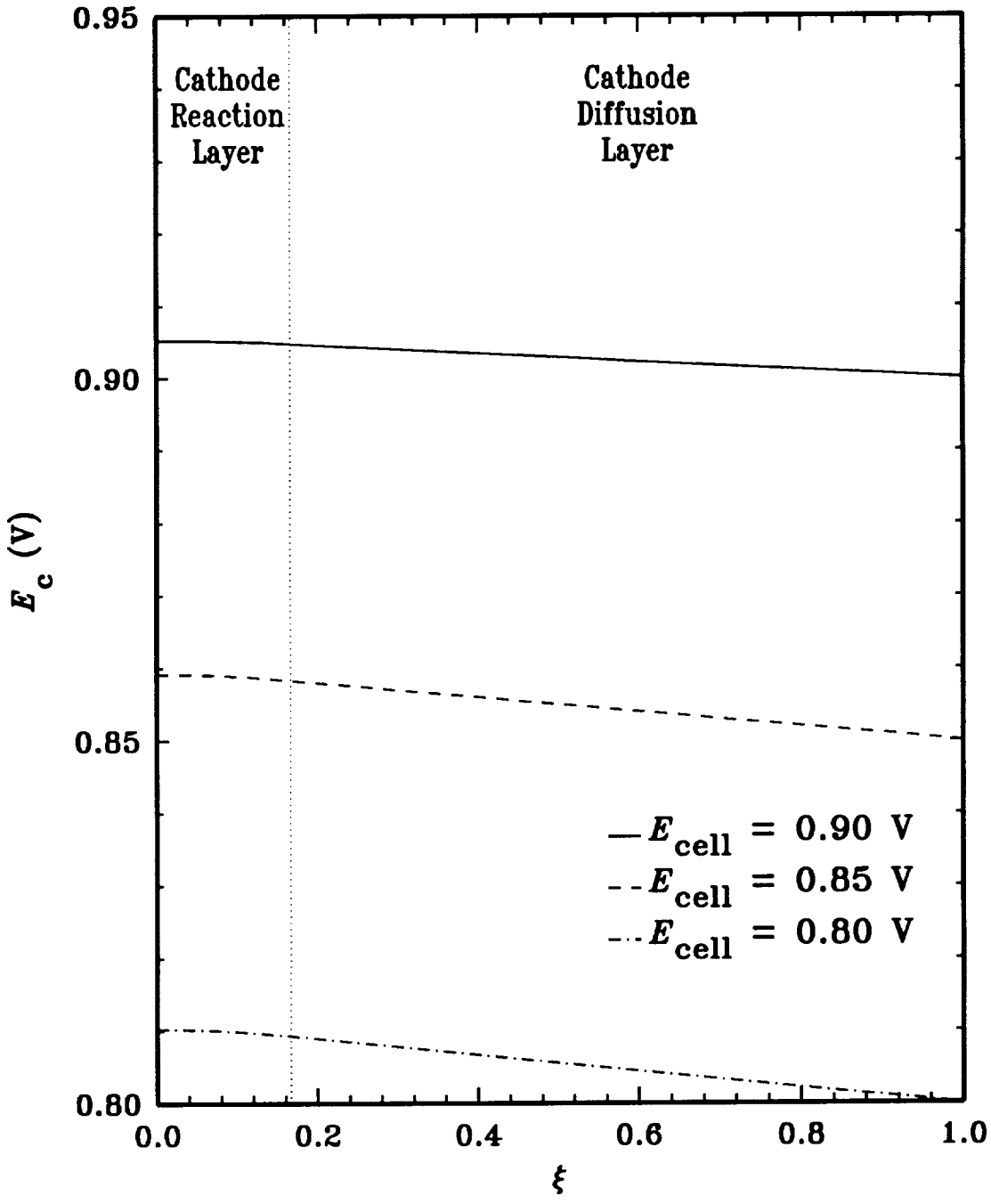

Figure 12. Solid potential variation in the cathode.

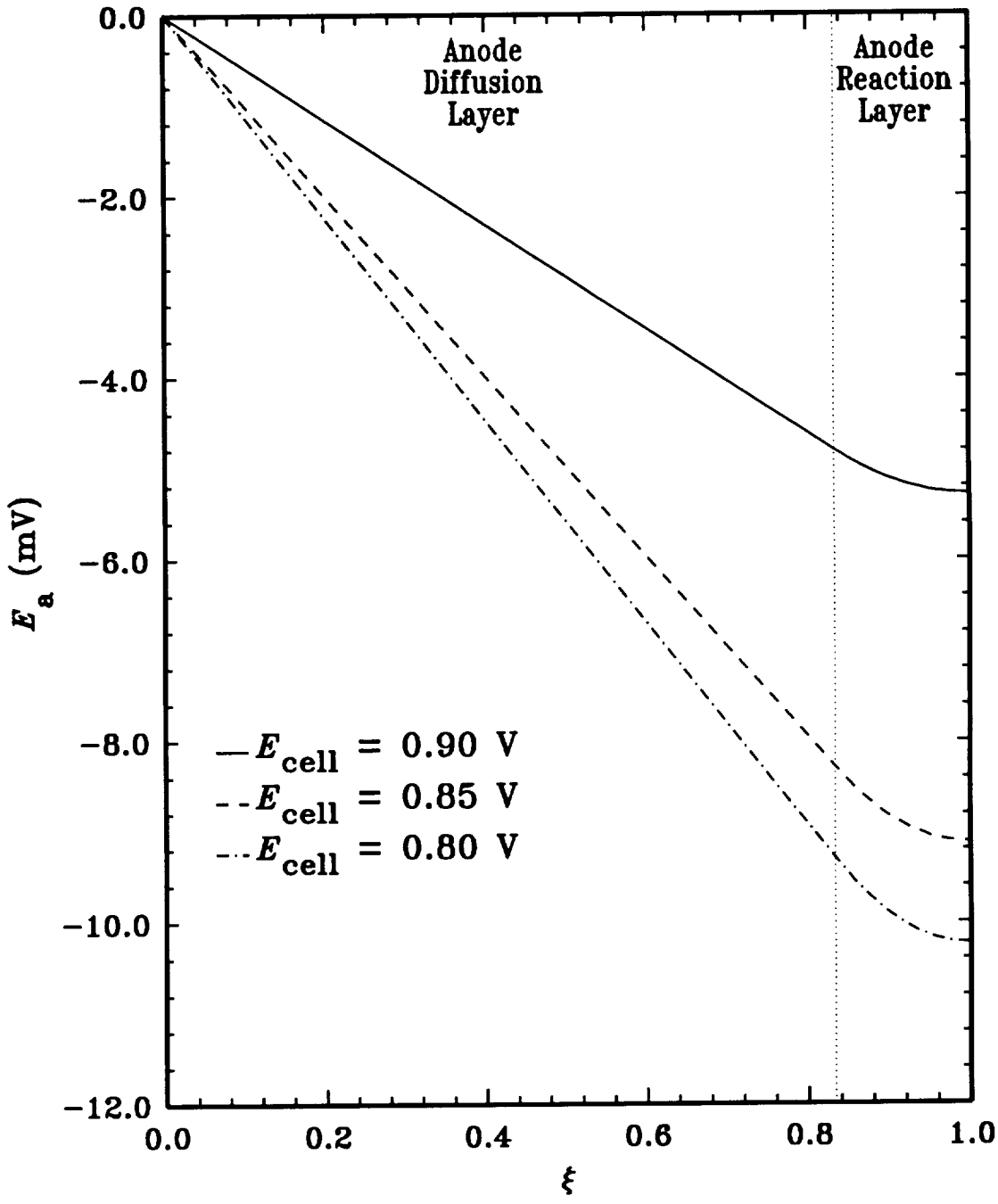

Figure 13. Solid potential variation in the anode.

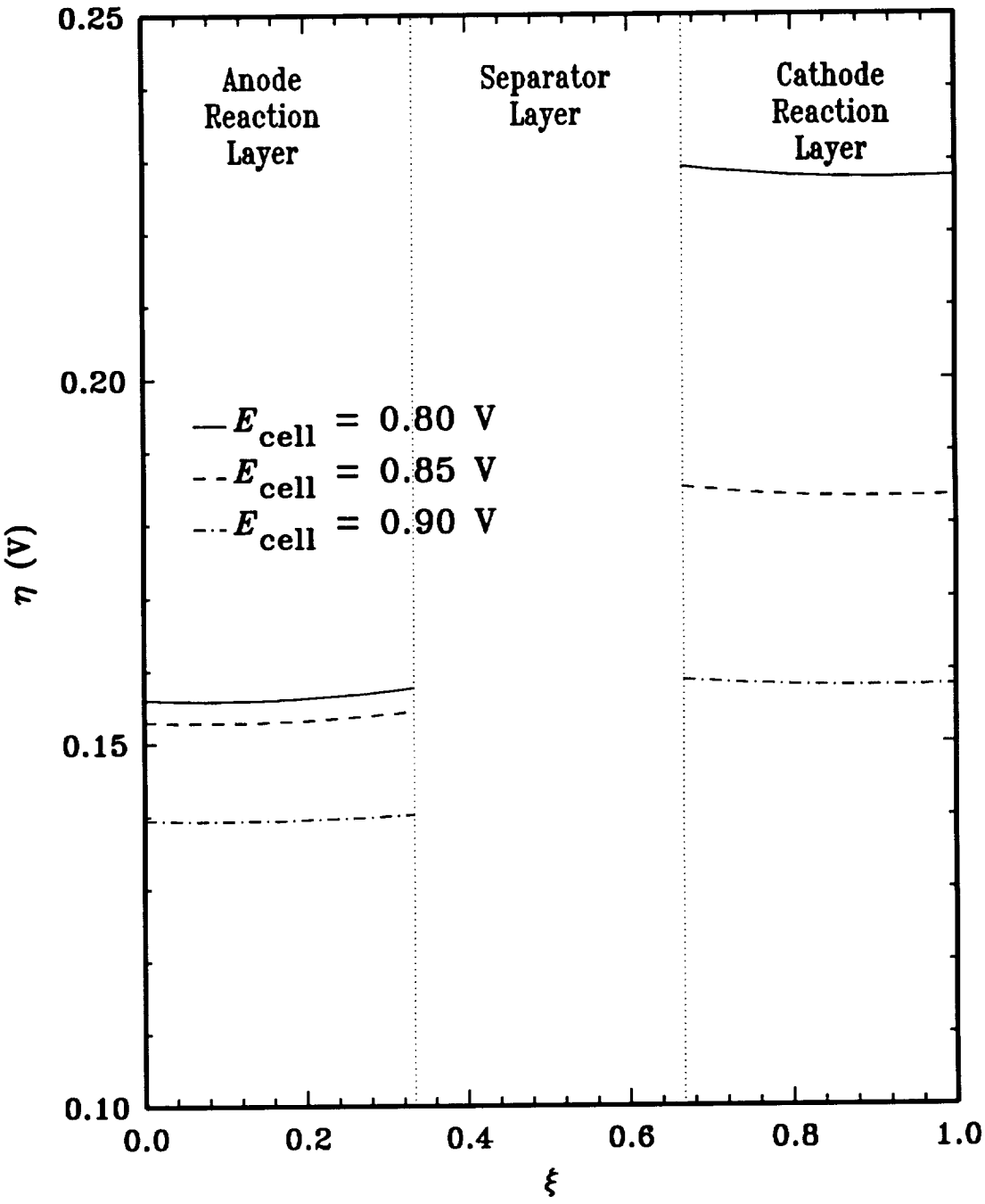

Figure 14. Comparison of the anode overpotential ($+\eta$) and cathode overpotential ($-\eta$) at various cell potentials.

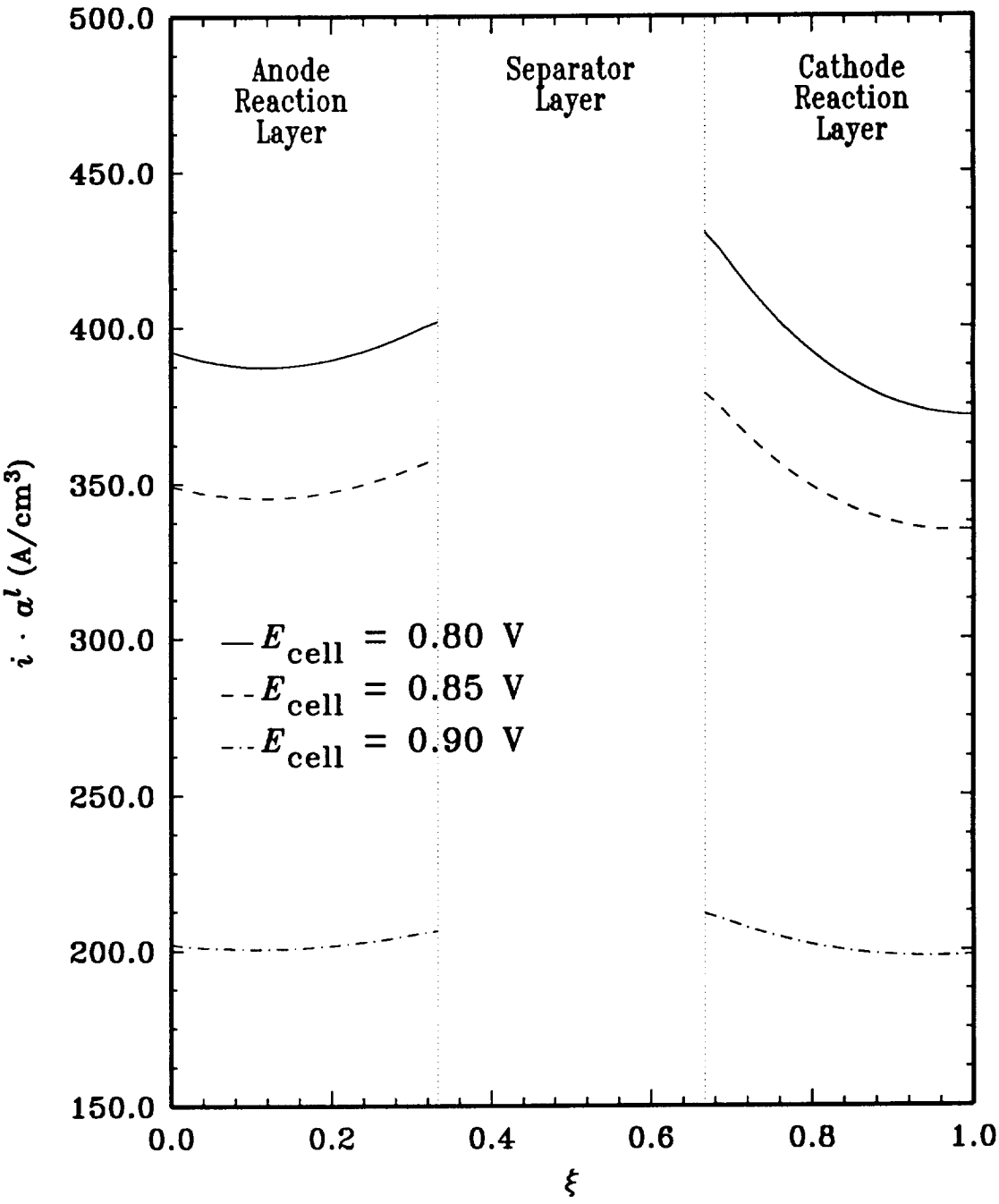

Figure 15. Variation of the anodic ($i_a \cdot a_a^l$) and cathodic ($-i_c \cdot a_c^l$) transfer currents for various cell potentials.

performance beyond the experimental domain. Note that the model predictions for the high pressure and temperature polarization in Fig. 16 only cover part of the experimental data range. This is due to some of the inaccuracies of the transport property correlations at high temperatures and pressures. Obtaining reliable experimental data for the various transport properties at high temperatures and pressures would improve the model's ability to predict high performance results for a wider range of operating conditions.

The model predictions in Fig. 16 are influenced by four parameters: the anodic and cathodic exchange transfer currents ($i_a^\circ \cdot a_a^l$ and $i_c^\circ \cdot a_c^l$) and the anodic and cathodic diffusional film areas (a_a^g/δ_a and a_c^g/δ_c), where the parameters shown in Table XII were used for the low temperature and pressure comparison. These parameters can significantly influence the polarization as shown in Fig. 17 for different values of the cathodic exchange transfer rate. This parameter is shown to influence the activation polarization region of the system without influencing the slope of the ohmic polarization region or the limiting current density at all. This suggests that an appreciable increase in the fuel cell performance up to the limiting current density can be obtained by increasing the electrocatalytic activity. Since the model predicts the same limiting current density for increasing exchange transfer currents, the dissolved oxygen concentration has to become even smaller to offset the higher exchange current densities. Similar results as shown in Fig. 17 were obtained for different anodic exchange transfer currents.

The effects of different diffusional film areas are shown in Fig. 18 for the cathode and in Fig. 19 for the anode where the base case conditions were used. Two benefits are achieved by increasing the cathodic diffusional film area parameter. First, the slope of the ohmic polarization is minimized allowing larger current densities to be obtained and, second, the limiting current density is increased. Similar inferences also apply to the anodic diffusional film area parameter. Increasing a_c^g/δ_c is associated directly

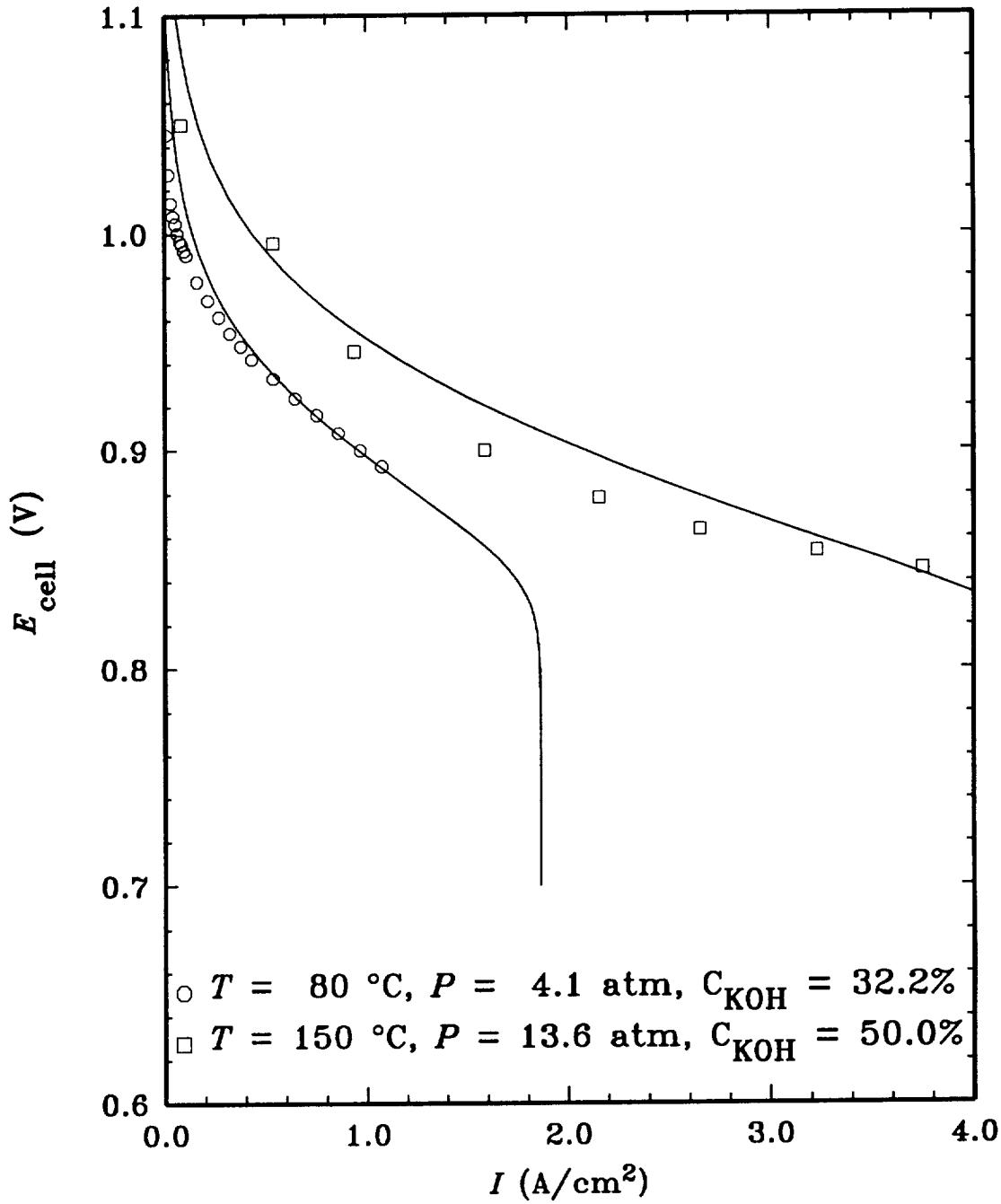

Figure 16. Comparison of model (—) and experimental predictions on the alkaline fuel cell polarization.

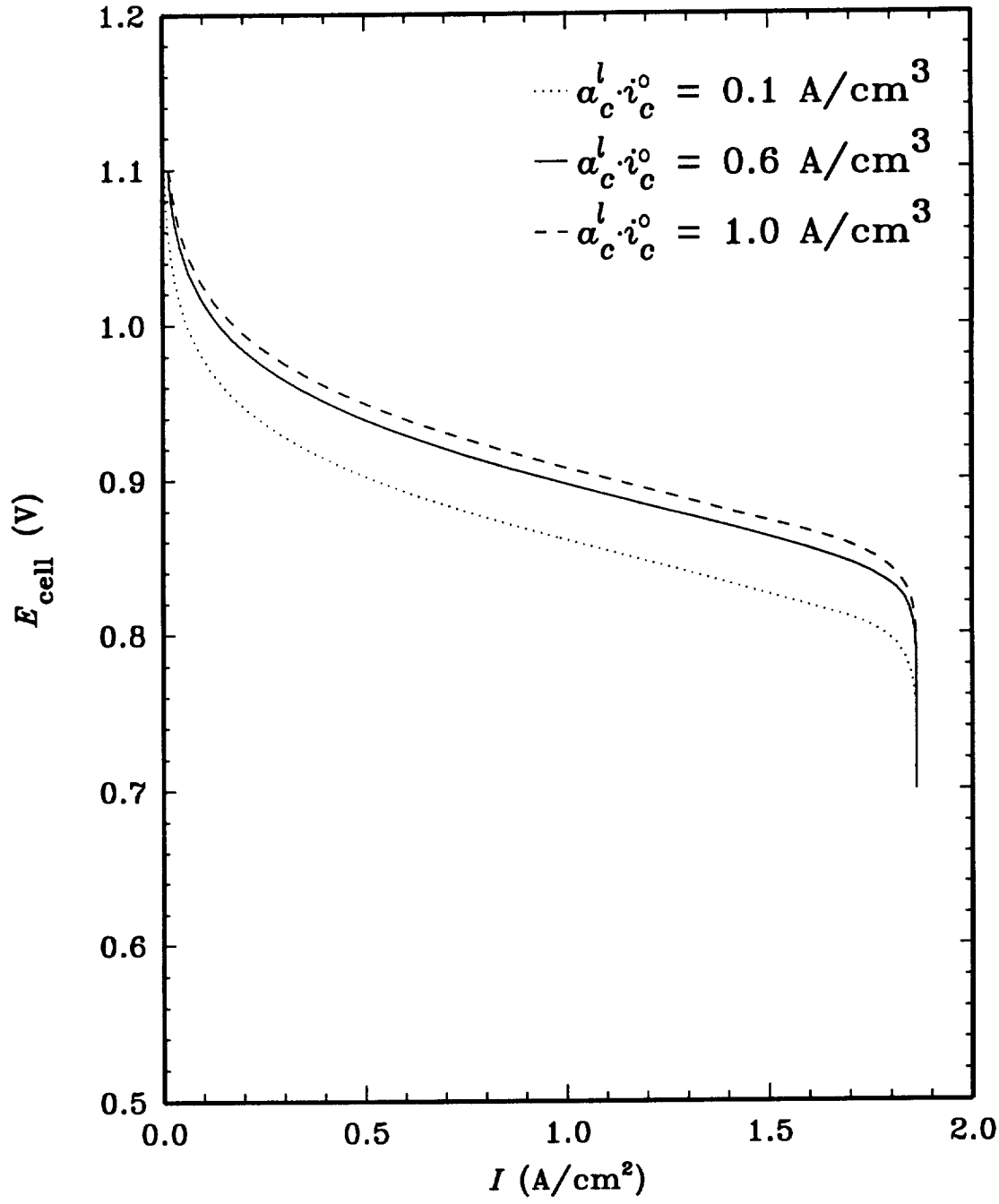

Figure 17. Effects of the cathodic exchange transfer current on the alkaline fuel cell polarization under the base case conditions.

with increasing the oxygen gas dissolution rate as given by Eq. [13]. Hence, in order to obtain high current densities, the number of gas-liquid sites should be increased allowing more gas to dissolve into the electrolyte. Note that this does not necessarily imply that more gaseous-filled pores should be present in the three-phase electrode. That is, increasing the gas phase porosity in the reaction layer, ϵ_R^g, will increase the number of gaseous filled pores, but not necessarily the gas phase specific surface area, a^g. Doubling the anode gas phase diffusional film area from the base case value of 5 x 10^8 cm^{-2} does not show any change from the base case polarization (shown by the solid line in Fig. 19). This simply indicates that the oxygen dissolution rate is limiting the performance. However, when a_a^g/δ_a is lowered to 1.0 x 10^8 cm^{-2}, the resulting performance decreases indicating that the hydrogen dissolution process is rate controlling. These results indicate that a significant interaction can occur between the anode and cathode in controlling the polarization. The ability to investigate the interaction of the anode, separator and cathode is one advantage to using a complete model of the alkaline fuel cell rather than using single electrode models as previously done.

The performance of the alkaline fuel cell is also dependent on the values of the transfer coefficients used in the Butler-Volmer kinetic expressions, Eqs. [40] and [41] as shown in Fig. 20 for different anodic and cathodic transfer coefficients. These parameters are shown to influence the polarization in an analogous manner as the cathodic and anodic exchange transfer currents. The determination of these transfer coefficients is important in order to obtain better model predictions.

Effects of Operating Conditions

The effect of increasing the total pressure in both the anode and cathode gas channels would increase the performance of the fuel cell as shown in Fig. 21 for three different pressures. Since earlier results showed that the dissolved oxygen concentration had a limiting effect on the performance, increasing the pressure allows

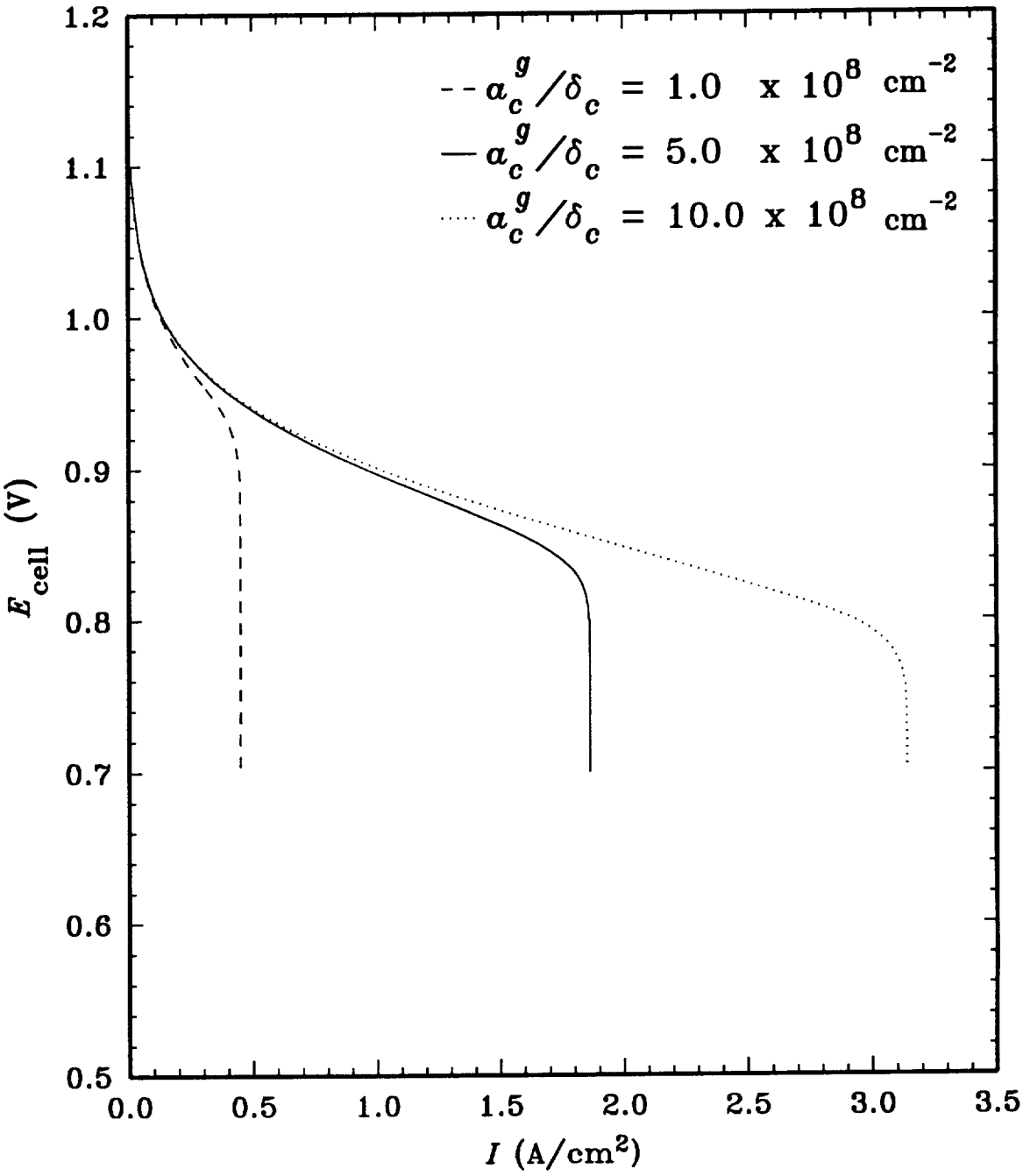

Figure 18. Influence of the cathodic diffusion film area on the fuel cell polarization evaluated under the base case conditions.

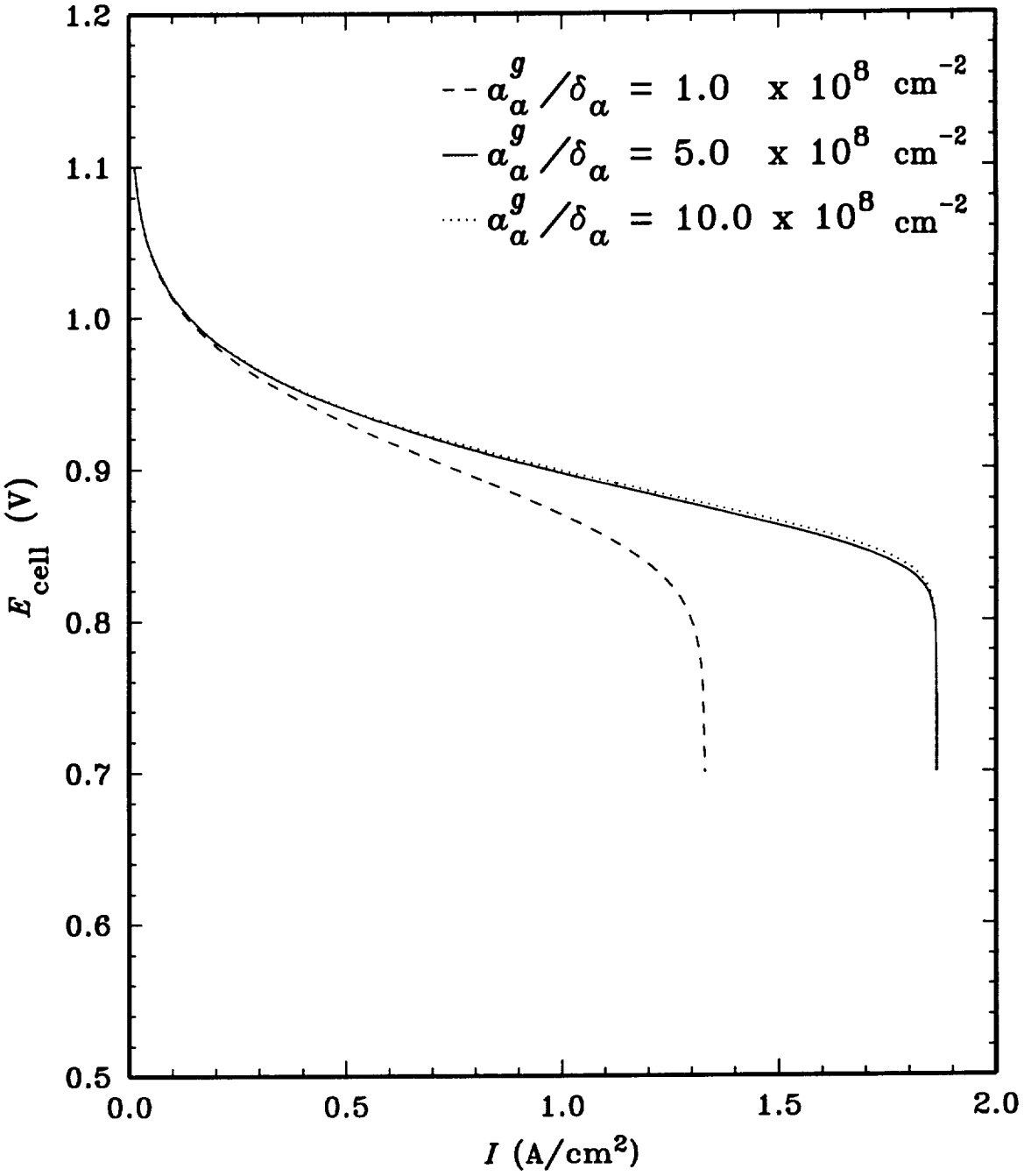

Figure 19. Influence of the anodic diffusion film area on the fuel cell polarization evaluated under the base case conditions.

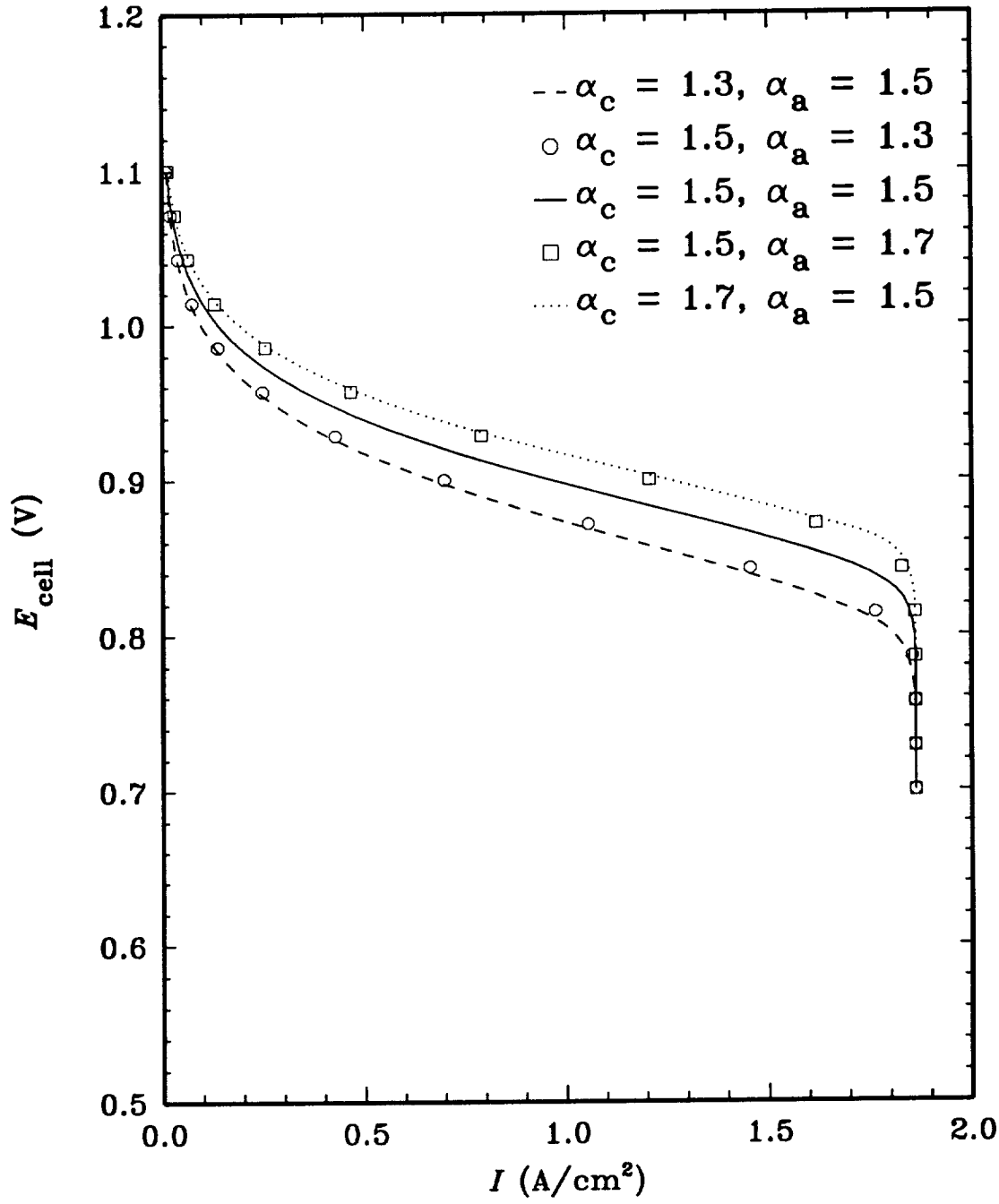

Figure 20. Effects of different anodic and cathodic transfer coefficients on the alkaline fuel cell polarization (base case conditions).

more gas to dissolve into the electrolyte as given by Henry's law, Eqs. [171] and [172], which increases the fuel cell performance. The model predictions give no apparent upper bound on the system pressure where the performance would start to degrade due to transport or kinetic effects.

Figure 22 shows the results of different system temperatures on the alkaline fuel cell performance. Increasing the temperature is shown to increase the activation polarization while extending the concentration polarization limit. As the system temperature is decreased, the limiting current density increases while the cell potential at the limiting current decreases. These results suggest that an optimal temperature might exist that is higher than 373 K that would give a maximum in the power density. Since the temperature has a significant impact on the cell performance, the inclusion of a thermal balance into a future alkaline fuel cell model could improve the model predictions.

The effects of different average electrolyte concentrations on the fuel cell performance are shown in Fig. 23 where a decreasing electrolyte concentration increases the performance. The average electrolyte concentration in most alkaline fuel cells is about 7 N (32%) since this concentration corresponds to the highest conductivity of the electrolyte. The model results in Fig. 23 apparently contradict this fact. The model presented here indicates that the dissolved oxygen concentration is a major factor in determining the fuel cell performance, based on the operating and cell parameters shown in Tables XII–XIV. Since the solubility of oxygen increases with a lowering of the electrolyte concentration, Eq. [171], a higher cell performance results when more oxygen dissolves into the electrolyte.

In order to determine the major limitations to the alkaline fuel cell performance, the base case conditions were used to examine the performance when certain forms of resistance were neglected as shown in Fig. 24 where the percent increase in the predicted current densities over the base case current densities are shown. To

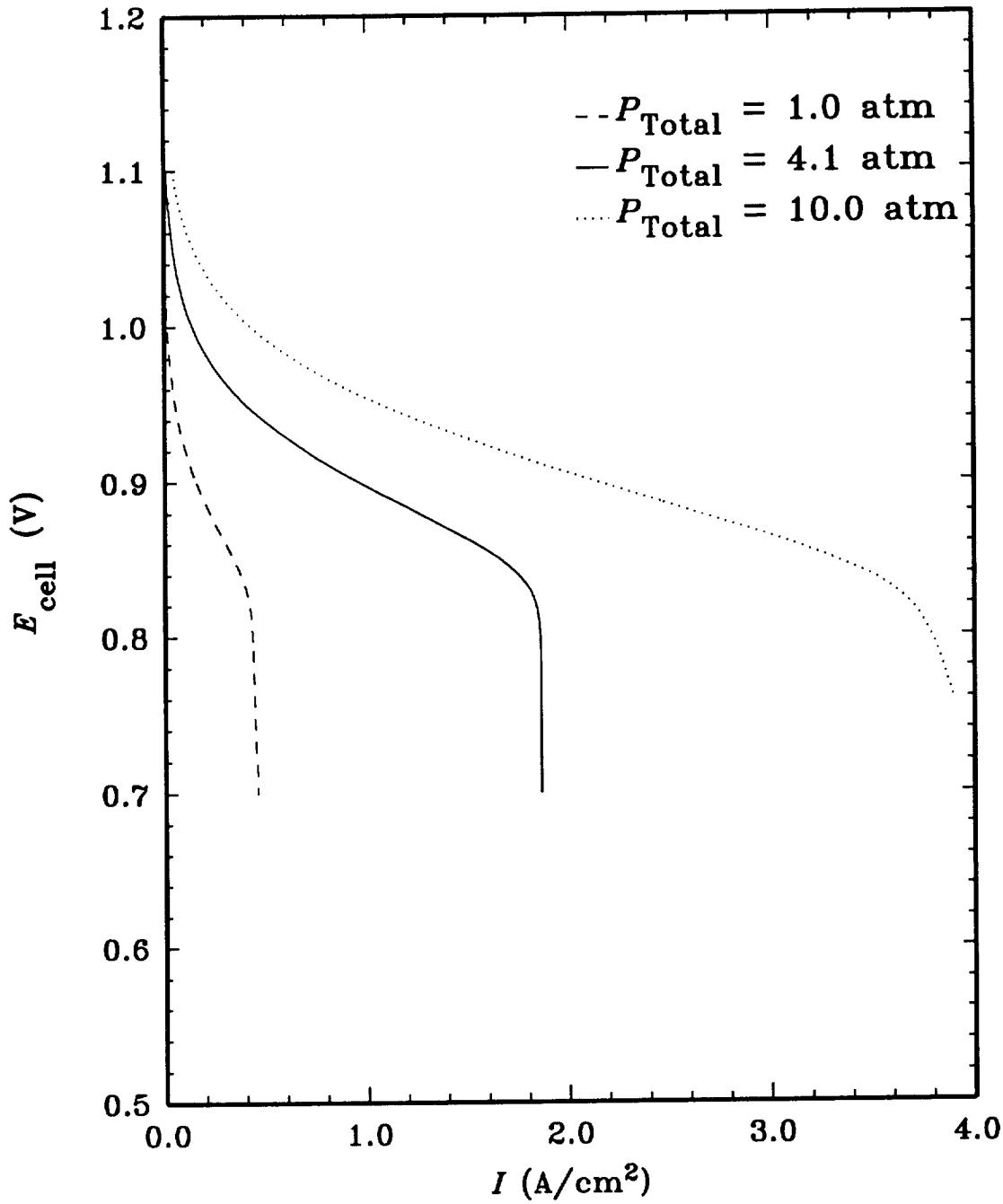

Figure 21. Pressure effects on the alkaline fuel cell polarization evaluated under the base case conditions.

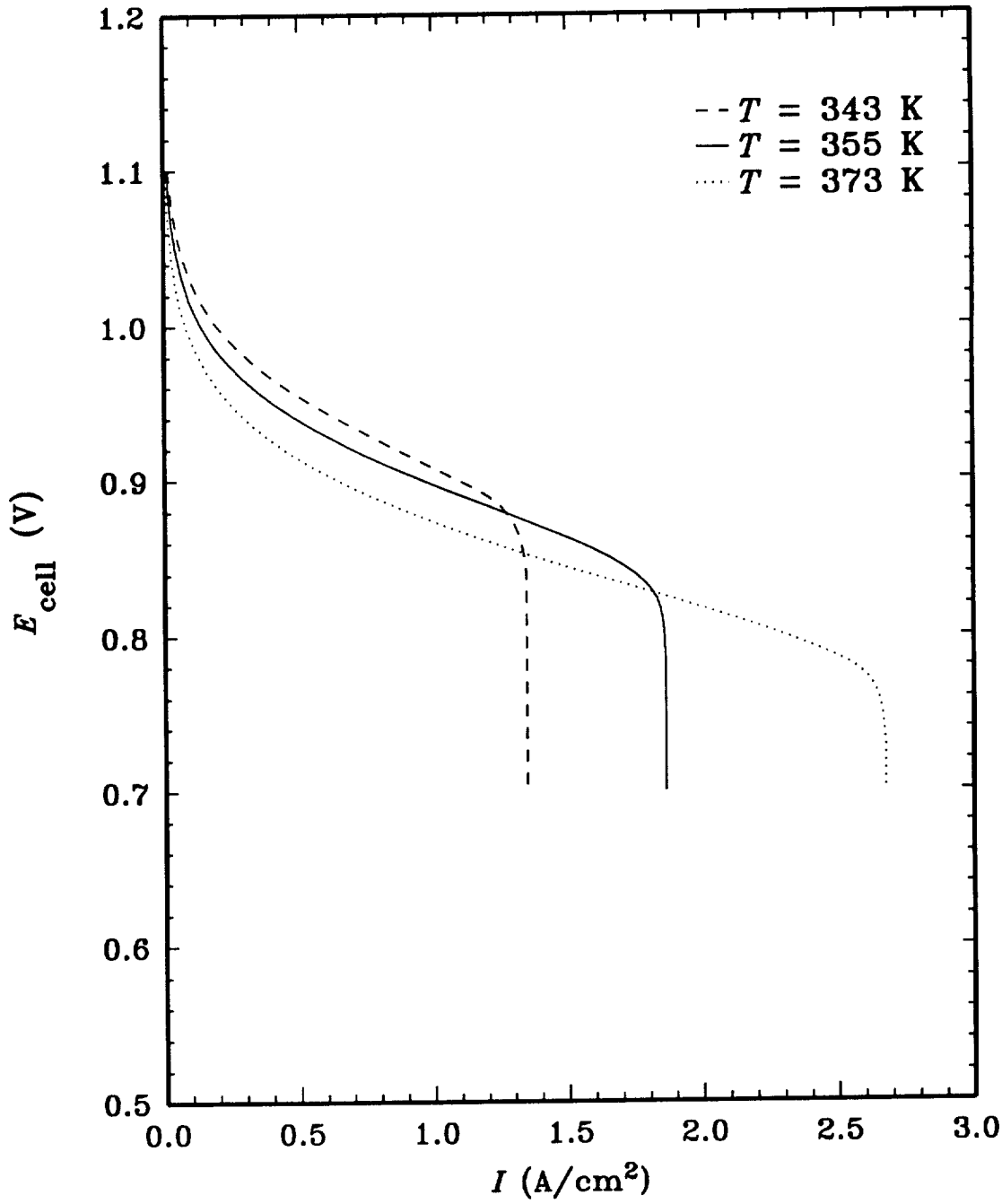

Figure 22. Temperature effects on the alkaline fuel cell polarization evaluated under the base case conditions.

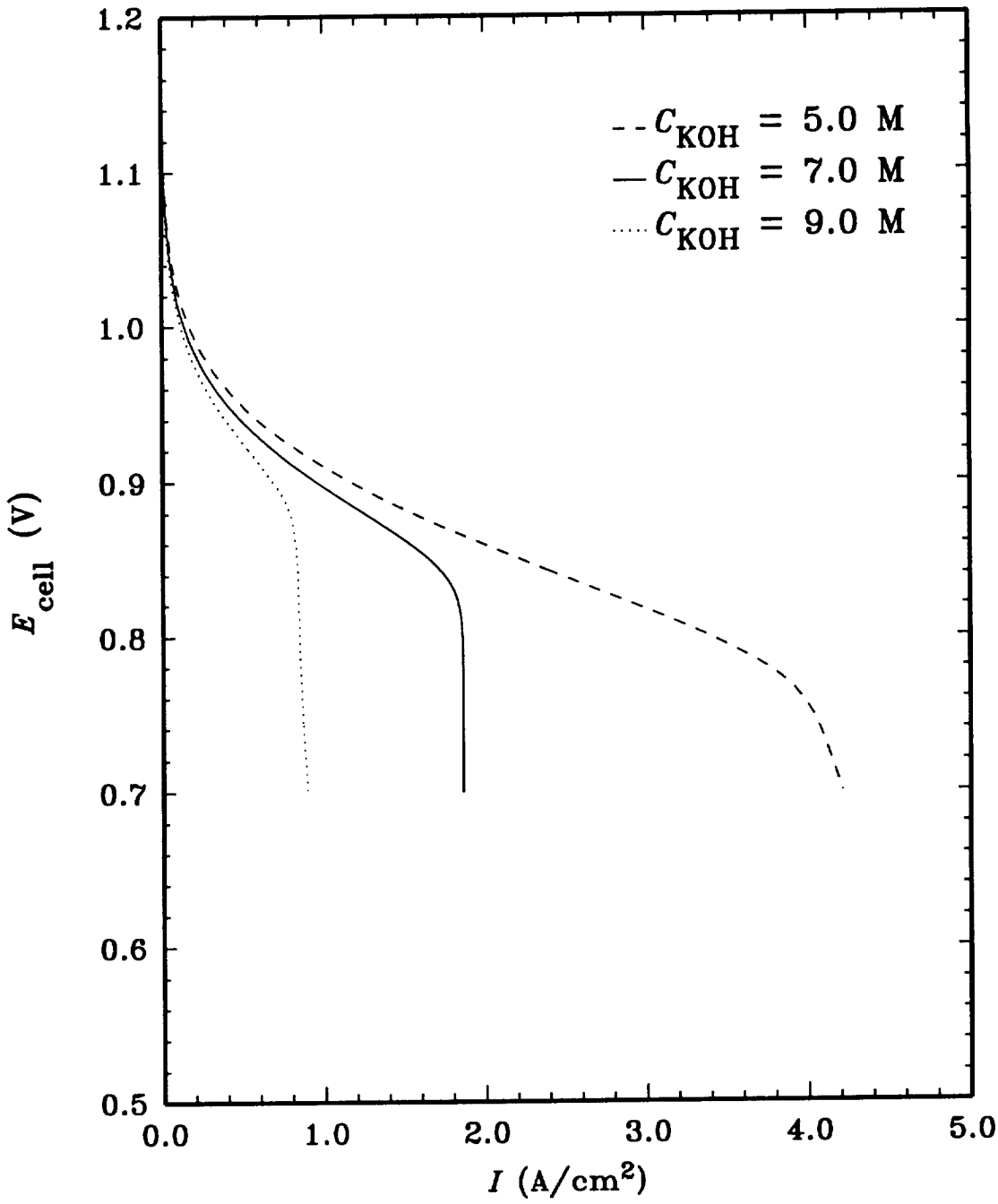

Figure 23. Electrolyte concentration effects on the alkaline fuel cell polarization evaluated under the base case conditions.

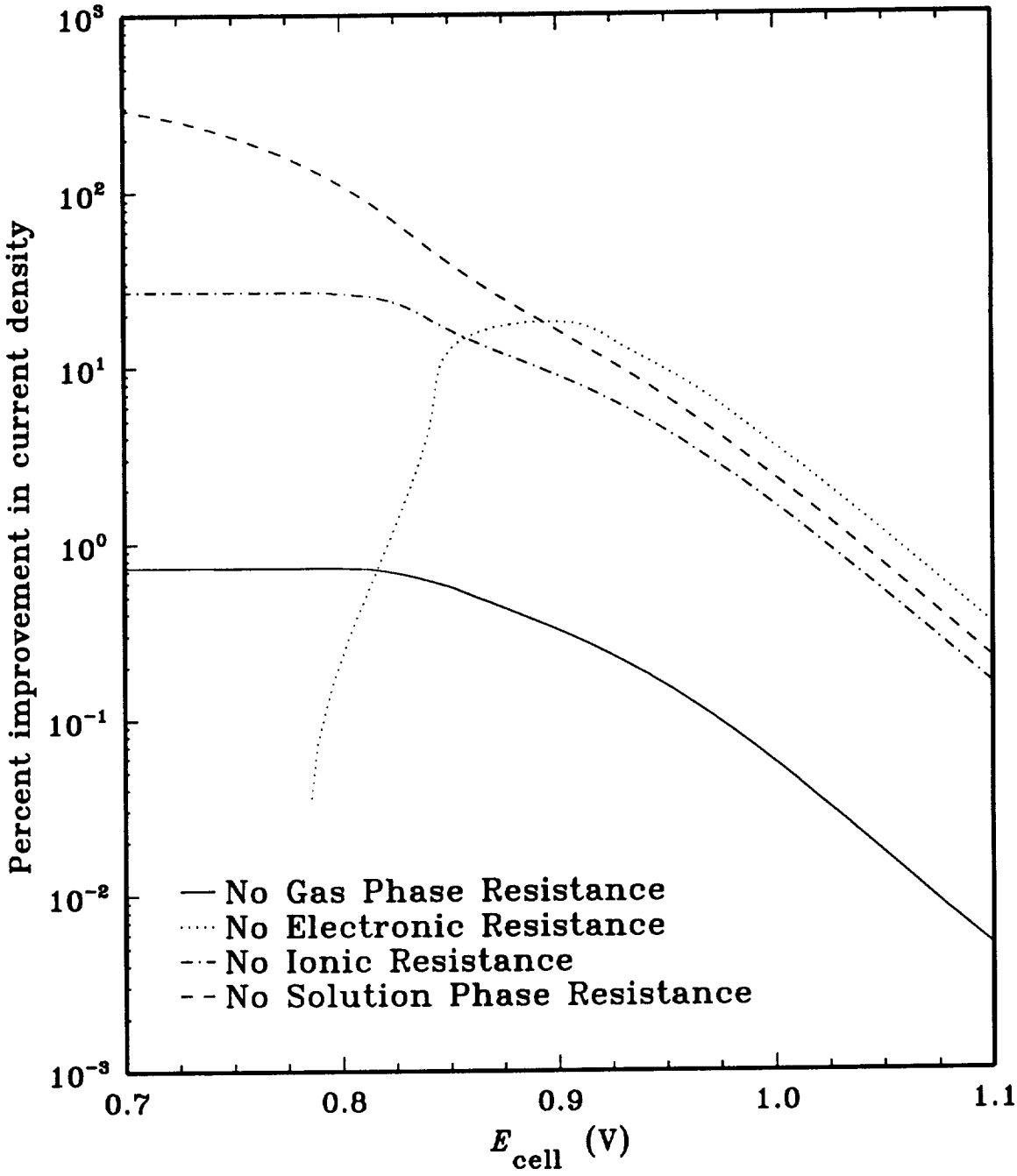

Figure 24. Improvement in the current density with respect to the base case current density ($\frac{i - i_{base}}{i_{base}} \times 100$) when different forms of resistance are neglected.

accomplish this, the various transport parameters were set to large values such that a further increase in the transport parameter would not change the resulting polarization. Thus, to investigate the effects of no gas phase resistances, the gaseous diffusivities were set to large values ($\approx$ 10000) so that no gas phase transport would exist. In an analogous manner, other transport parameters were increased to minimize their respective form of resistance. As shown in Fig. 24, minimizing gas phase diffusional resistances will contribute the least to improving the performance. Ionic resistance effects were minimized by increasing the conductivity of the electrolyte which gave a better performance increase than neglecting gas phase diffusional resistances. The common assumption of no electronic drop is shown in Fig. 24 to give the highest increase in performance for cell potentials greater than 0.9 V. However, for cell potentials lower than 0.9 V, the solution phase resistances have the most influence on the performance. This is reasonable since at potentials that approach the limiting current density, mass transfer effects prevent the attainment of even higher current densities. Increasing the liquid phase diffusion rates and the solubilities of the reactant gases will increase the alkaline fuel cell performance at low cell potentials.

CHAPTER IV

PARAMETER SENSITIVITY AND OPTIMIZATION PREDICTIONS OF THE ALKALINE FUEL CELL

A. Introduction

In designing high performance alkaline fuel cells, there are various attributes that can significantly influence the system. Such attributes might be the gas and liquid phase porosities, reaction layer and separator thicknesses, or the number of gas–liquid sites in the three phase electrodes. One way to investigate the relative importance of these parameters is to use a mathematical model that describes the chemical, electrochemical, and physical processes occurring in the fuel cell. Typically, models of single, three phase electrodes are used in determining polarization losses and optimal design parameters (28,64). However, these models do not consider any interactions between the anode, cathode, and separator which can significantly alter the performance of the system as well as alter the optimal values for certain parameters. A sensitivity analysis is performed on various parameters to determine which parameters are the most influential in increasing or decreasing the current density. This information can indicate the direction one should take in order to design better fuel cells. The results of the sensitivity analysis can also suggest which parameters should be obtained with more accuracy through further modeling studies or through experimentation.

To achieve high performance in the alkaline fuel cell, various design parameters can be optimized so that the fuel cell will deliver the maximum attainable power density. The important design parameters in the alkaline fuel cell are the thicknesses of the anode and cathode diffusion and reaction layers (L_D, L_R), separator thickness (L_S), electrode conductivity (σ), gas and liquid phase porosities (ϵ^g, ϵ^l), and the gas and liquid phase specific surface areas (a^g, a^l). By using the detailed model of the

alkaline fuel cell, these parameters are investigated in order to determine if an optimal value exists for each parameter. The sensitivity of the model predictions to various parameters will be examined next followed by the determination of the optimal design parameters to maximize the alkaline fuel cell's power density.

B. Sensitivity Analysis

In order to determine the relative importance of the transport, kinetic, and structural parameters on the fuel cell's performance, a sensitivity analysis can be applied. The sensitivity analysis can indicate which parameters have the largest influence on the predicted current density and, also, over which range of cell potentials the parameters have the most influence. Additionally, the sensitivity analysis can indicate which parameters are capable of being estimated when the model is used in conjunction with experimental data and a parameter estimation technique. That is, if a small perturbation in a parameter does not significantly change the predicted current density, then that parameter could assume a large range of values, all of which will give the same performance. The sensitivity coefficient can be defined as the difference in the predicted current density to a base–case current density for a small, dimensionless perturbation in a parameter j, while holding all other parameters constant:

$$\frac{\partial I}{\partial \ln \theta_j} = \frac{I - I^*}{\frac{\theta_j - \theta_j^*}{\theta_j^*}} \quad (\mathrm{A/cm^2}) \qquad [156]$$

where θ_j^* and I^* are the base-case parameter value and current density, respectively. Hence, large sensitivity coefficients indicate the parameter of interest significantly influences the current density. Large sensitivity coefficients may also indicate which parameters should be obtained with more accuracy through further modeling or experimental studies. That is, if the value for a parameter is not accurately known

and the parameter has a large sensitivity coefficient, then that parameter value should be ascertained with more accuracy to gain confidence in the model predictions.

All sensitivity coefficients calculated for this work were accomplished by increasing the parameter of interest by 5% over the base case values (shown in Tables XII – XV) and calculating the resulting change in the current density as given by Eq. [156]. This was performed over the potential ranges of (0.8 – 0.85 V), (0.85 – 0.93 V), and (0.93 – 1.1 V) representative of the concentration, ohmic, and activation polarization regions, respectively, for the conditions of the fuel cell simulation. By calculating the sensitivity coefficients in this manner, the effects of the parameters on the current density can be investigated under conditions of the various forms of polarization.

Sensitivity of Transport and Electrokinetic Parameters

The sensitivity coefficients for various parameters are shown in Figs. 25 and 26 for parameters specific to the cathode and anode, respectively. As shown in the activation and ohmic regions, the model predictions are most sensitive to the transfer coefficients, liquid phase specific surface area, and the reactant gas reaction orders. Since the model predictions are extremely sensitive to the transfer coefficients as governed by the exponential terms in the Butler-Volmer expression, Eq. [11], small perturbations in the transfer coefficients can significantly affect the predicted current density. Unfortunately, obtaining accurate values for the transfer coefficients is difficult since they vary too much depending on the temperature, cell potential, electrocatalyst, and electrode structure. Parameter estimation techniques could be used to fit the model to reliable experimental data by predicting the values for the transfer coefficients. This may necessitate a reformulation of the Butler-Volmer expression as shown by (65) to avoid numerical difficulties in the parameter estimation method.

The model predictions show little sensitivity to small perturbations in the conductivities of the cathode and anode diffusion regions as shown in Figs. 25 and 26, respectively. The dependence of the model predictions on the conductivities in the

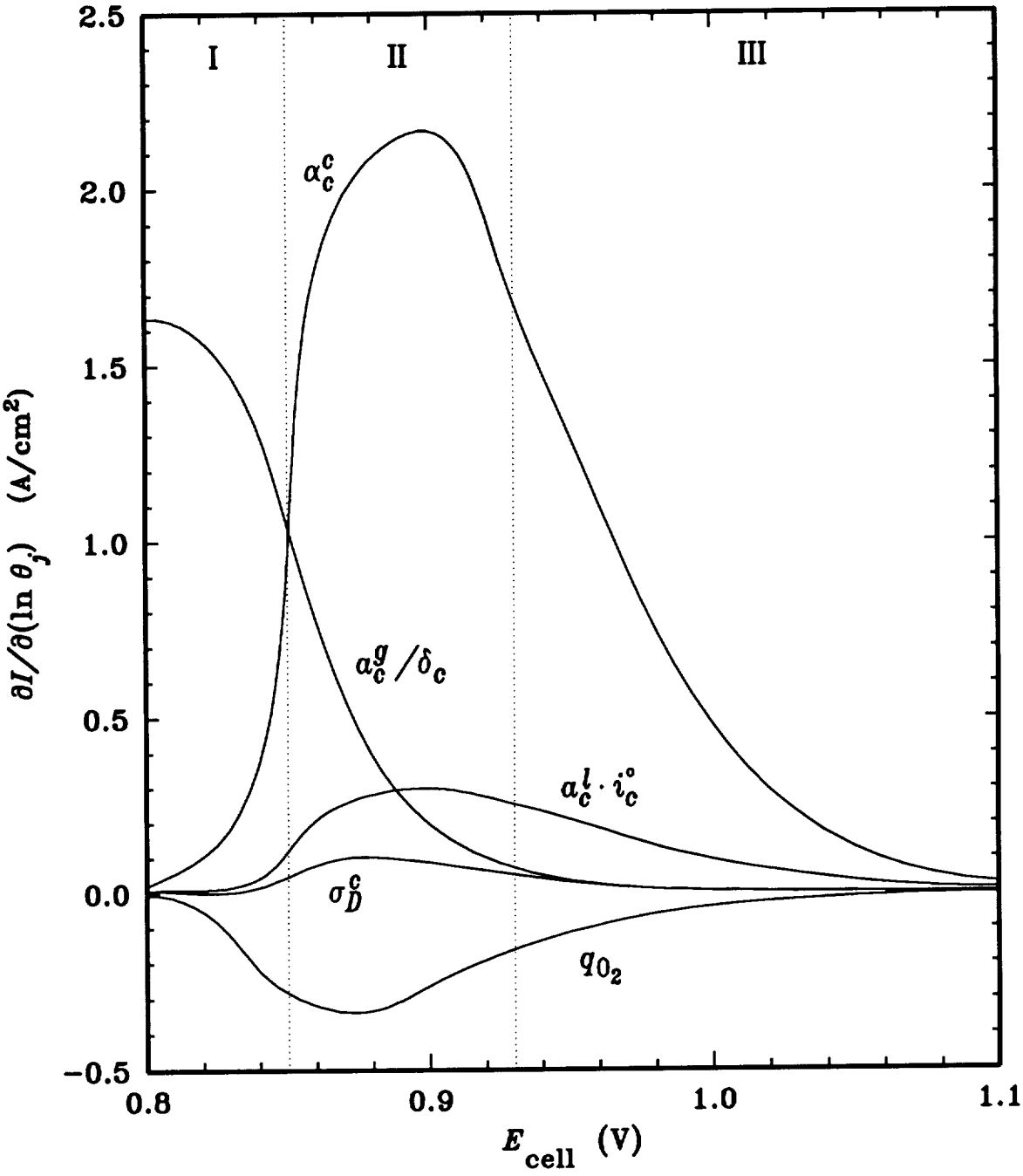

Figure 25. Sensitivity of the model predictions to cathode parameters for the concentration (I), ohmic (II), and activation (III) polarization regions.

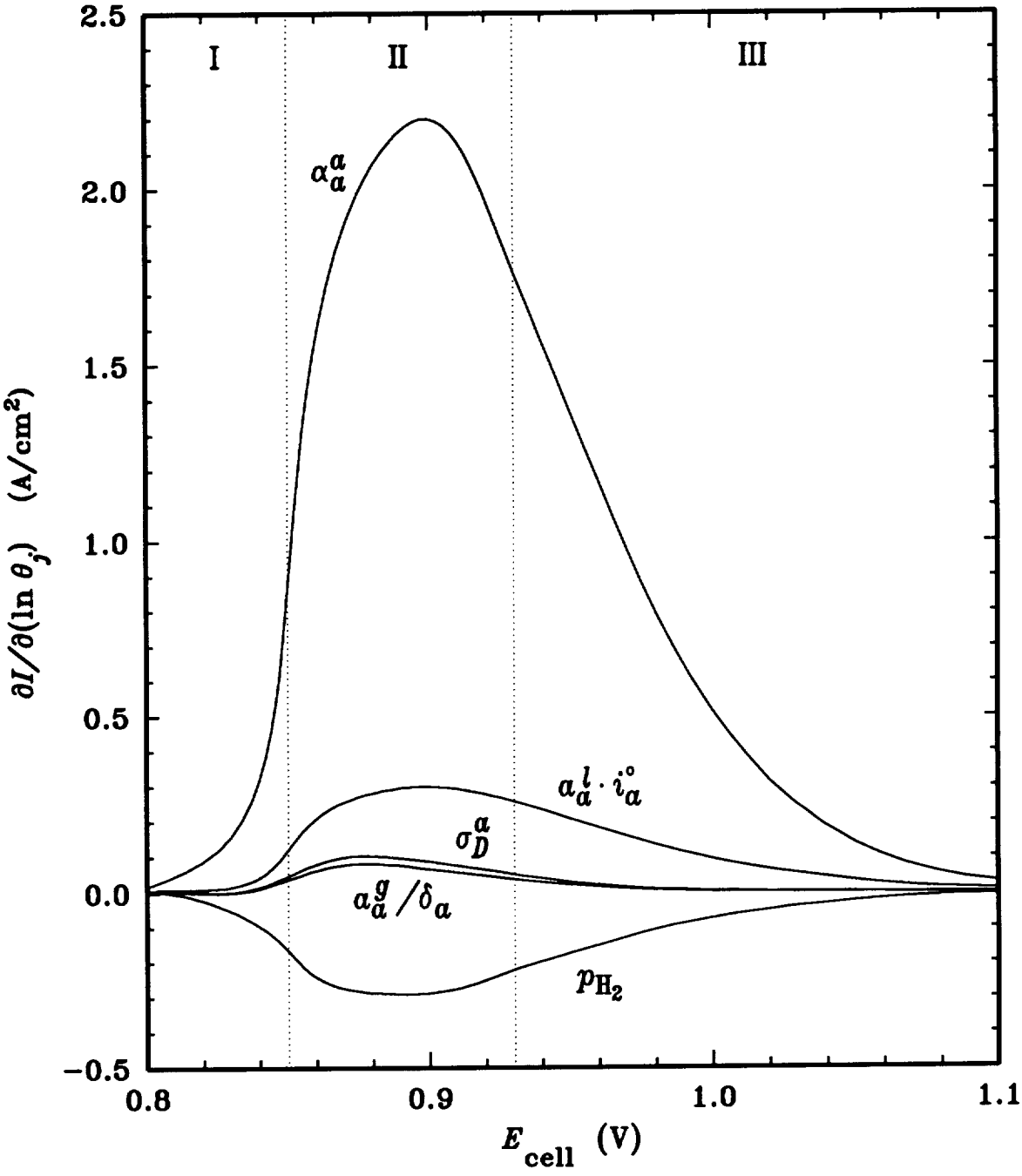

Figure 26. Sensitivity of the model predictions to anode parameters for the concentration (I), ohmic (II), and activation (III) polarization regions.

reaction layers was even less pronounced than in the diffusion layers. The relative insensitivity of a_a^g/δ_a on the model predictions over the entire range of cell potentials indicate that the dissolution of hydrogen gas into the electrolyte is not rate limiting. The most influential parameter in the concentration polarization region is a_c^g/δ_c which governs how much oxygen gas dissolves into the electrolyte through Eq. [13].

Sensitivity of Thickness Parameters

The effects of fuel cell thickness on the predicted performance are shown in Fig. 27 where the cathode reaction layer thickness is the most sensitive to the model predictions, followed by the anode reaction layer and separator thickness. The anode and cathode gas diffusion layer thicknesses are shown to have little effect on the model predictions. It is also apparent in Fig. 27 that the limiting current density can be increased by increasing the cathode reaction layer thickness or by decreasing the separator thickness. However, as will be shown later, increasing the cathode reaction layer thickness too much can degrade the performance.

Sensitivity of Porosity Parameters

The effects of porosity on the model predictions are shown in Fig. 28 where $\epsilon_{R,c}^l$ has the largest influence on the model predictions followed by $\epsilon_{R,c}^g$, ϵ_S, and $\epsilon_{R,a}^l$. Increasing the gas phase porosities in the diffusion layers and in the anode reaction layer showed no change in the model predictions. Since the diffusivities are influenced by the porosities as indicated by Eq. [7], Fig. 28 suggests that diffusion is not as important at high cell potentials as at low cell potentials. This is verified by Fig. 29 showing that the diffusion coefficients have the most influence on the cell performance in the ohmic and concentration polarization regions.

C. Current Density Optimization

Thickness Effects

The previous analysis on the sensitivity coefficients showed that small perturba-

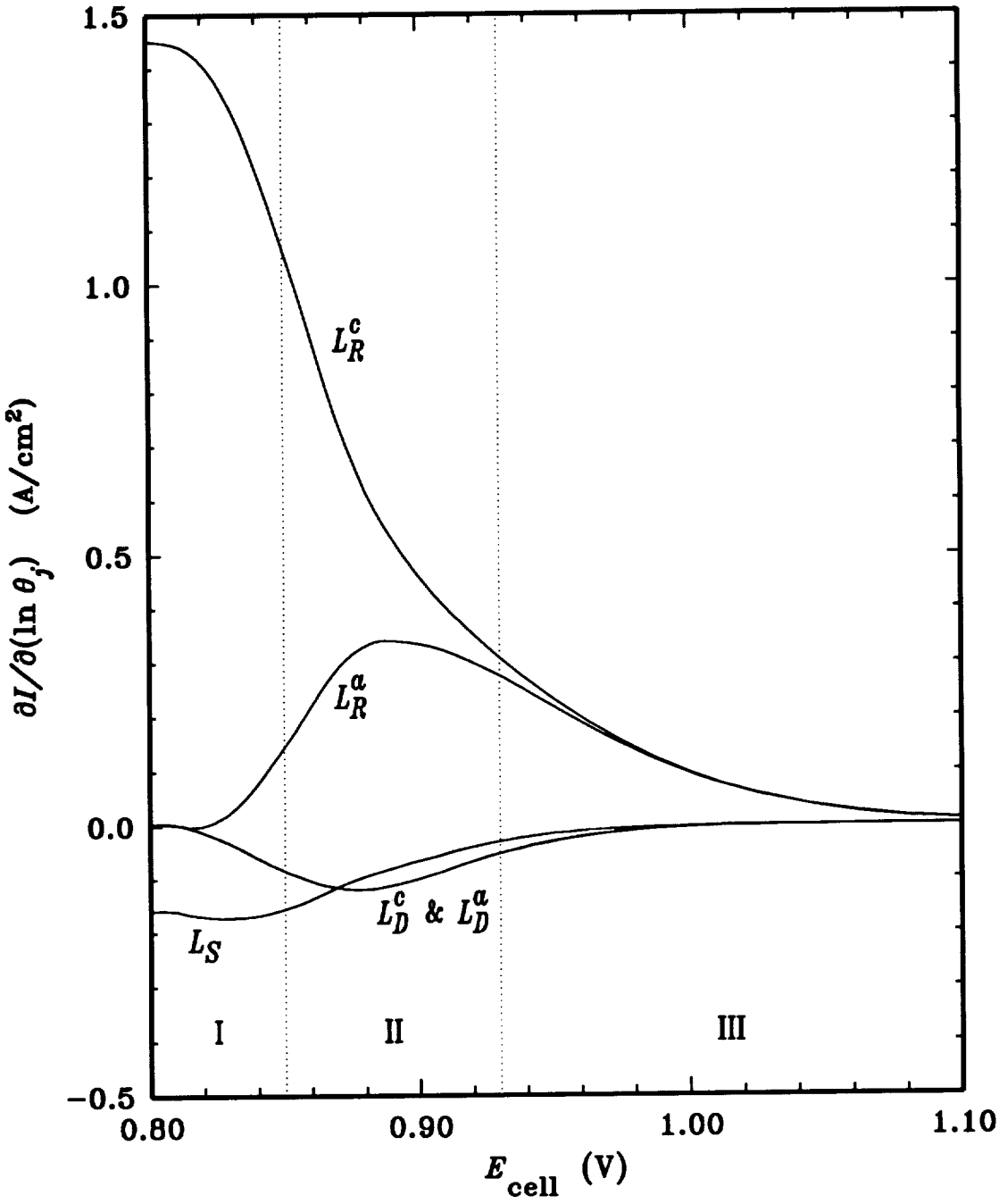

Figure 27. Sensitivity of the model predictions to changes in fuel cell thickness for the concentration (I), ohmic (II), and activation (III) polarization regions.

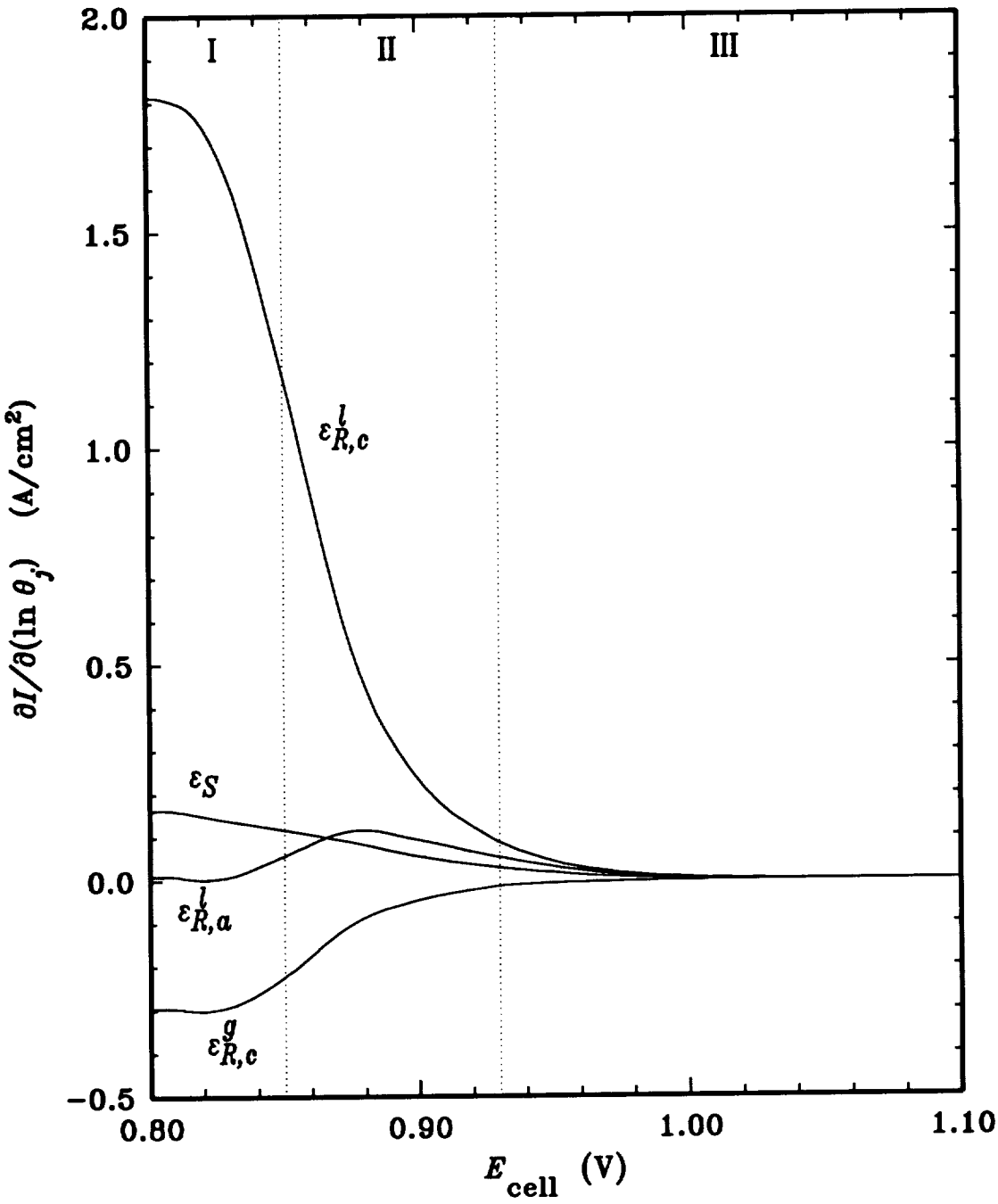

Figure 28. Sensitivity of the model predictions to changes in porosity for the concentration (I), ohmic (II), and activation (III) polarization regions.

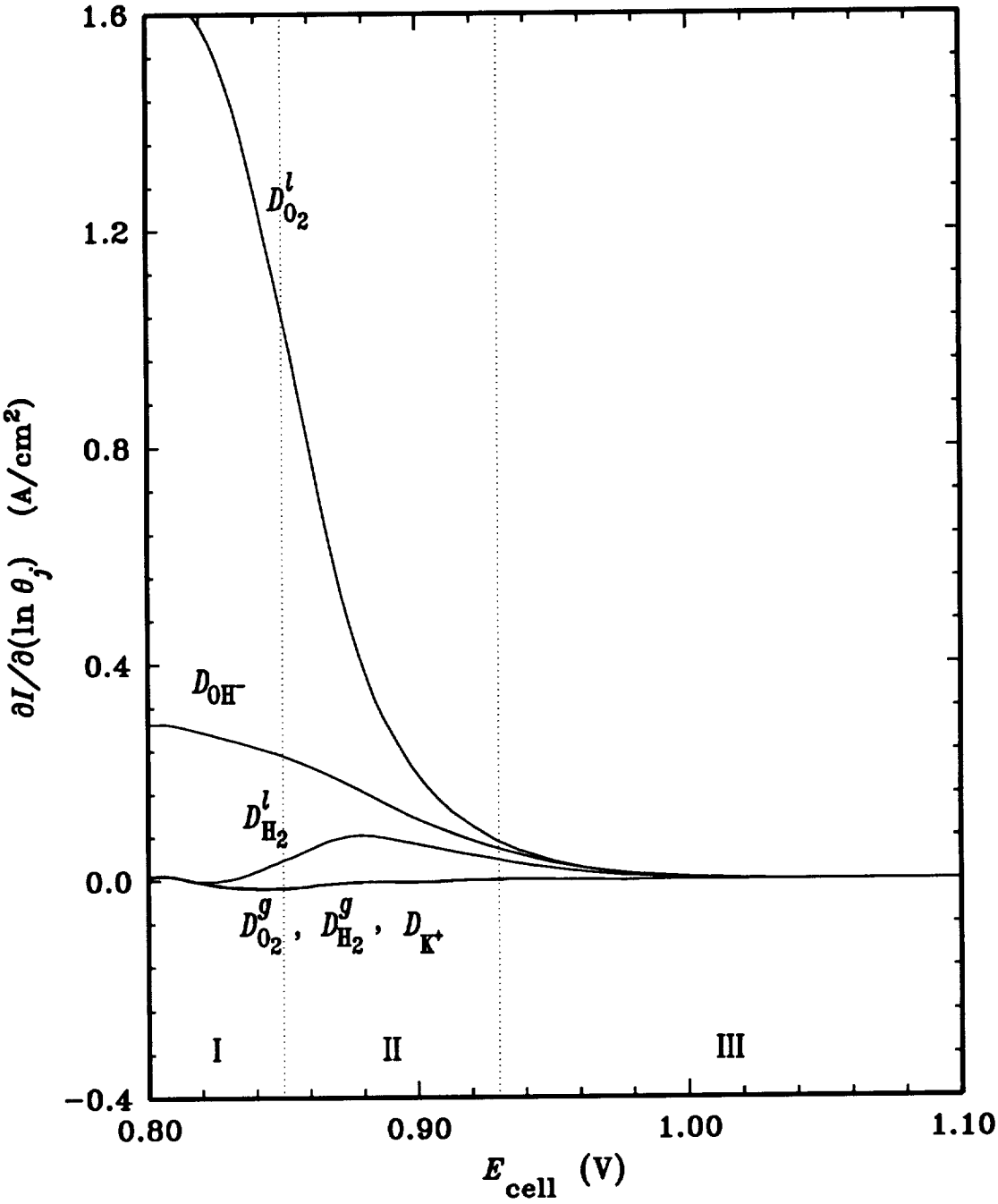

Figure 29. Sensitivity of the model predictions to changes in diffusivity for the concentration (I), ohmic (II), and activation (III) polarization regions.

tions in design parameters could yield significant improvements in the current density. However, the sensitivity analysis does not allow a quantitative prediction on what values the design parameters should have in order to provide the best performance. By using the mathematical model of the alkaline fuel cell, various design parameters can be optimized so that the system achieves the maximum attainable power density. From Fig. 27, it can be seen that the anode and cathode reaction layer thicknesses and the separator thickness have the most effect on the performance. Calculating the limiting current density for these parameters as they are varied individually over a 20 to 300 micron range with the others set equal to their base case values (Tables XII – XV) gives the results shown in Fig. 30. As shown in Fig. 30, a maximum occurs in the limiting current density for L_R^a at about 40 μm and for L_R^c at about 225 μm. The separator thickness does not show a maximum in the limiting current density indicating that its thickness should be as small as possible. Kenjo and Kawatsu (39) measured a flat limiting current density of about 1.5 A/cm^2 corresponding to a reaction layer thickness of 100 to 270 μm for an oxygen electrode. Although different operating conditions were used, the location of the optimal thickness range in Fig. 30 for L_R^c is similar to that obtained by (39). It has commonly been thought that increasing the reaction layer thickness should increase the limiting current density since more reaction sites are present in the electrode. However, according to our model, the reason for the decrease in the limiting current density beyond an optimal thickness is due to a lowering of the gas solubility, not to gas phase diffusional resistances. Increasing the reaction layer thickness causes a higher electrolyte concentration in the cathode which lowers the solubility of the reactant gas into the electrolyte. This will diminish the liquid phase diffusion of the dissolved reactant gas leading to lower fuel cell performance.

Porosity Effects

The sensitivity analysis for the porosity parameters, Fig. 28, show that the

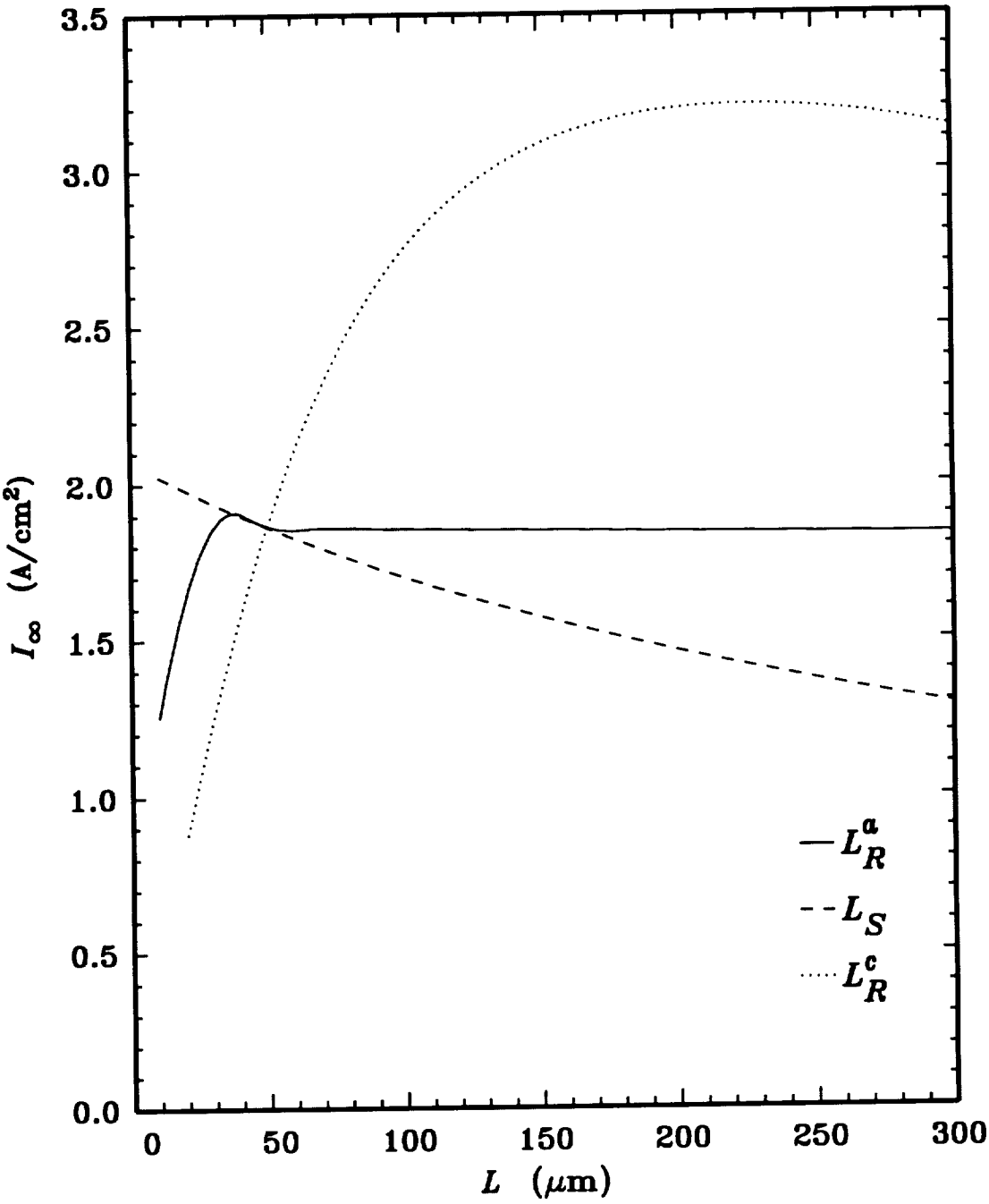

Figure 30. Effects of the separator and reaction layer thicknesses on the limiting current density.

concentration and ohmic polarization regions are significantly influenced by the various porosities. To investigate the optimal values for these porosities, the limiting current density was calculated for different parameter settings for the liquid phase porosities. These results are shown in Fig. 31. Note that the anode and cathode reaction layers were assumed to have a total porosity of 0.7 causing a constraint for the gas and liquid phase porosities

$$0.7 = \epsilon_R^g + \epsilon_R^l \qquad [157]$$

As shown in Fig. 31, increasing $\epsilon_{R,a}^l$ does not cause any noticeable difference in the predicted limiting current density. However, in the cathode, a dramatic increase in the limiting current density occurs up to an optimal porosity of about 0.695 where upon further increasing the porosity a rapid decline in the limiting current density occurs. Since the model treats the gas phase transport as occurring by molecular diffusion and convection, only a small fraction of the total electrode porosity is needed for the gas phase. As the gas phase porosity approaches a small value (*e.g.*, 0.005), the effective gas phase diffusivity becomes even smaller through Eq. [7] resulting in mass transfer limitations for the gas phase transport. Increasing the separator porosity increases the limiting current density more rapidly at lower porosities than at higher porosities. Since the separator porosity was assumed to be 0.8, further increasing the porosity will result in a slight increase of 30 mA/cm^2 at the limiting current density. Unfortunately, a maximum does not occur in the limiting current density for the separator porosity preventing an optimal porosity from being recognized. Note that other criteria could be considered in determining an optimal separator porosity in addition to an extremum in the current density such as the mechanical strength of the separator or lifetime, but this is beyond the scope of this work.

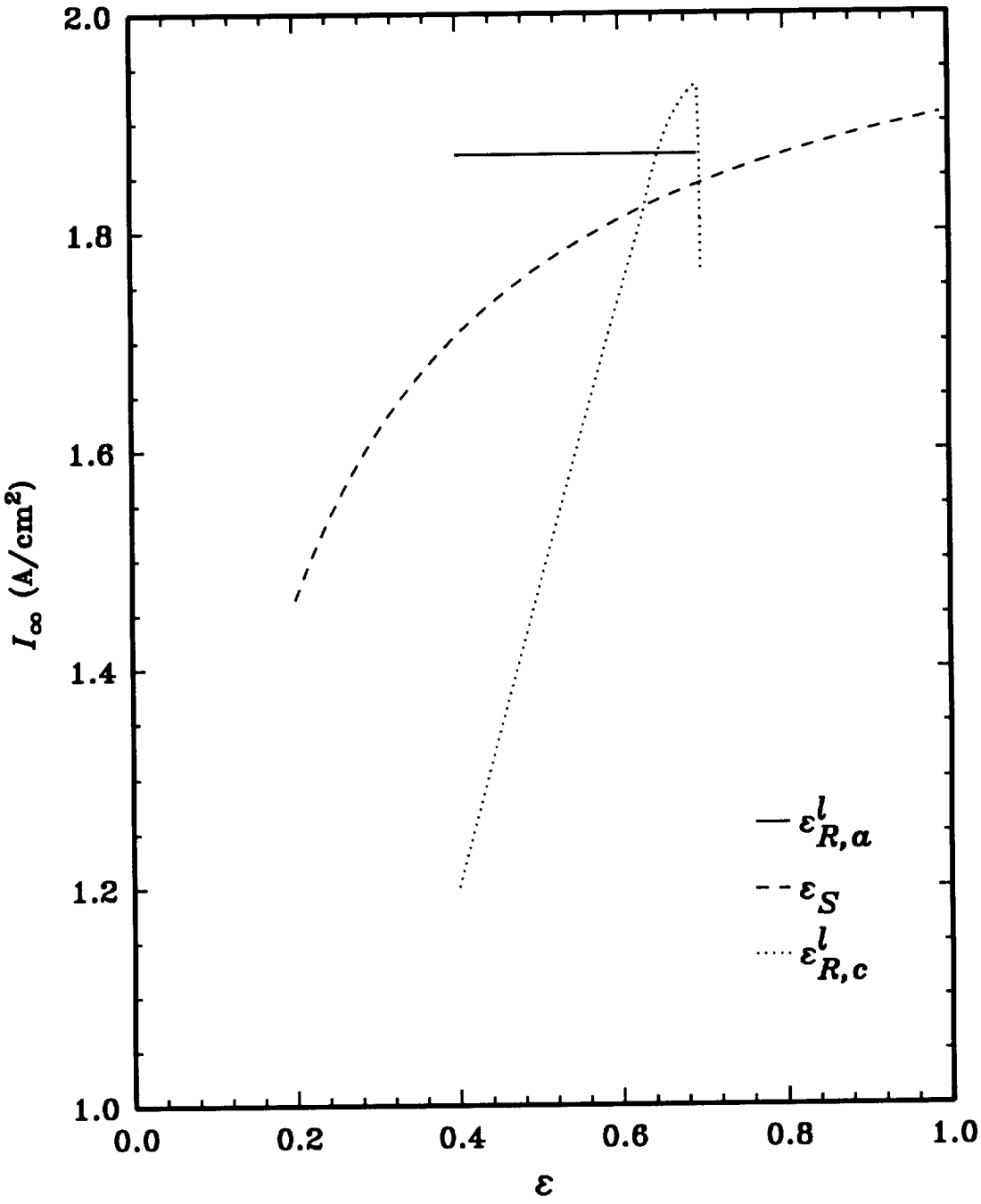

Figure 31. Effects of liquid phase porosity on the limiting current density.

Specific Surface Area Effects

The effects of the three specific surface areas (a_a^g, a_c^g, a_c^l) on the limiting current density are shown in Fig. 32. The performance curve for a_a^l is similar to that obtained for a_c^l and, thus, is not shown in Fig. 32. Note that since the diffusion layer thickness, δ, and the exchange current density, i°, always appear with either a gas or liquid phase specific surface area, δ was arbitrarily set to 1.0 x 10^{-5} cm and i° to 1.0 x 10^{-5} A/cm^2. It should also be noted that a_a^l and a_c^l do not affect the limiting current density as shown in Fig. 17, but they do affect the polarization prior to reaching the limiting current density. Thus, to properly investigate the effects of these parameters, the current density at 0.9 V was predicted for a_c^l ranging from 500 to 50,000 cm^2/cm^3 as shown in Fig. 32. The predicted current density approaches a fairly constant value as a_c^l is increased, suggesting that further increases in a_c^l will only contribute a marginal improvement to the current density or that a limiting current density has been attained. In Fig. 32, it is shown that increasing the anode gas phase specific surface area beyond 2000 cm^2/cm^3 does not improve the current density at all. Although increasing this parameter increases the dissolution rate of hydrogen gas into the electrolyte as governed by Eq. [13], the dissolution rate for oxygen is still limiting the current density. This is verified by Fig. 32 for a_c^g where increasing this parameter causes an increase in the current density. The large increase in performance due to increasing a_c^g shows the importance of designing three-phase electrodes with large interfacial gas-liquid surface areas, especially for the oxygen electrode. Since the dissolution rate is dependent on the gas phase specific surface area, an increase in a_c^g will allow more gas to dissolve into the electrolyte to react.

Optimal Power Density

To achieve optimal performance in the fuel cell, the more influential parameters of the model can be used to maximize the predicted current density or power density. It should be noted that other criteria than a maximum current density could be used

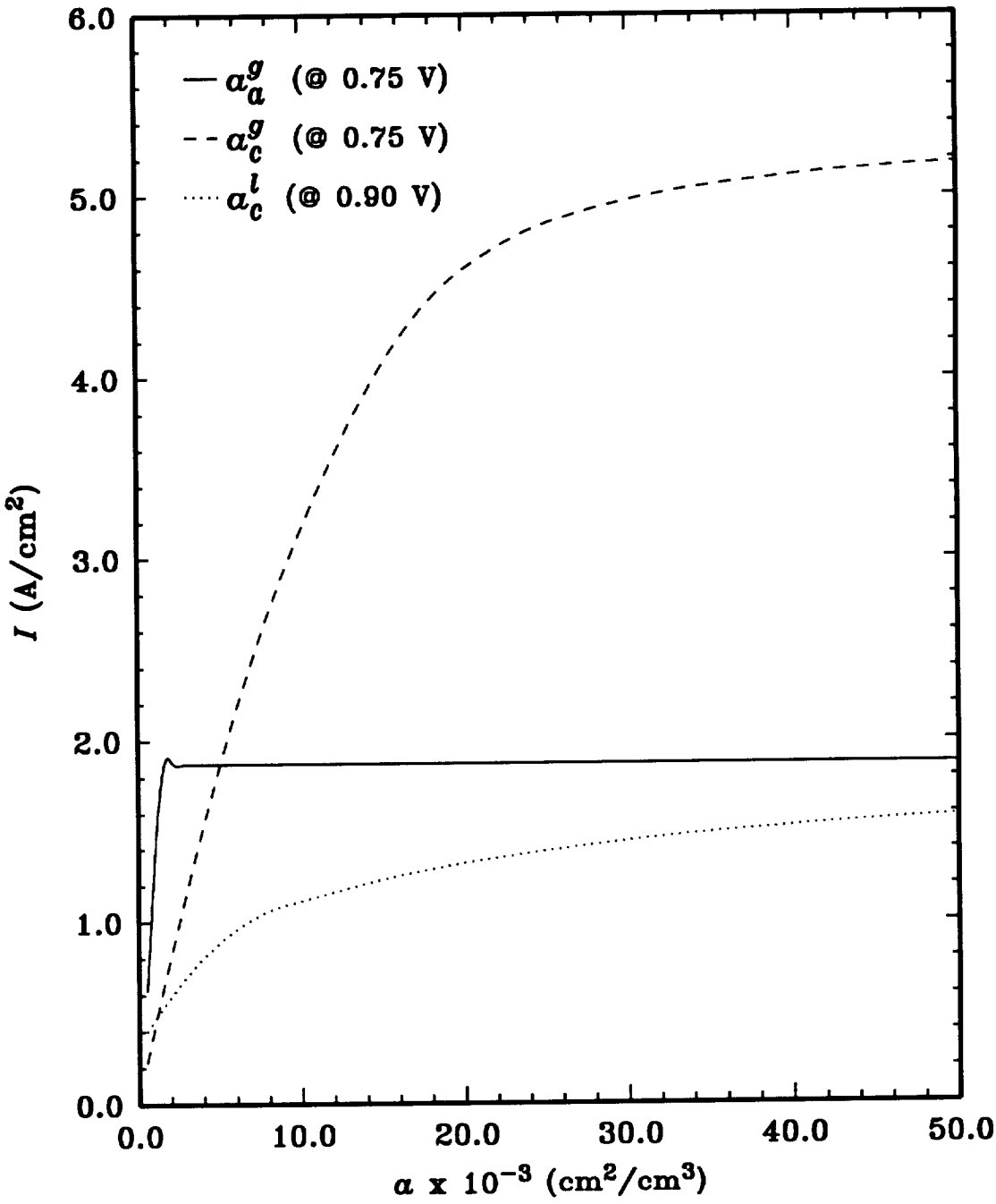

Figure 32. Effects of the gas and liquid phase specific surface areas on the current density.

in formulating an objective function. For example, Newman (66) optimizes an acid fuel cell by considering the average current density and the utilization of hydrogen based on capital, power, and fuel costs. Since the main objectives of this work are to increase the maximum attainable power density, economic factors are not considered. To maximize the power density, an objective function can be defined as:

$$\max\ P\left(\vec{\theta}\right) = E_{\text{cell}} \cdot I\left(\vec{\theta}, E_{\text{cell}}\right) \qquad [158]$$

where $\vec{\theta}$ represents a vector of unknown parameters θ_j and E_{cell} is itself an unknown cell potential. The optimal parameters and cell potential can be selected such that the power density as given by Eq. [158] is at a maximum.

The results of the sensitivity analysis shown in Figs. 25 – 28 and the single parameter optimal studies shown in Figs. 30 – 32 indicate which parameters can be optimized in Eq. [158]. The anode and cathode reaction layer thicknesses and the liquid phase porosity in the cathode reaction layer are the only parameters that caused an extremum in the predicted current density. All other parameters investigated here monotonically increased the current density as the parameters where lowered (*e.g.*, L_S) or increased (*e.g.*, a^g, a^l, ϵ_S). Note that the transfer coefficients could be included in the optimization procedure since they have a strong effect on the current density as shown in Figs. 25 and 26. Additionally, the reactant gas reaction orders, q_{O_2} and p_{H_2} could also be included in the optimization procedure. However, since it may be more difficult to manufacture electrodes with certain values for the transfer coefficients and reaction orders than for the thicknesses or porosities, the transfer coefficients and reaction orders were not considered in the optimization procedure.

The IMSL routine UMINF (67) was used to minimize Eq. [158] by using a quasi-Newton method to determine L_R^a, L_R^c, $\epsilon_{R,c}^l$, and E_{cell}. The optimized values are shown in Table XVI along with their starting values. The optimal cathode reaction layer thickness in Table XVI corresponds to about the same optimal value as shown

in Fig. 30, whereas a large difference results for the optimal anode reaction layer thickness. Since increasing L_R^a above 55 μm did not improve the current density as shown in Fig. 30, L_R^a was scaled over a thickness range of 50 to 300 μm using the optimal values in Table XVI for L_R^c, $\epsilon_{R,c}^l$, E_{cell} to investigate whether L_R^a is indeed at an optimal value. The resulting performance curve verified that the optimal anode reaction layer thickness shown in Table XVI does cause an extremum in the power density. Using the optimal parameter values other than E_{cell}, the performance of the fuel cell was predicted by the model as shown in Fig. 33 in comparison to the base case performance. As can be seen, a significant improvement in the maximum attainable power density has been achieved just by optimizing the cell potential and three design parameters.

Table XVI. Optimal parameter values for maximizing the power density.

Starting Values	Optimized Values
L_R^a = 0.005 cm	L_R^a = 0.01627 cm
L_R^c = 0.005 cm	L_R^c = 0.02234 cm
$\epsilon_{R,c}^l$ = 0.65	$\epsilon_{R,c}^l$ = 0.674
E_{cell} = 0.75 V	E_{cell} = 0.803 V

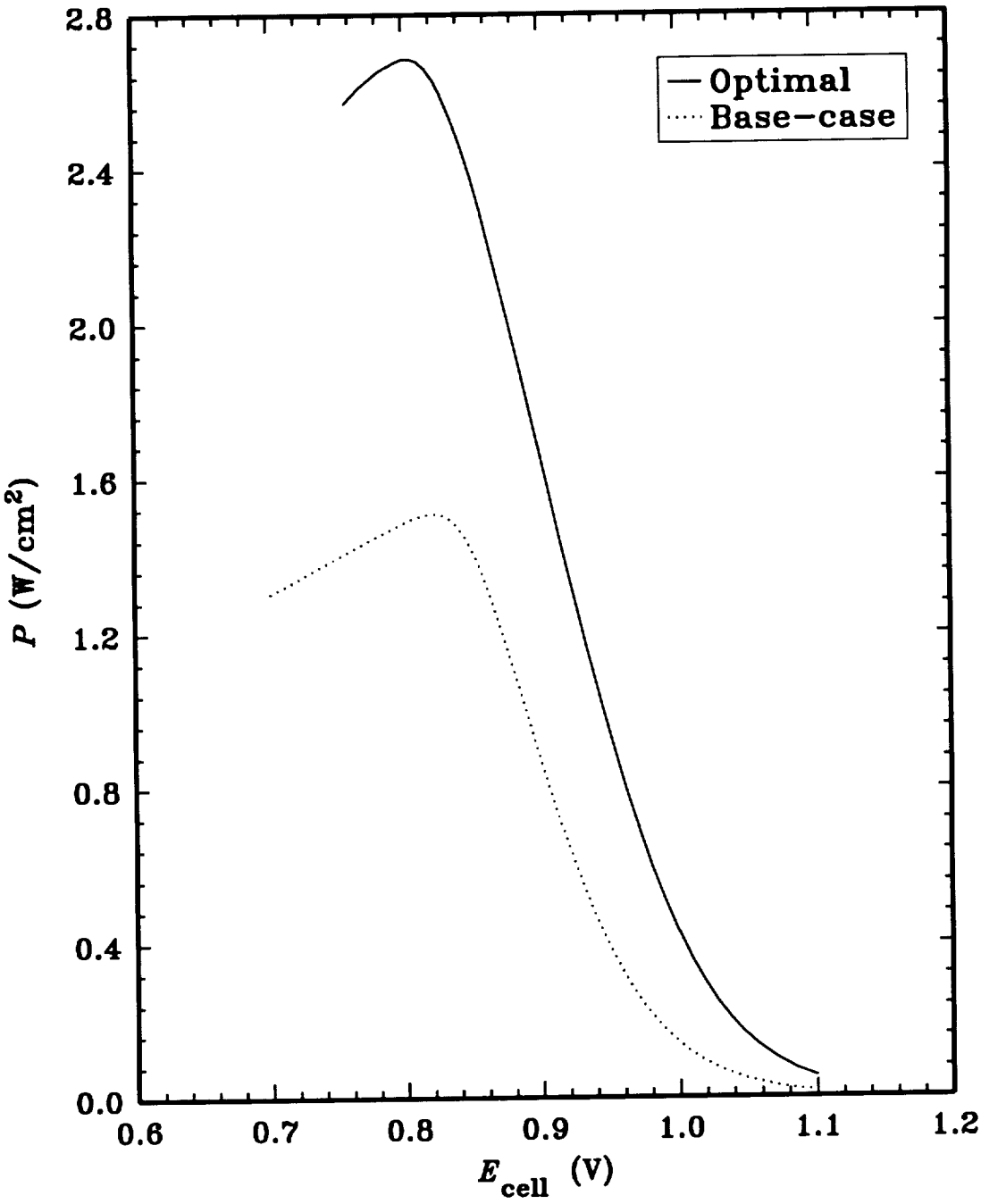

Figure 33. Optimal and base case power density performance for the alkaline fuel cell.

CHAPTER V

CONCLUSIONS AND RECOMMENDATIONS

A. Alkaline Fuel Cell Model Conclusions

A mathematical model of an alkaline fuel cell has been developed to predict the performance of the system for different cell potentials operating under steady-state and isothermal conditions. The model describes the phenomena occurring in the gas, liquid, and solid phases of the anode and cathode gas diffusion regions, the anode and cathode reaction layers, and the separator. The model accounts for the one-dimensional transport of reactant gases, water vapor, solution phase concentrations, solid and solution potential variations, and the volume average velocity. Performance results were obtained for a set of base-case conditions that could be used for a high performance alkaline fuel cell. Gas phase diffusional resistances were found not to significantly influence the performance of the system. The model predicts that the diffusion of dissolved oxygen contributes the most to the polarization losses at low potentials while the electronic resistances contribute the most resistance at high cell potentials. To obtain better performance with the alkaline fuel cell, it is suggested that the three-phase electrodes should be highly conductive and contain a large number of gas-liquid sites allowing more reactant gas to dissolve into the electrolyte. Increasing the pressure and temperature will also result in improved performance.

Various attributes of the system such as the catalyst distribution, exchange transfer currents, and diffusional film areas could be optimized to yield better performance. The model shows that interactions between the anode and cathode exist suggesting that models or experiments based on full–cells are necessary instead of half–cells when estimating unknown parameters or optimizing various attributes. One of the main advantages of this model is its ability to quantitatively show the influence of different parameters on the predicted current density. These quantitative results can

help in the design of alkaline fuel cells as well as help focus the direction of future research on alkaline fuel cells.

A sensitivity analysis of an alkaline fuel cell model indicates that many parameters can significantly influence the performance of the system, especially in the ohmic and concentration polarization regions. In particular, parameters specific to the oxygen electrode such as the reaction layer thickness, liquid phase porosity, gas phase specific surface area, and the cathodic transfer coefficient have been found to influence significantly the performance. The effect of various design parameters on the limiting current density have been investigated to determine if optimal values exist for the parameters. The model has shown that the anode and cathode reaction layer thicknesses, the liquid phase porosity in the cathode reaction region, and the cell potential can be optimized to give the maximum attainable power density. The optimal reaction layer thicknesses are shown to be a compromise between the number of reaction sites and the solubility of the reactant gases. A small fraction of the total porosity in the cathode reaction region is needed in the gas phase to sustain a high gas phase diffusion rate while maintaining a large diffusion rate in the liquid phase. The model predictions indicate that the largest improvement in the fuel cell performance will be recognized by increasing the gas phase specific surface area in the cathode followed by increasing the electrocatalytic activity or liquid phase specific surface area and decreasing the separator thickness from the base case conditions.

B. Recommendations for Further Studies

Future studies on the alkaline fuel cell should include a closer comparison of the model and experimental data. Incorporating more features (*e.g.*, teflon content, catalyst distribution, pore sizes, etc.) of experimental three phase electrodes into the model may give a better description of the fuel cell performance. It may also be desirable to include air as the reactant gas in the oxygen electrode rather than oxygen itself since some applications of the alkaline fuel cell use air as the reactant gas. This

would require the addition of another reaction in the system since the CO_2 in the air would react with the OH^- ions causing the $CO_3^=$ to precipitate in the pores and the OH^- concentration to be reduced.

One desired extension to the alkaline fuel cell model would be to include the gas channel effects. As the reactant gases flow through the channels, their pressures decrease while the water vapor pressures increase in the anode and cathode gas channels. If too much water is produced, the electrodes may become flooded causing severe performance degradation. Including the gas flows in the gas channels may help determine when conditions of flooding will occur and suggest methods to minimize the effects of flooding.

Another important effect to consider is the thermal management of the fuel cell. The heat produced by the alkaline fuel cell reactions is typically removed by a circulating electrolyte. However, when a non-circulating electrolyte is used, as in this work, severe thermal gradients may occur in the electrodes and separator which can further degrade the performance of the fuel cell. Including a thermal balance would allow an even more realistic description of the fuel cell.

NOMENCLATURE

Roman Symbols

a^g	Specific gas phase surface area, cm^2/cm^3
a^l	Specific liquid phase surface area, cm^2/cm^3
b	Tafel slope, V/decade
C_i	Concentration of species i, mol/cm^3
D_i	Free-stream diffusivity of species i, cm^2/s
$\mathcal{D}_i$	Effective diffusivity of species i, cm^2/s
E	Electrode potential, V
f_a	Fraction of water generated that leaves through the anode
f_c	Fraction of water generated that leaves through the cathode
F	Faraday's constant, 96,487 C/mol
$\mathbf{H}$	Hessian matrix
H_i	Henry's constant for species i, $mol/(cm^3atm)$
i	Local current density, A/cm^2
i°	Exchange current density, A/cm^2
I	Total cell current density, A/cm^2
I_∞	Limiting current density, A/cm^2
k_{scx}	Setschenow salt effect parameter, cm^3/mol
L	Thickness, cm
M_i	Molecular weight of species i
n	Number of electrons transferred
N_i	Flux of species i, $mol/(cm^2\text{-}s)$
p_i	Anodic reaction order for species i
P	Power density, W/cm^2
P_i	Pressure of species i, atm
q_i	Cathodic reaction order for species i
R	Gas constant, 8.314 J/(mol-K) or 82.057 cm^3-atm/(mol-K)

R_i^e	Electrochemical reaction rate, mol/(cm^3-s)
R_i^p	Transport rate across phase boundary, mol/(cm^3-s)
s_i	Stoichiometric coefficient of species i
t	Time, s
t_i°	Transferrence number of species i relative to the solvent velocity
T	Temperature, K
U	Theoretical open-circuit potential evaluated at reference concentrations, V
U^θ	Standard electrode potential, V
U_{RE}^θ	Reference electrode potential, V
u_i	Mobility of species i, mol-cm^2/(J-s)
$\vec{v}$	Volume average velocity, cm/s
$\bar{V}_i$	Partial molar volume of species i, cm^3/mol
x_i	Liquid phase mole fraction of species i
x_i°	Liquid phase mole fraction of species i in pure water
y_i	Vapor phase mole fraction of species i
z	Spatial coordinate, cm
z_i	Charge number of species i

Greek Symbols

α_a	Anodic transfer coefficient
α_c	Cathodic transfer coefficient
δ	Diffusion layer thickness, cm
ϵ	Porosity
η	Overpotential, V
$\vec{\theta}$	Vector of parameters, θ_j
θ_j	Parameter j
Λ	Equivalent conductance, cm$^2/\Omega$
λ_i°	Limiting ionic conductivity of species i, cm$^2/\Omega$
λ_i	Ionic conductivity of species i, cm$^2/\Omega$

ν_i	Number of cations or anions produced by the dissociating electrolyte
ξ	Dimensionless spatial coordinate
ρ	Electrolyte density, g/cm^3
σ	Electrode conductivity, S/cm^2
τ	Tortuosity
ϕ	Solution phase potential, V

Superscripts and Subscripts

a	Anode
c	Cathode
D	Diffusion layer
e	Electrolyte or electrochemical rate
g	Gas phase
i	Species i
j	Species j
l	Liquid phase
r	Reference condition
R	Reaction layer
p	Production rate due to transport across a phase boundary
S	Separator layer
T	Total value
+	Cation (K^+)
—	Anion (OH^-)
o	Solvent (water)
*	Base-case value or logarithmically transformed variable

REFERENCES

1. S. Srinivasan, *J. Electrochem. Soc.*, **136**, 41C (1989).
2. K. Tomantschger, S. Srinivasan, R.D. Findlay, I. Joanes, F. McClusky, L. Oporto, A. Reid, and K. Kordesch, "Development of a 500 Watt Bipolar Alkaline Fuel Cell," 859370, 20th Intersociety Energy Conversion Engineering Conference (1985).
3. H.V. Broeck, "Fuel Cell Seminar," abstracts, p. 125, Tucsan, AZ, May 19–22 (1985).
4. J.O'M. Bockris and S. Srinivasan, "Fuel Cells: Their Electrochemistry," McGraw-Hill, New York (1969).
5. J.O'M. Bockris and A.J. Appleby, "Alkaline Fuel Cells," in *Assessment of Research Needs for Advanced Fuel Cells*, S.S. Penner, Editor, Department of Energy Contract No. 1–84ER30060 (1985).
6. E.J. Taylor and S. Srinivasan, "Alkaline Systems," in *Power Sources for Electric Vehicles*, B.D. McNicol and D.A.J. Rand, Editors, p. 839, Elsevier, New York (1984).
7. A. Winsel and G.J. Richter, "Conversion of Hydrogen in Fuel Cells," in *Electrochemical Hydrogen Technologies*, H. Wendt, Editor, p. 381, Elsevier, New York (1990).
8. K. Kinoshita, F.R. McLarnon, E.J. Cairns, "Fuel Cells: A Handbook," Department of Energy Contract No. DE-AC03–76SF00098 (1988).
9. L. Swette and J. Giner, *J. Power Sources*, **22**, 399 (1988).
10. K. Tomantschger, F. McClusky, L. Oporto, A. Reid, *J. Power Sources*, **18**, 317 (1986).
11. W.M. Vogel and K.A. Klinedinst, *Electrochim. Acta*, **22**, 1385 (1977).

12. S. Srinivasan and E. Gileadi, "Electrochemical Techniques in Fuel Cell Research," in *Handbook of Fuel Cell Technology*, C. Berger, Editor, Prentice-Hall, Inc., Englewood Cliffs, NJ (1968).

13. R. DeLevie in, "Advances in Electrochemistry and Electrochemical Engineering," Vol. 6, P. Delahay, Editor, p. 329, Interscience Publishers Inc., New York (1967).

14. Y.A. Chizmadzhev and Y.G. Chirkov in, "Comprehensive Treatise of Electrochemistry," Vol. 6, E.B. Yeager, J. O'M. Bockris, B.E. Conway, and S. Sarangapani, Editors, p. 317, Plenum Press, New York (1983).

15. B.V. Tilak, R.S. Yeo, and S. Srinivasan in, "Comprehensive Treatise of Electrochemistry," Vol. 3, J. O'M. Bockris, B.E. Conway, E.B. Yeager, and R.E. White, Editors, p. 39, Plenum Press, New York (1981).

16. K.V. Kordesch, *J. Electrochem. Soc.*, **125**, 77C (1978).

17. J. Newman and W. Tiedemann, *AIChE J.*, **21**, 25 (1975).

18. F.G. Will, *J. Electrochem. Soc.*, **110**, 145 (1963).

19. F.G. Will, *J. Electrochem. Soc.*, **110**, 152 (1963).

20. J.A. Rockett and R. Brown, *J. Electrochem. Soc.*, **113**, 207 (1966).

21. D.N. Bennion and C.W. Tobias, *J. Electrochem. Soc.*, **113**, 593 (1966).

22. I. Iliev, S. Gamburzev, A. Kaisheva, and J. Mrha, *J. Applied Electrochem.*, **5**, 291 (1975).

23. J. Giner and C. Hunter, *J. Electrochem. Soc.*, **116**, 1124 (1969).

24. H.R. Kunz, L.J. Bregoli, and S.T. Szymanski, *J. Electrochem. Soc.*, **131**, 2815 (1984).

25. H.R. Kunz and L.A. Murphy, *J. Electrochem. Soc.*, **135**, 1124 (1988).

26. M.B. Cutlip, *Electrochim. Acta*, **20**, 767 (1975).

27. R. Aris, "Elementary Chemical Reactor Analysis," (1969).

28. R.P. Iczkowski and M.B. Cutlip, *J. Electrochem. Soc.*, **127**, 1433 (1980).

29. Pehr Bjornbom, *Electrochim. Acta*, **32**, 115 (1987).

30. J.S. Newman and C.W. Tobias, *J. Electrochem. Soc.*, **109**, 1183 (1962).

31. R. Darby, *Adv. Energy Convers.*, **5**, 43 (1965).

32. R.E. White, M.A. Nicholson, L.G. Kleine, J. Van Zee, and R. Darby, *J. Electrochem. Soc.*, **131**, 268 (1984).

33. S. Motoo, M. Watanabe, and N. Furuya, *J. Electroanal. Chem.*, **160**, 351 (1984).

34. M. Watanabe, M. Tomikawa, and S. Motoo, *J. Electroanal. Chem.*, **182**, 193 (1985).

35. M. Watanabe, M. Tozawa, and S. Motoo, *J. Electroanal. Chem.*, **183**, 391 (1985).

36. M. Watanabe, M. Tomikawa, and S. Motoo, *J. Electroanal. Chem.*, **195**, 81 (1985).

37. M. Watanabe, K. Makita, H. Usami, and S. Motoo, *J. Electroanal. Chem.*, **197**, 195 (1986).

38. K.V. Ramesh, and P.R. Sarode, S. Vasudevan, and A.K. Shukla, *J. Electroanal. Chem.*, **223**, 91 (1987).

39. T. Kenjo and K. Kawatsu, *Electrochim. Acta*, **30**, 229 (1985).

40. L. Müller and L.N. Nekrasov, *Electrochim. Acta*, **9**, 1015 (1964).

41. L. Müller and L.N. Nekrasov, *J. Electroanal. Chem.*, **9**, 282 (1965).

42. A. Damjanovic, M.A. Genshaw, and J. O'M. Bockris, *J. Phys. Chem.*, **70**, 3761 (1966).

43. A. Damjanovic, M.A. Genshaw, and J. O'M. Bockris, *J. Electrochem. Soc.*, **114**, 1107 (1967).

44. A. Kozawa, *J. Electroanal. Chem.*, **8**, 20 (1964).

45. R.J. Bowen and H.B. Urbach, *J. Chem. Phys.*, **49**, 1206 (1968).

46. E. Yeager, *Electrochim. Acta*, **29**, 1527 (1984).

47. K. Mund, G. Richter, and F. von Sturm, "Proceedings of the Workshop on the Electrocatalysis of Fuel Cell Reactions," The Electrochemical Society Inc., Pennington, NJ, p. 47 (1978).

48. W. Vielstich, "Proceedings of the Workshop on the Electrocatalysis of Fuel Cell Reactions," The Electrochemical Society Inc., Pennington, NJ, p. 67 (1978).

49. J. Appleby and R.K. Sen, "Proceedings of the Workshop on the Electrocatalysis of Fuel Cell Reactions," The Electrochemical Society Inc., Pennington, NJ, p. 84 (1978).

50. D.B. Sepa, M.V. Vojnovic, and A. Damjanovic, *Electrochim. Acta*, **25**, 1491 (1980).

51. A.J. Appleby and J. Marie, *Electrochim. Acta*, **24**, 195 (1979).

52. R.B. Bird, W.E. Stewart, E.N. Lightfoot, "Transport Phenomena," John Wiley & Sons, New York, NY (1960).

53. J.S. Newman, "Electrochemical Systems," Prentice-Hall, Inc., Englewood Cliffs, NJ (1973).

54. D.M. Bernardi, *J. Electrochem. Soc.*, **137**, 3344 (1990).

55. R.E. White, S.E. Lorimer, and R. Darby, *J. Electrochem. Soc.*, **130**, 1123 (1983).

56. S. G. Bratsch, *J. Phys. Chem. Ref. Data*, **18** (1989).

57. J. Newman and T.W. Chapman, *AIChE J.*, **19**, 343 (1973).

58. L.G. Austin, "The Electrochemical Theory of Fuel Cells," in *Handbook of Fuel Cell Technology*, C. Berger, Editor, Prentice-Hall, Inc., Englewood Cliffs, NJ (1968).

59. W.L. Fielder and J. Singer, Paper 66 presented at the Electrochemical Society Meeting, Seattle, WA, October 14–19 (1990).

60. G. Akerlof and P. Bender, *J. Amer. Chem. Soc.*, **63**, 1085 (1941).

61. B.A. Finlayson, "Nonlinear Analysis in Chemical Engineering," McGraw-Hill, New York (1980).

62. W.J. Minkowycz, E.M. Sparrow, G.E. Schneider, and R.H. Pletcher, "Handbook of Numerical Heat Transfer," John Wiley & Sons, New York (1988).

63. R.E. Martin and M.A. Manzo, "Alkaline Fuel Cell Performance Investigation," 889498, 23rd Intersociety Energy Conversion Engineering Conference (1988).

64. S.C. Yang, M.B. Cutlip, and P. Stonehart, *Electrochim. Acta*, **35**, 869 (1990).

65. T.I. Evans and R.E. White, *J. Electrochem. Soc.*, **136**, 2798 (1989).

66. J. Newman, *Electrochim. Acta*, **24**, 223 (1979).

67. IMSL Library Ver. 1.0, "Problem-Solving Software System for Mathematical and Statistical FORTRAN Programming," IMSL, Inc., Houston, Texas (1987).

68. K. V. Kordesch, "Low Temperature–Low Pressure Fuel Cell with Carbon Electrodes," in *Handbook of Fuel Cell Technology*, C. Berger, Editor, Prentice-Hall, Inc., Englewood Cliffs, NJ (1968).

69. M.K. Tham, R.D. Walker, and K.E. Gubbins, *J. Phys. Chem.*, **74**, 1747 (1970).

70. D. Dobos, "Electrochemical Data," Elsevier, Amsterdam, The Netherlands (1975).

71. L.S. Darken and H.F. Meier, *J. Amer. Chem. Soc.*, **64**, 621 (1942).

72. M.B. Knaster and L.A. Apel'baum, *Russ. J. Phys. Chem.*, **38**, 120 (1964).

73. K.E. Gubbins and R.D. Walker, *J. Electrochem. Soc.*, **112**, 469 (1965).

74. P. Ruetschi and R.F. Amlie, *J. Phys. Chem.*, **70**, 718 (1966).

75. R.E. Davis, G.L. Horvath, and C.W. Tobias, *Electrochimica Acta.*, **12**, 287 (1967).

76. S.K. Shoor, R.D. Walker, and K.E. Gubbins, *J. Phys. Chem.*, **73**, 312 (1969).

77. C.L. Young, "IUPAC Solubility Data Series," Vol. **5/6**, Pergamon Press, New York (1981).

78. B.B. Bensen, D. Krause, and M.A. Peterson, *J. Soln. Chem.*, **8**, 655 (1979).

79. R. Battino and E. Wilhelm, "IUPAC Solubility Data Series," Vol. **5/6**, Pergamon Press, New York (1981).

APPENDIX A

CORRELATIONS FOR DIFFUSIVITY AND SOLUBILITY PARAMETERS

In order to obtain a realistic simulation of the alkaline fuel cell, the various transport and thermodynamic properties should be dependent on the temperature and concentration since the concentration of all species readily changes during the simulation. Correlations were developed to predict the values of these transport and thermodynamic parameters as a function of concentration (or pressure) and the system temperature.

Correlation of the Water Vapor Pressure to the Electrolyte Concentration

Since it is assumed that equilibrium is established at the gas-liquid interfaces in the active regions of the fuel cell, the water vapor pressure above the KOH electrolyte can be correlated with the KOH concentration. Experimental measurements of this water vapor pressure above KOH have been measured from 20 °C to 80 °C for KOH concentrations ranging from 0% to 50% KOH (by weight) (76). Fitting this data to a linear function ($R^2 \approx .99$) allows the following correlation to be defined:

$$P_{H_2O} = a_{H_2O} + b_{H_2O}\, C_e \qquad [159]$$

where C_e is in mol/cm^3 and the vapor pressure of water is in atm. The regression coefficients are shown in Table XVII. Note that for temperatures higher than 80 °C the water vapor pressure was extrapolated from the lower temperature correlations. Extrapolating the data in this manner can introduce some uncertainty in the water vapor pressure and, thus, in the model predictions. Hence, caution should be used for temperatures higher than 80 °C.

Table XVII. Regression coefficients for the correlation of the water vapor pressure to the electrolyte concentration.

Temperature (K)	a_{H_2O}	b_{H_2O}
333	0.19503	-11.222
343	0.30777	-18.468
353	0.46858	-28.095

Correlations for Diffusivities

The gas phase diffusivities for oxygen in water and hydrogen in water, at low pressures, can be given by corresponding states principles (52) where

$$\frac{PD_{ij}}{(P_{c_i}P_{c_j})^{1/3}(T_{c_i}T_{c_j})^{5/12}\sqrt{\frac{1}{MW_i}+\frac{1}{MW_j}}} = 3.640\times10^{-4}\left(\frac{T}{\sqrt{T_{c_i}T_{c_j}}}\right)^{2.334} \qquad [160]$$

Equation [160] simplifies to

$$D^g_{O_2} = \frac{4.2076\times10^{-7}\,T^{2.334}}{P}\ \text{cm}^2/\text{s} \qquad [161]$$

for oxygen in water and

$$D^g_{H_2} = \frac{2.1410\times10^{-6}\,T^{2.334}}{P}\ \text{cm}^2/\text{s} \qquad [162]$$

for hydrogen in water where T is in °K, and P in atm.

The diffusivity for dissolved oxygen in KOH and for dissolved hydrogen in KOH was obtained from the experimental measurements of Tham *et al.* (77) where they measured the diffusivities from 25 °C to 100 °C for 0 to 50% KOH solutions. These diffusivities were correlated as a function of KOH concentration by fitting their data to cubic polynomials. For temperatures higher than 80 °C, the data were extrapolated from the lower temperatures.

The diffusivity of the electrolyte species were determined by scaling the equivalent conductances of the KOH electrolyte at 25 °C to the temperature of interest by using the ratio of the limiting equivalent ionic conductivities. That is, the limiting ionic conductivities given by (78) for 25 °C and 100 °C, shown in Table XVIII, were interpolated to the temperature of interest as shown in Table XVIII, for example, at 80 °C. The ratio of the limiting ionic equivalent conductivity for species i, λ_i°, to the limiting equivalent conductivity, Λ° $(= \lambda_-^\circ + \lambda_+^\circ)$, at the temperature of interest was

then multiplied by the equivalent conductivity, Λ, of the KOH electrolyte (at 25 °C) as given by (79) to get the ionic equivalent conductivity, λ_i, for species i.

$$\Lambda = 272.0 - 3846.59\, C_e^{0.5} + 1.41 \times 10^5\, C_e\left(1.0 - 7.191\, C_e^{0.5}\right) \quad (\mathrm{cm}^2/\Omega) \qquad [163]$$

where the electrolyte concentration is in mol/cm^3. For example, at 80 °C and for a 7M KOH electrolyte, the ionic equivalent conductivity for K^+ would be:

$$\lambda_+ = \left[272. - 3846.59\sqrt{7\times10^{-3}} + 1.41\times10^5\cdot 7\times10^{-3}\left(1.0 - 7.191\sqrt{7\times10^{-3}}\right)\right] \times \frac{166.}{166. + 380.} \quad (\mathrm{cm}^2/\Omega) \qquad [164]$$

and similarly for the OH^- ion.

Once the ionic equivalent conductivities have been determined as a function of the KOH concentration and temperature, the ionic diffusivities can be determined by (53):

$$D_i = \frac{RT\lambda_i}{F^2} \qquad [165]$$

and assuming that the Nernst-Einstein condition applies the mobilities of the ionic species are readily calculated from the ionic diffusivities:

$$u_i = \frac{D_i}{RT} \qquad [166]$$

Correlations for the Solubility of Oxygen and Hydrogen Gas in KOH Solutions

The solubilities of hydrogen and oxygen gas in KOH have been investigated by many investigators (80–85) where the solubility data is usually reported in the form of a Setschenow salt effect parameter. This salt effect parameter, k_{scx}, can be written in the form

$$k_{scx} = \frac{1}{C_e}\log\left(\frac{x_i^\circ}{x_i}\right) \quad (\mathrm{cm}^3/\mathrm{mol}) \qquad [167]$$

Table XVIII. Limiting equivalent ionic conductivities for different temperatures.

Species	λ_i° (cm^2/eq.-Ω)		
	25 °C	100 °C	80 °C [a]
OH^-	197.6	446.	380.
K^+	73.5	200.	166.
Λ°	271.1	646.	546.

[a] interpolated

where x_i is the mole fraction of gas in the electrolyte solution and x_i° is the mole fraction of the gas in pure water. For hydrogen, k_{scx} is fairly constant at 0.129 over the temperature range of 25 to 100 °C . For oxygen, the salt effect parameter varies almost linearly over the temperature range of 60 to 100 °C such that

$$k_{scx,O_2} = 0.1923 - 0.10 \times 10^{-3} T \ \ (\mathrm{cm^3/mol}) \qquad [168]$$

where T is given in K. Bensen *et al.* (86) derived the following equation for the solubility of oxygen in water over the temperature range of 373 to 563 K:

$$\ln \frac{1}{x^\circ_{O_2}} = -4.1741 + \frac{1.3104 \times 10^4}{T} - \frac{3.4170 \times 10^6}{T^2} + \frac{2.4749 \times 10^8}{T^3} \qquad [169]$$

The mole fraction of hydrogen gas in pure water was similarly fitted to experimental data by Battino and Wilhelm (87) over the temperature range of 273 to 353 K giving:

$$\ln x^\circ_{H_2} = -48.1611 + \frac{5528.45}{T} + \frac{16.8893}{\ln \frac{T}{100.0}} \qquad [170]$$

Henry's law constants were formulated as a function of temperature and concentration by rearranging Eq. [167] to give:

$$H_i = \frac{(2C_e + C_o)}{1 - x_i} x_i \quad (i = O_2, H_2) \qquad [171]$$

where the mole fraction for species i is given by Eqs. [167] and [169] for oxygen

$$x_{O_2} = \frac{1}{\exp\left[-4.1741 + \frac{1.3104\times10^4}{T} - \frac{3.4170\times10^6}{T^2} + \frac{2.4749\times10^8}{T^3}\right]} \times \frac{1}{10^{(0.1923-0.10\times10^{-3}T)1000C_e}} \qquad [172]$$

and by Eqs. [167] and [170] for hydrogen:

$$x_{H_2} = \frac{\exp\left[-48.1611 + \frac{5528.45}{T} + 16.8893 \ln \frac{T}{100}\right]}{10^{129.0C_e}} \qquad [173]$$